Winter 2018

Visible-to-Near-Infrared Spectral Variability of Hydrated Sulfates and Candidate Mars Landing Sites: Implications for the Mastcam-Z Investigation on NASA's Mars-2020 Rover Mission

Darian Dixon
Western Washington University, dixond4@wwu.edu

Visible-to-Near-Infrared Spectral Variability of Hydrated Sulfates and Candidate Mars Landing Sites: Implications for the Mastcam-Z Investigation on NASA's Mars-2020 Rover Mission

By Darian Dixon

Accepted in Partial Completion of

the Requirements for the Degree

Master of Science

Kathleen L. Kitto, Dean of the Graduate School

ADVISORY COMMITTEE

Chair, Dr. Melissa Rice

Dr. Pete Stelling

Dr. Michael Kraft

MASTER'S THESIS

In presenting this thesis in partial fulfillment of the requirements for a master's degree at Western Washington University, I grant to Western Washington University the non-exclusive royalty-free right to archive, reproduce, distribute, and display the thesis in any and all forms, including electronic format, via any digital library mechanisms maintained by WWU.

I represent and warrant this is my original work, and does not infringe or violate any rights of others. I warrant that I have obtained written permissions from the owner of any third party copyrighted material included in these files.

I acknowledge that I retain ownership rights to the copyright of this work, including but not limited to the right to use all or part of this work in future works, such as articles or books.

Library users are granted permission for individual, research and non-commercial reproduction of this work for educational purposes only. Any further digital posting of this document requires specific permission from the author.

Any copying or publication of this thesis for commercial purposes, or for financial gain, is not allowed without my written permission.

Signature: Darian Dixon

Date: 2/23/2018

Visible-to-Near-Infrared Spectral Variability of Hydrated Sulfates and Candidate Mars Landing Sites: Implications for the Mastcam-Z Investigation on NASA's Mars-2020 Rover Mission

By Darian Dixon

A Thesis

Presented to

The faculty of

Western Washington University

In Partial Completion of

the Requirements for the Degree

Master of Science

By Darian T. Dixon

February 2018

ABSTRACT

The Mars-2020 rover mission will explore an astrobiologically relevant ancient environment on Mars, establish geologic context of the region, assess past habitability, and cache rocks for a future sample return. The Mastcam-Z instrument is a stereoscopic, zoom-enabled multispectral imager that will be critical to these objectives. As one of the mission's primary reconnaissance tools, Mastcam-Z's two cameras will acquire red-green-blue (RGB) true-color images and visible-to-near-infrared (VNIR) images with 11 narrowband filters from ~400-1100 nm. Mastcam-Z's new ~975 nm spectral filter will help characterize the ~950-1000 nm absorption band in hydrated minerals, which has not been resolvable by previous rover multispectral imagers. We hypothesize that this filter will allow Mastcam-Z to better characterize VNIR hydration bands in hydrated sulfates, although mineral mixtures, iron-oxide dust contamination, and varying grain size will affect band depths. At the time of this writing, three candidate landing sites are being considered for the Mars-2020 mission, each bearing mineralogical units extensively investigated by high-resolution orbital SWIR (short-wave-infrared) imagery. We also hypothesize that Mastcam-Z VNIR spectral parameters can distinguish the prominent geologic units characterized by orbital SWIR at each landing site, although iron-oxide dust distribution is the suspected primary control on VNIR spectral variability on Mars. Synthetic magnesium and calcium sulfate samples were measured with a laboratory spectrometer and acquired spectra were convolved to expected Mastcam-Z resolution to identify the spectral filter combinations most sensitive to signatures of hydration. Sulfate samples were subject to bimodal mineral mixing, grain size separation, and contamination with a martian dust simulant to quantify the spectral effects these properties have on the ~950-1000 nm hydration band. SWIR imagery from the Mars 2020 candidate landing sites were also convolved to expected Mastcam-Z resolution. Spectral parameters were then developed at expected Mastcam-Z resolution that would corroborate mineral detections made by extensively-tested SWIR spectral parameters and SWIR spectra of prominent units. Mastcam-Z-simulated hydrated sulfate

spectra reveal that Mastcam-Z can detect hydration in bimodal mixtures of hydrated Mg-sulfates but bimodal mixtures Ca-sulfates may present challenge unless significantly gypsum-rich. Iron-oxide dust contamination significantly shallows the ~950-1000 nm hydration band in hydrated sulfates, whereas band depth generally increases with increasing grain size. Mastcam-Z-simulated orbital imagery reveals distinct Mastcam-Z VNIR spectral parameters distinguishing prominent geologic units for each landing site, although modified versions of Pancam parameters are recommended for the Columbia Hills. Seasonal changes in spectral variability at the Columbia Hills and regional variation in spectral parameter effectiveness at NE Syrtis indicate VNIR spectral properties on Mars are likely controlled by surface dust distribution. These results provide specific operational recommendations for Mastcam-Z and insights into the nature of VNIR spectra on Mars.

ACKNOWLEDGEMENTS

To Dr. Briony Horgan, Dr. Jeffrey Johnson, Jennifer Buz, and several others at NASA JPL, Caltech, and Arizona State University, thank you for your frequent support and input – this thesis wouldn't have been possible without you. To my mentor, Dr. Margaret Fraiser, thank you for giving an ear to any and all emotional breakdowns even while living 2000 miles away. To my loving parents that moved to Washington to be closer to me, thank you for being a daily source of encouragement and my rock throughout my entire life. To Luan Heywood, thank you for being one of the greatest friends I've made since my move to Washington and for being someone I could always confide in throughout this journey. To my advisor Dr. Melissa Rice, thank you for believing in me even when I didn't believe in myself. Your guidance made all this possible. To my thesis committee, thank you for your support and advice throughout the entire process. To the faculty and students in the geology department, thank you for the community you've provided and for making my time at WWU truly unforgettable. And to my beautiful fiancé that walked with me every step of the way, thank you for absolutely everything. You are my Sun, my moon, and all my stars and there's no way any of this would have been possible without you.

TABLE OF CONTENTS

ABSTRACT iv

ACKNOWLEDGEMENTS vi

LIST OF FIGURES AND TABLES viii

Chapter 1

INTRODUCTION TO THESIS 1

Chapter 2

INTRODUCTION TO SULFATES INVESTIGATION 13

METHODS FOR SULFATES INVESTIGATION 17

RESULTS FOR SULFATES INVESTIGATION 22

DISCUSSION FOR SULFATES INVESTIGATION 27

CONCLUSIONS FOR SULFATES INVESTIGATION 36

FUTURE WORK FOR SULFATES INVESTIGATION 37

Chapter 3

INTRODUCTION TO CRISM INVESTIGATION 38

METHODS FOR CRISM INVESTIGATION 45

JEZERO RESULTS 50

JEZERO DISCUSSION 52

NE SYRTIS RESULTS 55

NE SYRTIS DISCUSSION 57

COLUMBIA HILLS RESULTS 60

COLUMBIA HILLS DISCUSSION 63

DISCUSSION FOR CRISM INVESTIGATION 65

CONCLUSIOSN FOR CRISM INVESTIGATION 67

FUTURE WORK FOR CRISM INVESTIGATION 68

REFERENCES CITED 71

FIGURES 90

TABLES 137

LIST OF FIGURES AND TABLES

Figure 1. Example calcite spectrum showing appearance of absorption bands

Figure 2. Orbital spectral data from Jezero Crater showing how CRISM data is used

Figure 3. Pancam, Mastcam, and Mastcam-Z simulated spectra of gypsum

Figure 4. High-definition illustration of the Mars-2020 rover

Figure 5. Depiction of experimental setup for spectral analysis of sulfate samples

Figure 6. Illustration showing the process for calculating band depth

Figure 7. Hypothetical transmission profiles for Mastcam-Z

Figure 8. Overview of spectral features to be calculated for all Mg- and Ca-sulfate spectra

Figure 9. Hypothetical transmission profile of Mastcam-Z 445 nm filter

Figure 10. Example of 445 nm band error correction

Figure 11. Dust-free gypsum and epsomite grain size series spectra

Figure 12. Dust-free Ca-sulfate bimodal mixture spectra

Figure 13. Dust-free Mg-sulfate bimodal mixture spectra

Figure 14. Dust-contaminated Mg- and Ca-sulfate bimodal mixture spectra

Figure 15. Detection thresholds for dust-free gypsum and epsomite grain size series

Figure 16. Detection thresholds for all bimodal Mg- and Ca-sulfate mixture sets

Figure 17. Hydration band depth with respect to H_2O/SO_4 ratio in hydrated sulfates

Figure 18. Hydration band position with respect to H_2O/SO_4 ratio in hydrated sulfates

Figure 19. Simulated epsomite-kieserite mixture spectra compared to laboratory mixture spectra

Figure 20. Overview of key compositional spectral absorption bands

Figure 21. Locations of Mars-2020 landing sites

Figure 22. Orbital imagery of Jezero Crater

Figure 23. Orbital imagery of NE syrtis

Figure 24. Orbital imagery of Gusev Crater

Figure 25. Overview of CRISM observations acquired at each Mars-2020 landing site

Figure 26. Overview of spectral ratio process in CRISM analysis

Figure 27. Geologic units of interest at Jezero Crater

Figure 28. Mastcam-Z and CRISM SWIR parameter composites for Jezero Crater regions of interest

Figure 29. Mastcam-Z simulated composites and CRISM SWIR parameter composites for Jezero Crater

Figure 30. SWIR reflectance spectra from Jezero Crater

Figure 31. VNIR reflectance spectra from Jezero Crater

Figure 32. Simulated 3D perspectives of Jezero Crater using Mastcam-Z parameters

Figure 33. Geologic units of interest at south NE Syrtis

Figure 34. Mastcam-Z and CRISM SWIR parameter composites for south NE Syrtis regions of interest

Figure 35. Mastcam-Z simulated composites and CRISM SWIR parameter composites for south NE Syrtis

Figure 36. SWIR reflectance spectra from south NE Syrtis

Figure 37. VNIR reflectance spectra from south NE Syrtis

Figure 38. Mastcam-Z simulated composites and CRISM SWIR parameter composites for NE Syrtis ellipse

Figure 39. CRISM SWIR parameter map, VNIR and SWIR reflectance spectra at NE Syrtis ellipse

Figure 40. Geologic units of interest at the Columbia Hills

Figure 41. Mastcam-Z and CRISM SWIR parameter composites for Columbia Hills

Figure 42. Mastcam-Z and CRISM SWIR parameter composites for Columbia Hills regions of interest

Figure 43. Mastcam-Z simulated RGB and deccorelation stretches for Columbia Hills

Figure 44. VNIR and SWIR reflectance spectra from Columbia Hills

Figure 45. Simulated 3D perspectives of Columbia Hills using Mastcam-Z parameters

Table 1. Summary of Mg- and Ca-sulfates used in this work

Table 2. Data from dust-free epsomite and gypsum grain size series

Table 3. Data from dust-free bimodal Ca-sulfate mixtures

Table 2. Data from dust-free bimodal Mg-sulfate mixtures

Table 3. Data from dust-contaminated bimodal Mg- and Ca-sulfate mixtures

Table 4. Simulated epsomite-kieserite mixtures compared to laboratory mixtures

Table 5. Summary of CRISM observations used in this work

Table 8. Summary CRISM spectral parameters used in this work

Table 9. Summary of Suggested Mastcam-Z spectral parameters

Table 10. Summary of Pancam parameters and modified Mastcam-Z versions

1.0 INTRODUCTION

1.1.1 Introduction to Thesis and Study Motivation

Introduction to Thesis

Over the course of decades, NASA missions have explored the surface of Mars from orbit and on the ground, uncovering a planetary history brimming with the potential for habitable environments in the distant past. Fueling the search for ancient habitable environments, intriguing hydrated mineral deposits have been discovered using spectral imagery. Unraveling Mars history will rest on our understanding of these deposits. Going forward, linking orbital mineral mapping with ground-based observations from rovers will help characterize the ancient martian environment, providing more complete models of Mars' planetary evolution and pinpointing regions most likely to have been hospitable. The next chapter of this longstanding exploration effort, NASA's Mars-2020 rover, will characterize the surface geology and assess the astrobiological potential of a compelling region of Mars. Mastcam-Z, a stereoscopic, zoom-enabled multispectral imager will help guide the Mars-2020 rover. The dual-camera instrument will provide red-green-blue (RGB) true-color imagery and visible-to-near-infrared (VNIR) multispectral imagery vital to dictating the rover's navigation and science investigations. 11 VNIR spectral filters covering ~400-1100 nm will allow Mastcam-Z to be sensitive to subtle differences in color inherent to mineralogy and chemical composition. This multispectral imagery, coupled with true-color observations, will identify broad compositional and morphological differences in rocks to help guide *in situ* scientific analyses. Herein, I describe my efforts to support the Mars-2020 mission: investigating the capabilities of the Mastcam-Z multispectral imaging system and the reflectance spectroscopic properties of minerals on Mars.

Two separate studies comprise this work: (1) a laboratory investigation of the visible-to-near-infrared reflectance spectra of Mars-relevant hydrated Mg- and Ca-sulfate minerals, with a focus on the

morphology of a spectral signature near ~950-1000 nm that is indicative of hydration, and (2) an investigation of orbital spectral imagery taken of the three Mars-2020 candidate landing sites. Laboratory spectra and orbital spectral imagery are convolved to the estimated spectral resolution of Mastcam-Z. These data are analyzed to determine what grain size, mineral mixing, and dust contamination conditions allow for hydration in Mg/Ca-sulfates to be detected by Mastcam-Z, Mastcam-Z's ability to constrain the prominent geologic units at each landing site, and what phenomena influence VNIR spectral variability on Mars. Recommendations are made as to what combinations of Mastcam-Z imaging filters should be used to scan for hydration in sulfate units and what parameters allow Mastcam-Z multispectral imagery to distinguish prominent geologic units at the three proposed landing sites. The following three chapters describe this work. Chapter 1 is a broad introduction presenting the motivation for these investigations and necessary background information. Chapter 2 fully details the laboratory investigation of hydrated sulfates and Chapter 3 fully details the orbital investigation of Mars-2020 landing sites.

Reflectance spectra can be used to assess the mineralogy of a surface (see section 1.2). Mastcam-Z will be one of the primary reconnaissance instruments on the Mars-2020 rover. Visible approximate-true-color (ATC) and VNIR multispectral images acquired by Mastcam-Z will help inform the rover's navigation and target selection for in-situ analyses and sample caching. A variety of hydrated/hydroxylated minerals exhibit an absorption feature centered at ~950-1000 nm (Hunt, 1977), including hydrated sulfates. However, most laboratory work characterizing Mars-relevant mineral spectra has concentrated on short-wave-infrared (~900-2500 nm; SWIR) features to support the CRISM (Compact Reconnaissance Imaging Spectrometer for Mars; Murchie et al., 2007); and OMEGA (Observatoire pour la Mineralogie, l'Eau, les Glaces et l'Activitie; Bibring et al., 2004) missions that are capable of imaging at longer wavelengths. As such, this VNIR spectral signature remains to be investigated in depth and is important for identifying hydrated minerals when longer-wavelength data

are unavailable. Hydrated sulfates on Mars present a variety of potential formation mechanisms including evaporitic deposition, similar to playa lake environments (Warren, 1999; Tosca and McLennan, 2006), and acidic, sulfurous hydrothermal environments (e.g. Golden et al., 2005; Klingelhöfer et al., 2004; Squyres et al., 2004; Wang et al., 2006b). To yield a firmer understanding of these environments in a martian context, it is crucial we understand how Mastcam-Z will view these minerals by investigating the morphology of the ~950-1000 nm spectral feature.

Additionally, it is important to understand how spectral signals observed from orbit correlate with what can be observed on the ground by Mastcam-Z. Orbital spectrometers like CRISM operate at higher spectral resolution and over a wider effective wavelength range than ground-based imaging spectrometers. Beyond sulfates, a variety of other key materials are present at the Mars-2020 candidate landing sites, including phyllosilicates, carbonates, and mafic minerals. These mineral deposits have been well characterized in SWIR using the CRISM instrument (e.g. Carter and Poulet, 2012; Ehlmann and Mustard, 2012; Goudge et al., 2015), but it is not known how they will appear to Mastcam-Z VNIR. Mastcam-Z will detect compositional differences on the surface both for long-distance reconnaissance and for mapping of smaller-scale mineral distributions to guide traverse planning and sample caching. To support future Mastcam-Z operation, this work links orbital SWIR spectroscopy to simulated Mastcam-Z VNIR spectroscopy and identifies parameters allowing Mastcam-Z to reproduce some spectral reconnaissance achieved from orbit. However, Mastcam-Z is not the only instrument that may benefit from this work. Future rovers/landers may be developed with evolved multispectral imagining instruments. No past research has convolved orbital hyperspectral images to the simulated resolution of ground-based multispectral instruments and this work serves to demonstrate that orbital SWIR imagery can be used to develop VNIR parameters for multispectral imagers.

1.2 Reflectance Spectroscopy on Mars

The Mastcam-Z instrument will utilize reflectance spectroscopy (e.g. Hunt, 1977; Clark and Roush, 1984a), the imaged interactions between incident sunlight and surface material, to interpret surface mineral composition. Reflectance spectra on Mars are typically acquired in the VNIR (~400-1100 nm) and SWIR (~900-2500 nm). Mineral grains reflect or absorb light at different wavelengths. Chemical composition, molecular geometry, grain size, and the number of distinct phases present control the resulting reflectance spectrum. Absorption features (Figure 1), defined as the observed decrease in reflected light at specific wavelengths (also known as absorption bands), can be distinct to specific minerals (e.g. Hunt, 1977; Clark et al., 1999). Absorption bands result from electronic processes and vibrational processes (e.g., Hunt, 1977; Burns, 1993; Clark et al., 1999).

In electronic processes, photons exert various effects on mineral electrons and cause electronic absorptions. The prominent electronic processes, crystal field effects and charge transfer processes, occur in transition elements. Crystal field effects result when energy levels in d-orbitals are split between neighboring atoms in a crystal lattice, allowing electrons to more easily move into higher energy states after photon absorption (e.g., Burns, 1993) and charge transfer processes involve movement of an electron between ions/ligands (e.g., Morris et al., 1985; Clark et al., 1999).

Vibrating bonds in dipolar molecules give rise to vibrational absorptions. Due to bending and stretching in molecular morphology, bonded atoms continuously tug at one another, producing nanoscale vibrations governed by bond strength and atomic mass (e.g., Wilson et al., 2012; Herzberg, 2013). A dipolar molecule can experience 3N-6 fundamental vibration frequencies (each producing an absorption band), where N is the number of atoms in the molecule (e.g., Clark et al., 1999). Additional vibration frequencies (and corresponding absorption bands) can occur: overtones, the sum of multiple instances of a single fundamental frequency, and combinations, the sum of multiple different

fundamental frequencies (e.g., Clark et al., 1999; Wilson et al., 2012; Herzberg, 2013). Combination and overtone bands are weaker and occur at shorter wavelengths than fundamentals. H_2O, OH, metal-OH, and CO_3 bearing minerals experience multiple fundamental vibrations, each with various combinations and overtones (e.g., Hunt, 1977; Clark et al., 1990; Clark et al., 1999). For example, carbonates often show diagnostic absorptions near 2300 nm and 2500 nm (Figure 1). H_2O and OH experience overtone and combination bands near ~950-1000 nm, ~1400 nm, and ~1900 nm (e.g., Hunt, 1977) that are important for detecting hydrated minerals, such as hydrated sulfates. The precise position and shape of absorption bands are dictated by a mineral's specific crystal chemistry and molecular morphology. We can, therefore, use absorption bands to infer the presence of specific minerals.

Orbital and ground-based spectrometers scour Mars' preserved ancient environments for invaluable mineralogical data. The OMEGA (Bibring et al., 2004) and CRISM (Murchie et al., 2007) instruments aboard the Mars Express (Chicarro et al., 2004) and Mars Reconnaissance Orbiter (MRO; Graf et al., 2005; Zurek and Smrekar, 2007) missions, respectively, allow high-resolution mapping of mineral deposits from orbit (Figure 2).

1.3 Martian Surface Mineralogy and Brief History

The exploration of Mars has revealed a planetary history with distinct stages of widespread geologic activity, active aqueous processes, and a paleoclimate potentially suitable for habitable surface environments (e.g. Carr and Head III, 2010a; Fassett and Head, 2011; Ehlmann et al., 2016). Much of what we know about ancient Mars has been inferred through mineralogical discoveries in terrains from three distinct martian periods: the Noachian, Hesperian, and Amazonian.

Little is known about the properties of pre-Noachian Mars (4.5 – 4.1 Ga); it is assumed that most rock from this time has been buried by younger material, reworked by impact events, and extensively eroded by aqueous/aoelian processes. Mars' dichotomy boundary – the stark geographic transition

dividing the smooth northern lowlands and rugged southern highlands – may have formed from enormous impact events during this time (e.g. Frey, 2006). Pyroxenes and olivines dominate the mineralogy of ancient basaltic-to-andesitic crust extracted from the mantle ~4.5 Ga (e.g. Halliday et al., 2001; Nimmo and Tanaka, 2005). In some regions, these units experienced subsequent weathering and alteration, forming various alteration minerals (e.g. Bibring et al., 2006).

Beginning around 4.1 Ga at the start of the Noachian (4.1 – 3.7 Ga), fluvial activity carved extensive valley networks, resulting in widespread lacustrine deposition in closed basins. (e.g. Carr and Head III, 2010; Fassett and Head, 2011; Ehlmann et al., 2016). Massive sedimentary sequences indicate a long period of fluvial activity, suggesting the atmosphere was thicker than at present. (e.g. Owen, 1992; Jakosky and Phillips, 2001). Noachian-aged sedimentary deposits contain significant amounts of phyllosilicate minerals (primarily smectites), which are also widespread throughout much of Mars' non-layered crust (e.g. Mustard et al., 2008; Ehlmann et al., 2009).

The Hesperian (3.7 – 3.0 Ga) is characterized by the loss of the bulk of the martian atmosphere, a shift from near-neutral pH to acid-sulfate aqueous chemistry, the eventual depletion surface water volume, and the conclusion of valley network formation (e.g. Bibring et al., 2006; Bouley et al., 2009; Hoke and Hynek, 2009; Carr and Head III, 2010a; Fassett and Head, 2011). Impact-induced hydrothermal systems sustained some limited phyllosilicate formation (e.g. Marzo et al., 2010; Mangold et al., 2012), but Hesperian-aged deposits often contain Mg/Ca-carbonates, Mg/Ca/Fe-sulfates, opaline silicas, iron oxides, and pristine to partially-altered mafic volcanics (e.g. Bibring et al., 2006; Fassett and Head, 2011; Ehlmann and Edwards, 2014). Hydrated sulfates primarily occur in Hesperian-aged deposits and understanding how these minerals spectrally appear to Mastcam-Z will enable better characterization of ancient Hesperian environments.

In the frigid and hyper-arid Amazonian period (3.0 Ga – Present), aeolian activity is the primary control on landscape modification (e.g. Hartmann et al., 2005; Carr and Head III, 2010; Fassett and Head, 2011). With minimal ongoing geologic activity, erosion rates are several orders of magnitude lower than previous periods (e.g. Golombek and Bridges, 2000) and new aqueous alteration processes at the surface have likely ceased.

These alteration minerals provide valuable clues to the nature of ancient depositional environments on Mars. Smectites often form in aqueous environments with circum-neutral to alkaline pH, and are often deposited in marine and lacustrine environments (Velde, 2013). Some crustal phyllosilicate units on Mars may have formed via groundwater-crust interactions and impact-induced hydrothermal systems (e.g. Ehlmann et al., 2011). Mars' phyllosilicate-rich Noachian mineralogy indicates near-neutral pH aqueous alteration occurred over large areas on the surface and in groundwater reservoirs during this time. Hesperian sulfates indicate substantial sulfur supply, likely due to lava outgassing during volcanic events (e.g. Bibring et al., 2006) creating the Tharsis Rise – the largest volcanic complex on Mars (e.g., Nimmo and Tanaka, 2005; Carr and Head III, 2010). Extensive sulfur outgassing, coupled with volcanically-induced release of other volatiles, may have resulted in sulfur oxidation in the martian atmosphere, precipitating H_2SO_4-bearing material onto the surface and spurring the global aqueous chemistry shift (e.g. Bibring et al., 2006). Acidic alteration resulting from hydrothermal activity in sulfur-rich environments and/or surface weathering of mafics and phyllosilicates fueled production of sulfate minerals (Bibring et al., 2006). Most carbonates are Mg-rich and occur in association with olivine and Mg-bearing clays (Ehlmann et al., 2008b). Mg-carbonates have been identified in the Syrtis Major region (e.g. Ehlmann et al., 2008; Ehlmann and Mustard 2012) and may have formed (Brown et al., 2010) similarly to an Mg-phyllosilicate-carbonate regime in Western Australia developed via hydrothermal alteration of basalt (Brauhart et al., 2001; Brown et al., 2005).

Most mineral detections on Mars have been made from orbit; however, landed spacecraft have allowed for analyses on much finer scales, albeit spatially-limited.

1.3 History and Evolution of Ground-Based Reflectance Spectroscopy on Mars

Mars rovers and landers have used stereoscopic multispectral imagers as essential tools for interpreting surface mineralogy. These imagers consist of a dual charge-coupled device (CCD) camera system equipped with spectral filters in the VNIR range that allow throughput of strategically chosen wavelengths – individual images from each spectral filter are combined to form three-dimensional image 'cubes' (e.g., Gat, 2000). The success of ground-based multispectral imagers on Mars since the 1970s is the heritage of Mastcam-Z.

Viking 1 and 2

The Viking Lander Camera System (LCS) pioneered multispectral imaging on the surface of Mars, imaging with six VNIR spectral filters spanning 400-1000 nm (Mutch et al., 1972). LCS determined the first ground-based spectral endmember rocks on Mars, capturing albedo differences between 'palagonitic dust,' 'dark rocks,' and 'blocky material' exposed by the spacecraft's descent engine (Arvidson et al., 1989).

Mars Pathfinder

Mars Pathfinder (Golombek et al., 1997) used the Imager for Mars Pathfinder Experiment (IMP) – a stereoscopic, multispectral imager consisting of two eyes 15 cm apart on a cylindrical mast, snapping images using 12 spectral filters covering 440-1000 nm. IMP's Pixel resolution was 512x512 with an angular resolution of 0.98 mrad/pixel (Smith et al., 1997). Multispectral observations revealed seven (three rock and four soil) spectral endmember units at the confluence of the Ares and Tiu flood channels

(Smith et al., 1997) and spectral signatures consistent with the presence of low-Ca pyroxene, olivine, nanophase goethite, akaganeite, maghemite, and/or schwertmannite (Bell et al., 2000; Bell et al., 2002).

Mars Exploration Rover (MER) Spirit and Opportunity Rovers

In 2004, the Spirit and Opportunity rovers, landed in the Gusev Crater (home to the Columbia Hills) and Meridiani Planum (Arvidson et al., 2006; Squyres et al., 2006), respectively, three weeks apart. Both rovers were equipped with Panoramic Camera (Pancam), an 8-filter stereoscopic multispectral imaging system covering the 400-1100 nm range (Bell et al., 2003; Bell et al., 2006). Pancam captured panoramic images detailing spectral variation across landscapes with a focal length of 43 mm, pixel resolution of 1024x1024, and an angular resolution of 0.28 mrad/pixel (Gunn and Cousins, 2016). Pancam's filter set in conjunction with other MER instrument data, has identified signatures consistent with the presence of ferric oxides, such as hematite, manganese oxides observed in distinct-color rock coatings, and phyllosilicate-rich rock (Farrand et al., 2016). In the Columbia Hills, spectra of opaline silica-bearing outcrops and soils observed by Spirit's Pancam exhibited a steep negative slope between the 934 nm and 1009 nm filters (Wang et al., 2008). Rice et al. (2010) showed that a diversity of hydrated minerals exhibit a similar spectral signature in this range due to the $2\nu_1 + \nu_3$ H_2O combination band and/or $3\nu_{OH}$ overtone (e.g., Herzberg, 1945; Bayly et al., 1963; Clark et al., 1990), demonstrating that the width and band center of this hydration band varies significantly among different hydrated minerals. In spectra of mineralized veins at Endeavor Crater, Pancam also observed a steep negative slope between the 934 nm and 1009 nm filters (e.g. Farrand et al., 2013, 2016). In combination with measurements of $CaSO_4$ from the rover's Alpha Particle X-ray Spectrometer (APXS), the presence of this absorption allowed for the identification of the hydrated Ca-sulfate gypsum (Squyres et al., 2012). Pancam lacked an additional filter between 934 and 1009 nm, limiting the ability to resolve the ~950-1000 nm hydration feature for all hydrated minerals (Pancam cannot detect the feature when it is centered shortward of ~980 nm; Rice et al., 2010). Mastcam-Z will have a new filter within this range (to

be discussed in Section 1.4), and it will be important to understand how hydrated sulfates will appear spectrally to Mastcam-Z.

Phoenix Mars Lander

Phoenix's Surface Stereo Imager (SSI) imaged using numerous filters covering 450-1000 nm with a 1024x1024 pixel resolution and 0.24 mrad/pixel angular resolution (Lemmon et al., 2008). Phoenix's arm excavated periglacial material, exhuming high-albedo soils showing resolvable absorption bands at ~967 nm thanks to three-filter coverage at 931 nm, 967 nm, and 1002 nm. Additional analyses constrained Mg/Ca-perchlorates as the source of observed hydration bands (Cull et al., 2010a). Spectra of 'snow-white material' exhumed by Spirit also exhibited a resolvable hydration band in this wavelength region – this material was confirmed to be near-pure H_2O ice (Cull et al., 2010b). When intermixed with >1 wt% of the surrounding soil, the hydration band in this ice was masked, showing that martian dust/soil contamination can significantly hinder the depth of VNIR hydration bands. SSI demonstrated the usefulness of an additional filter in the ~950-1000 nm range, providing better resolution of hydration band morphology.

Mars Science Laboratory (MSL) Curiosity Rover

Landing in Gale Crater in 2012, Curiosity, the most recent and sophisticated rover mission to date (Grotzinger et al., 2015), hosts Mastcam, the direct successor to Pancam. Mastcam is a stereo multispectral imager with 12 VNIR spectral filters and, for the first time on any ground-based Mars spectrometer, an RGB Bayer filter (produces true-color visible imagery). Mastcam possesses asymmetrical focal lengths – 100 mm (M-100) in one eye and 34 mm (M-34) in the other. Pixel resolution is 1200x1200, M-100 angular resolution is 0.074 mrad/pixel and M-34 angular resolution is 0.22 mrad/pixel. Mastcam assisted in discoveries at Gale Crater indicative of an ancient fluvio-lacustrine environment (e.g. Grotzinger et al., 2014, 2015). Multispectral observations with Mastcam have

returned spectral features consistent with iron oxides (including nanophase) and iron-rich silicates (Wellington et al., 2017). Cross-cutting white veins found to contain calcium-sulfates (Nachon et al., 2014; Vaniman et al., 2014a) showed spectra with a negative slope between the 937 nm and 1013 nm filters. Various hydrated sulfates, water ice, and natron show absorption bands in laboratory resolution consistent with the slope observed in Mastcam spectra (Rice et al., 2013). Mastcam lacks a filter between 937 nm and 1013 nm to better resolve the band and hydration bands in the ~950-1000 nm range could be characterized more completely with additional filters.

1.4 Future Multispectral Imagers: Mastcam-Z on Mars-2020

Mars-2020 Rover

Mars-2020, the next chapter in martian surface exploration, will scan and scour the surface for new clues regarding Mars' planetary evolution. Mars-2020's Science Definition Team Report outlined four critical scientific mission objectives (Mustard et al., 2013):

A. Explore an astrobiologically relevant ancient environment on Mars to decipher its geological processes and history, including the assessment of past habitability.

B. Assess the biosignature preservation potential within the selected geological environment and search for potential biosignatures.

C. Demonstrate significant technical progress toward the future sample return of scientifically selected, well-documented samples to Earth.

D. Provide an opportunity for contributed HEOMD or Space Technology Program (STP) participation, compatible with the science payload and within the mission's payload capacity (this objective is not related to geologic/astrobiological investigation and is of no concern for this thesis).

Objective C is new in Mars exploration. Fitted with a first-of-its-kind drilling and caching system, Mars-2020 will core and collect rock samples for future retrieval. Selection of scientifically compelling samples is crucial and Mastcam-Z will play a critical role in this capacity by helping mineralogically characterize surface materials. At the time of this writing, three sites are being evaluated to serve as Mars 2020's field area: the Columbia Hills (formerly explored by MER Spirit), Northeast Syrtis Major, and Jezero Crater. The geology, context, and rationale for visiting each site will be discussed in Chapter 3.

Mastcam-Z

Mastcam-Z, the "eyes" of NASA's Mars-2020 rover (Bell et al., 2016), is a stereoscopic pair of zoomable CCD cameras providing broad-band red/green/blue (using the same Bayer filter as Mastcam), narrow-band VNIR color, and direct solar images. Unique zoom functionality allows for coverage of horizontal fields of view between 23° and 6° (Gunn and Cousins, 2016). Like previous imagers, Mastcam-Z's filters obtain spectra in the 400–1100 nm wavelength range to distinguish signatures consistent with important Fe-bearing minerals that show absorption features in VNIR. To be more sensitive to mineralogical diversity detected in the past decade (as summarized in Section 1.2 above), Mastcam-Z has improved positioning of narrowband filters. A new ~975nm filter will improve resolution in the region of the ~950-1000 nm VNIR hydration band found in hydrated sulfates, hydrated perchlorates, hydrated carbonates, hydrated silica, some phyllosilicates, and H_2O ice (e.g. Hunt, 1977). A new ~600 nm filter will help characterize Fe^{3+}-bearing material that may show an absorption band near 530 nm (e.g. Kong et al., 2011). Both eyes contain RGB filters and an 805 nm stereo filter. The left eye contains filters spanning 445-805 nm and the right eye contains filters spanning 805-1013 nm. Mastcam-Z's filter design provides spectral coverage superior to Pancam and Mastcam (Figure 3). The instrument will sit atop the mast of the rover and use a calibration target, based on the design of the Mastcam calibration target (Figure 4). The calibration target is a mounted disc of circular stripes and plates – each an ideal representation of the specific wavelengths each filter is sensitive to – used to calibrate imagery as

described in Wellington et al. (2017) and Bell et al. (2017). While Mastcam-Z has heritage with previous instruments, this specific spectral filter arrangement is the first of its kind. This work will investigate this filter set's capabilities with respect to VNIR hydration bands for the first time. Because the Mars-2020 mission seeks to investigate and sample an astrobiologically-relevant paleoenvironments (a classification that requires signs of past aqueous activity), it is crucial that we develop an understanding of how Mastcam-Z's improved resolution will view VNIR hydration bands.

In summary, the sources of VNIR spectral variability on Mars are still poorly understood, particularly as they relate to hydrated sulfate minerals and the prominent geologic units present at the Mars-2020 candidate landing sites. Mastcam-Z's new filter set will provide the opportunity to characterize hydration bands in new ways. However, how these hydration bands will appear to Mastcam-Z's first-of-its-kind filter set remains unknown, as does how Mastcam-Z can most effectively be used to corroborate spectral detections made with orbital instruments. The work described in the proceeding chapters addresses these gaps in knowledge. The following two chapters will describe how Mastcam-Z will view hydration bands in sulfates at varying conditions, what Mastcam-Z filters are most effective for capturing signs of hydration in sulfates, what Mastcam-Z filters can be used to corroborate spectral detections made from orbit at each Mars-2020 candidate landing site, and the primary controls on VNIR spectral variability on the surface of Mars.

2.0 CHARACTERIZING VISIBLE TO NEAR-INFRARED SPECTRA OF HYDRATED SULFATES IN MASTCAM-Z RESOLUTION

2.1 Introduction

2.1.1 Hydrated Sulfates on Mars

Sulfate minerals on Mars are important environmental indicators. As stated in Section 1.3, the presence of widespread sulfate mineral deposits on Mars indicates a period of significantly sulfur-rich

aqueous environments as H_2SO_4 was precipitated onto the surface following major volcanic outgassing events (e.g. Bibring et al., 2006). Thus, the presence of hydrated sulfate minerals in any given region allows for the possibility that acid-sulfate hydrothermal environments existed in that location in the distant past. These environments are important for understanding Mars' aqueous history and provide regions of interest to search for indications of past habitability. Constraining Mastcam-Z's ability to detect hydrated sulfate minerals directly supports exploration of these environments. Effectively identified hydrated sulfates can be further analyzed by other instruments on the Mars-2020 payload, cached for the future sample return mission, and allow for the interpretation of past aqueous environments at the chosen landing site. Because hydrated sulfates encountered on Mars will likely be intermixed with different endmembers and/or iron oxide dust, this research also analyzes how such mixtures will affect the crucial ~950-1000 nm hydration band. Constraining the spectral trends that occur with mineral mixtures and dust contamination allows for quantification of potential hinderances to Mastcam-Z's ability to detect hydration in sulfates and offers insights into the general variability of this understudied VNIR absorption band.

Ca/Mg-sulfates have been identified in a variety of regions on Mars. Magnesium and calcium sulfates are common in martian regolith (Vaniman and Chipera, 2006) and exist in multiphase dehydration/rehydration systems with concentrations of different species varying based on local environmental conditions (Vaniman and Chipera, 2006). Mg-sulfates are expressed in surface material as monohydrated kieserite, stable in near-equatorial latitudes during the martian summer, and polyhydrated epsomite, the result of kieserite rehydrating at higher latitudes (Vaniman and Chipera, 2006). Laboratory experiments demonstrated that kieserite can also hydrate to hexahydrite (Vaniman et al., 2004). Sulfur-rich soils were identified in Gusev Crater by the Spirit rover (Yen et al., 2008) using the alpha-particle X-ray spectrometer (Squyres et al., 2003) and the Mossbauer Spectrometer (MB; Squyres et al., 2003). Elemental analysis of these soils revealed the presence of Fe(III)-, Mg-, and Ca-bearing

sulfate phases. Sulfate material was also observed *in situ* at Meridiani Planum by the Opportunity rover (Squyres et al., 2012). A large vein unit at Endeavor Crater dubbed 'Homestake' contained significant amounts of SO_3 and Ca, signaling the presence of Ca-sulfates (Squyres et al., 2012). Multispectral imagery was used in conjunction with APXS analyses, revealing the notable negative slope between the 934 nm and 1009 nm filters, indicative of hydration. At Gale Crater, anhydrite, bassanite, and gypsum have been observed to coexist in a dehydration series within fracture-filling vein deposits (Nachon et al., 2014; Vaniman et al., 2017). Curiosity ChemMin XRD data from vein samples reveal that gypsum is primarily concentrated at depth and dehydrates to bassanite when exposed to ambient conditions (Vaniman et al., 2017), while anhydrite occurs both at depth and on the surface. OMEGA has identified kieserite, gypsum, and unconstrained polyhydrated sulfate material in layered sedimentary deposits at a variety of locations on Mars (Gendrin et al., 2005). Surface analysis with CRISM has yielded signatures of bassanite in the Mawrth Vallis region (Wray et al., 2010), jarosite and unconstrained polyhydrated sulfates in NE Syrtis (Ehlmann and Mustard, 2012), and layered Mg-sulfates in Gale Crater (Milliken et al., 2009), among numerous other identifications.

As previously stated, the sulfate deposits that will be encountered by Mastcam-Z are unlikely to be homogenous; intimate mixtures of various hydrated sulfate species are more likely (e.g., Vaniman et al., 2013). Mineral mixtures are difficult to discern in VNIR spectra because of non-linear mixing effects. Due to the close combination of endmember particles in intimate mixtures, incident light undergoes multiple interactions with each endmember, leading to non-linear combinations of the spectral properties of endmember constituents in an acquired spectrum (Hapke, 2012). Mixture spectra can be modeled in some cases to estimate the proportions of each endmember, but simple linear mixing models break down when applied to intimately mixed samples (Hapke, 2012). Various statistical methods to 'unmix' intimate mixture spectra have been developed and tested (e.g. Broadwater and Banerjee, 2010; Nascimento and Bioucas-Dias, 2010; Hapke, 2012) and effective spectral unmixing

models for combinations of Mars-relevant clays and epsomite have been explored (Stack and Milliken, 2015). However, additional model testing with other Mars-relevant minerals is required before we can confidently rely on models (instead of manually creating and analyzing mixtures in the lab) to understand how rover spectrometers will visualize mixture spectra in the field. This thesis does not test statistical unmixing methods, but will discuss the non-linear spectral effects of hydrated sulfate mixtures. The dataset herein could prove useful to further test the effectiveness of unmixing models on Mars-relevant mixtures in future work.

2.1.2 Hydrated Sulfates Investigation

This work spectrally investigates synthetic varieties of several calcium and magnesium sulfates (Table 1). Ca- and Mg-sulfate phases were selected that have been either explicitly detected on Mars or theoretically inferred to be stable at the surface. To support identification of hydration in these phases with Mastcam-Z, five key hypotheses are tested:

1) The ~975 nm filter will allow Mastcam-Z to detect the ~950-1000 nm band in hydrated sulfates when used in tandem with the ~1013 nm and ~937 nm filters.

2) Bimodal mixtures of hydrated sulfates will mask or shallow the ~950-1000 nm band at Mastcam-Z's spectral resolution due to varying hydration states.

3) Minor (5% sample vol.) martian dust contamination will mask the ~950-1000 nm band at Mastcam-Z's spectral resolution due to the absorptions of iron oxides in VNIR.

4) Mastcam-Z will not have uniform sensitivity to hydration in sulfates at all grain sizes

(strength of the ~950-1000 nm absorption band is dependent on grain size).

5) Bimodal mixtures of hydrated sulfates will experience nonlinear mixing effects that cannot be accurately described by standard linear spectral mixing models.

To address these hypotheses, we created bimodal mixtures of these sulfates and analyzed them in VNIR with a laboratory spectrometer. The outcome of this work is a dataset consisting of band depth and band position information for a variety of imposed conditions, as well as suggestions for the use of the Mastcam-Z spectral filter set to constrain hydration in Ca/Mg-sulfates. The 937 nm, 975 nm, and 1013 nm filters are used to determine what filter combinations are most sensitive to signs of this hydration (i.e. must all three filters be used in tandem as hypothesized or could two-filter combinations reasonably detect hydration from the resulting slope between them?)

2.2 Methods

An Analytical Spectral Devices, Inc. (ASD) Field Spec 4 Wide-Res (WR) spectrometer was used for data collection. The Fieldspec 4 WR is a 2151 channel spectrometer offering VNIR spectral coverage from 350-2500 nm at a spectral resolution of 3 nm from 350-700 nm and 30 nm at 701-2500 nm. Scan time is 100 ms with a 0.1 nm reproducibility and 0.5 nm accuracy. Spectral bandwidth is 1.4 nm at 350-1000 nm and 1.1 nm at 1001-2500 nm. The spectrometer has three detectors: a VNIR detector capturing 350-1000 nm composed of a 512-element silicon array, SWIR detector 1 capturing 1001-1800 nm, and SWIR detector 2 capturing 1801-2500 nm. Both SWIR detectors are composed of a graded index InGaAs photodiode. The spectrometer absorbs light with a 1.5 m fiber optic with a 25° field of view. The fiber optic is attached to a contact probe at a fixed viewing angle of 35°. The light source – contained within the contact probe – is a 6.5 W halogen lightbulb with a color temperature of 2901 +/- 10 °K that produces a 10-mm spot size light. The stray light specification is 0.02 % in VNIR and 0.01 % in SWIR 1 and 2.

Ca-sulfate mixtures were made from synthetic anhydrite, bassanite, and gypsum purchased from Sigma Aldrich. Vendor documents indicate ≥97% purity for each sample. Two series of sample powders were created: bimodal mixtures and single phases at varying grain size. Bimodal mixtures were

created by volumetrically mixing anhydrite-gypsum, bassanite-gypsum, and anhydrite-bassanite combinations at 10% total sample volume intervals (e.g. 90% anhydrite-10% gypsum, 80% anhydrite-20% gypsum, 70% anhydrite-30% gypsum, etc.). These bimodal mixtures were chosen to capture a range of concentrations for a Mars-like dehydration series. For bimodal mixtures, samples were gently crushed using an agate mortar and pestle and dry sieved to a grain size of 500-1000 μm. For the grain size series, gypsum was crushed and sieved to grain size fractions of 2-4 mm, 1-2 mm, 500-1000 μm, 250-500 μm, 125-250 μm, 63-125 μm, and <63 μm. A whole rock selenite sample (a lithified ~2" x 3" x 2" chunk) was also used to analyze the spectra of a solid gypsum outcrop, such as large vein deposits. Samples were stored in airtight sample cups to protect against long-term exposure to ambient humidity. Mixtures were thoroughly agitated with a plastic stirrer to randomly distribute particles. These methods were repeated for the magnesium sulfate minerals, with epsomite selected for the grain size series. Whole rock epsomite, however, was not available for this study and no proxy for cohesive Mg-carbonate outcrop is assessed. Trimodal mixtures were not explored given the difficulty that would accompany attributing changes in spectral properties to the relative abundances of each individual phase. Cross-class mixtures of Ca- and Mg- sulfates were also not investigated. Trimodal and cross-class hydrated sulfate mixtures remain an intriguing subject for a future, expanded study.

Reflectance spectra of each sample were measured in a dark room to limit stray light contamination. Sample powders were analyzed in custom-made aluminum sample holders fashioned to be the same diameter as the contact probe. The contact probe was held in place using a ring stand while an adjustable platform raised sample cups into contact with the probe (Figure 5). This minimized the escape of light reflected by the sample and further shielded the detector from ambient light. Sample holders and the contact probe were cleaned between samples. Contamination is not a significant risk with such easily removable powders. Cleaning with condensed air and kimwipes removed all visible powder and no spurious features were observed in resulting spectra. Spectral measurements were

made 1000 times for each sample – and averaged into a single spectrum – to minimize noise. White and dark reference spectra are required for calibration of sample spectra and were acquired using a Spectralon white standard at the start of laboratory work. Heating of the instrument during operation can cause these reference values to deviate slightly if not regularly calibrated. A dark current and white reference measurement was retaken every 10 minutes to mitigate this issue. A splice correction was applied using ASD software to correct for "jumps" in reflectance at wavelengths where detector change occurs (1000 nm and 1800 nm).

Following analysis of uncontaminated powders, a subset of the gypsum-anhydrite and epsomite-kieserite mixtures were mixed with JSC Mars-1, a Mars dust simulant (Allen et al., 1997), and new spectra were acquired. JSC Mars-1 is composed of <1 mm weathered volcanic ash from the Pu'u Nene volcanic in Hawaii. The dust simulant was dry sieved to <500 µm before being mixed with sulfate samples. While there are numerous Mars dust simulants, JSC Mars-1 represents a close spectral match to dusty regions on Mars and has become the industry standard for Mars analog studies and has been used/compared in analog studies of Mars covering a wide range of topics (e.g. Moroz et al., 2009; Phebus et al., 2011; Johnson et al., 2017). JSC Mars-1 was introduced at 5% total volume of the sample. Five percent dust contamination simulates the minimum amount of dust observed on any martian surface, even after attempts to remove dust with rover equipment. The dust simulant was mixed into the samples with a plastic stirrer for over one minute to randomly distribute particles. A subset of dust contaminated Ca-sulfate samples were re-mixed and measured a second time to discern if any significant variations occurred in dust distribution in the sample. No significant spectral differences were observed.

Absolute reflectance values were used for data processing and analysis. Laboratory resolution band depths for the hydration band were calculated by creating straight-line continuums over the spectral absorption and applying the equation $D_B \equiv (R_C - R_B)/ R_C$ (Clark and Roush, 1984). D_B is the band

depth, R_C is the reflectance of the continuum line at the band center wavelength, and R_B is the reflectance of the spectrum at the band center wavelength (Figure 6). Left and right shoulder positions chosen to calculate straight-line continuums for laboratory spectra were 960 and 1050 nm.

Each spectrum was convolved to Mastcam-Z resolution by integrating over Mastcam-Z's hypothetical filter transmission profiles, roughly Gaussian curves centered on specific wavelengths (Figure 7). Given that Mastcam-Z's filters have not been manufactured yet, the hypothetical transmission profiles used are replicas of the Mastcam filter transmission profiles. The profile of the 805 nm filter was copied and shifted to create hypothetical bandpasses for the new ~600 nm and ~975 nm filters that are unique to Mastcam-Z. The convolution script removes spectral data outside of the Gaussian transmission profile for each filter, simulating the spectrum Mastcam-Z would capture. Deconvolved spectra were over-plotted on original spectra to visualize data loss at Mastcam-Z resolution. To aid in discrimination of sulfate hydration signatures with Mastcam-Z, this work searched for the filter combination most sensitive to the ~950-1000 nm hydration band. Ideal filter combinations can then be used to optimize investigation of hydration signatures with Mastcam-Z. To that end, three Mastcam-Z convolved band depths were calculated (Figure 8): the center band depth of 975 nm (with 937 nm and 1013 nm as shoulder positions), the depth of 1013 nm below 937 nm (937-1013 band depth), and the depth of 975 nm below 937 nm (937-975 band depth). The 975 nm center band depth was calculated for the convolved spectra with 1013 nm and 937 nm used as shoulder positions. The 937-975 band depth and 937-1013 band depth were calculated using the equations $(R_{937} – R_{975})/R_{937}$) and $(R_{937} – R_{1013})/R_{937}$) where R_{xxx} is the reflectance at the specified wavelength.

The 975 nm center band depth, 937-1013 band depth, and 937-975 band depth for each sample were compared to that of a selected 'base sample.' For bimodal mixtures, the base sample was 100% of the more hydrated phase (e.g. 100% gypsum for gypsum-bassanite mixtures, 100% hexahydrite for hexahydrite-kieserite mixtures, etc.). The percent reduction of band depths (shallowing of the band) of

mixture samples from band depths of the base sample was quantified. For the gypsum and epsomite grain size series, the base sample was the coarsest sample of each mineral (whole rock selenite for gypsum and 2-4 mm for epsomite). For dust contaminated samples, the corresponding dust-free mixture was chosen as the based for each contaminate sample.

Measured in the laboratory prior to launch (Bell et al., 2017), the 445 nm Mastcam filter has some out of band transmission sensitive to light outside the intended effective wavelength range (Figure 9). Because the hypothetical Mastcam-Z transmission profiles used in this work are based on the official Mastcam transmission profiles, the aggregate of this noise can cause a significant vertical offset of 445 nm reflectance in a convolved spectrum. The Mastcam calibration process corrects this error to some degree. To correct for this issue, throughput of the 445 nm band at wavelengths >460 nm and <420 nm was reduced to 0, producing more accurate convolved spectra (Figure 10).

All spectra from this work have been uploaded to our online interactive spectral database (http://spectro.geol.wwu.edu/). The database combines data from the University of Winnipeg Planetary Spectrophotometer Facility (HOSERLab; Cloutis et al., 2006), the United States Geological Survey (USGS) Spectral Library (Kokaly et al., 2017), Brown University's Keck/NASA Reflectance Experiment Laboratory (RELAB; Pieters and Hiroi, 2004), Crowley et al., 1991 spectra of several playa evaporate minerals, the Advanced Spaceborne Thermal Emission and Reflectance Radiometer (ASTER) Spectral Library (Baldridge et al., 2009), and the Mastcam-Z team's spectral library of Mars-relevant minerals. The database was created by undergraduate computer science students at Western Washington University under the direction of Dr. Melissa Rice and myself, and is currently being maintained by students in our Mars science research group. This database has been made available to members of the Mars-2020 and MSL science teams to aid their spectral investigations.

2.3 Results

Observed spectral trends will be discussed in this result section. Trends in band depths for all samples are often too small to see with the naked eye. Tables (Tables 2-5) have been included in a supplementary section at the end of this chapter to house numerical band depth data that cannot be constrained visually.

2.3.1 Grain Size Series

Gypsum

The overall selenite spectrum has a steep negative slope toward longer wavelengths (Figure 11). Band center position is 1001 nm in all samples (Table 2). Overall, laboratory resolution band depths increase with grain size (Table 2). In powdered samples (excludes selenite), band depth peaks at 500-1000 μm (Table 2).

In Mastcam-Z convolved spectra, a similar grain size trend is observed: increasing band depth with increasing grain size. The 975 nm center band depth generally increases with grain size (Table 2). Mastcam-Z convolved band depths are shallower than laboratory resolution band depths at all grain sizes and of the convolved bands, the 975 nm center band exhibits the smallest bands depths at each size fraction (Table 2). Percent reduction of band depths from the selenite base sample generally decreases with increasing grain size, however this trend breaks down at grain sizes >1000 μm (Table 2).

Epsomite

All epsomite samples >500 μm show a slight negative slope toward longer wavelengths in the overall spectra (Figure 11). Band position varies from 998-1001 nm (Table 2). Laboratory resolution band depths increase with grain size while band position exhibits no notable trend (Table 2). Band depth peaks at 1000-2000 μm (Table 2).

Mastcam-Z convolved band depths also increase with grain size (Table 2). The 975 nm center band shows the smallest band depths (Table 2). Lab resolution bands are typically larger than convolved bands (Table 2). Deconvolved band depths peak at 500-1000 μm and percent reduction of band depths from the 2000-4000 μm sample generally decreases with increasing grain size (Table 2).

2.3.2 Bimodal Mixtures

Gypsum-Anhydrite

Anhydrite-bearing overall spectra slope positively toward longer wavelengths (Figure 12). Pure gypsum has a negative overall slope (Figure 12). Pure anhydrite, a nominally anhydrous mineral, exhibits a minor hydration band (Figure 11 and Table 3). Lab resolution band depth increases with gypsum concentration (Table 3). Band position ranges from 964 nm-1001 nm and shifts toward longer wavelengths with increased gypsum concentration (Table 3).

All Mastcam-Z band depths decrease significantly with increased anhydrite concentration (Table 3). Some samples exhibit slightly negative band depths, indicating that no absorption band exists (Table 3). Lab resolution band depths are generally larger than Mastcam-Z band depths (Table 3). Percent band depth reduction increases with anhydrite concentration and this effect is most pronounced for the 937-1013 band depth (Table 3).

Gypsum-Bassanite

Bassanite-bearing overall spectra slope positively toward longer wavelengths (Figure 12). Lab resolution band depth ranges increases with gypsum concentration (Table 3). Band position varies from 964-1001 nm and, like gypsum-anhydrite mixtures, shifts to longer wavelengths as gypsum concentration increases (Table 3).

Mastcam-Z band depths decrease with increasing bassanite concentration (Table 3). The 937-1013 band depth is negative at concentrations of 0-90% (Table 3). The 937-975 band depth is negative at concentrations of 0-70% gypsum (Table 3). Percent band depth reduction increases with bassanite concentration and, like gypsum-anhydrite mixtures, this effect is most prominent in the 937-1013 band depth (Table 3).

Bassanite-Anhydrite

All overall spectra slope positively toward longer wavelengths (Figure 12). The lab resolution band position varies between 964-969 nm, showing no systematic trend with mineral concentration (Table 3). Lab resolution band depth also exhibits no notable trend with mineral concentration (Table 3).

Both the 937-1013 band depth and the 937-975 band depth are negative at all tested concentrations (Table 3). Like in lab resolution spectra, no band depth trends are observed at Mastcam-Z resolution (Table 3). Percent band depth reduction varies significantly in both laboratory and Mastcam-Z resolution, with several negative reductions, indicating hydration bands deeper than that of the base sample (Table 3).

Epsomite-Kieserite

All overall spectra slope negatively toward longer wavelengths and slope steepens with increased epsomite concentration (Figure 13). Lab resolution band depth increases with increasing epsomite concentration (Table 4). Band position for all samples of 20% or greater epsomite is 1001 nm (Table 4). Pure kieserite shows a lab resolution band position of 1024 nm and the addition of 10% epsomite shifts this band to 998 nm (Table 4).

The 975 nm center band depth, 937-1013 band depth, and 937-975 band depth all increase with epsomite concentration (Table 4). The 937-1013 band depth and 937-975 band depth exceed the 975

nm center and laboratory resolution band depths in all mixtures (Table 4). Percent band depth reduction increases with kieserite concentration (Table 4).

Epsomite-Hexahydrite

Lab resolution band position ranges from 985-1001 nm, generally shifting toward longer wavelengths with increased epsomite concentration (Table 4). Lab resolution band depth increases with increasing epsomite concentration (Table 4).

The 975 nm center band depth exhibits no concentration trend, while the 937-1013 band depth and 937-975 band depth increase with epsomite concentration (Table 4). Like epsomite-kieserite mixtures, the 937-1013 band depth and 937-975 band depth are larger than the 975 nm center and laboratory resolution band depths (Table 4). Percent band depth reduction increases with hexahydrite concentration for the 937-1013 band depth and 937-975 band depth (Table 4). Reductions of the 975 nm center band depth are significantly lower and follow no observable trend (Table 4).

Hexahydrite-Kieserite

Lab resolution band depth increases with increasing hexahydrite concentration (Table 4). Band position generally shifts toward shorter wavelengths with increased hexahydrite concentration, although this trend shows some variance (Table 4).

All Mastcam-Z convolved band depths increase with increasing hexahydrite concentration (Table 4). Overall, the 975 nm center band depths are greater than lab resolution band depths, yet smaller than the 937-1013 band depths and 937-975 band depths (Table 4). Percent band depth reduction from 100% hexahydrite increases with kieserite concentration at laboratory and Mastcam-Z reduction (Table 4).

2.3.3 Dust Contamination Series

Dust Contaminated Gypsum-Anhydrite

All overall spectra slope positively toward longer wavelengths; this slope is steepest from ~400-750 nm (Figure 14). Laboratory resolution band depth is smaller in contaminated versus uncontaminated samples, and exhibits no concentration trend (Table 5). Band position varies from 961-992 nm, shifting to longer wavelengths with increased gypsum concentration (Table 5). Uncontaminated samples show band positions shifted toward longer wavelengths (Table 5).

The 937-1013 band depth is negative at all concentrations and the 937-975 band depth is negative at concentrations of 0-80% gypsum (Table 5). The 975 nm center band depth is negative for 100% anhydrite and band depth increases with increasing gypsum concentration (Table 5). Although the 937-1013 band depth and the 937-975 band depth are largest in the 100% gypsum sample, no concentration trend exists for these features (Table 5). Percent band depth reduction of the 975 nm center band depth from uncontaminated samples increases with increasing anhydrite concentration (Table 5).

Dust Contaminated Epsomite-Kieserite

All overall spectra slope positively toward longer wavelengths and, similarly to the gypsum-anhydrite sample set, the slope is steepest at shorter wavelengths (Figure 14). Laboratory resolution band depth increases with increasing epsomite concentration and is significantly smaller than in uncontaminated samples (Table 5). Band position ranges from 975-1001 nm, shifting toward longer wavelengths with increased epsomite concentration (Table 5). Apart from 100% epsomite, contaminated sample band positions are at shorter wavelengths than their uncontaminated counterparts (Table 5).

Overall, Mastcam-Z convolved band depths increase with increasing epsomite concentration (Table 5). The 937-1013 band depth is negative from 0-40% epsomite and the 937-975 band depth is negative from 0-20% epsomite (Table 5). Percent band depth reduction from uncontaminated samples increases with increasing kieserite concentration (Table 5).

2.4 Discussion

This data reveals several key trends in the variation of the ~950-1000 nm absorption band. Important takeaways regarding the effects of mineral mixing, grain size, and dust contamination gleaned from this dataset are valuable to future Mastcam-Z operations.

2.4.1 Hydration Feature Detectability

Internal sources of Mastcam-Z instrument error have yet to be characterized. Instrument errors for the Pancam instrument were found to be <1% (Bell et al., 2006), indicating that any band depth greater than 1% can be considered a positive detection and not spectral noise. Anticipating similar instrument error to that of Pancam, a band depth ≥0.01 (1%) is considered potentially detectable to Mastcam-Z. The following section summarizes what minerals and conditions exhibit detectable bands (Figures 15 and 16), and what this means for Mastcam-Z operation.

Grain Size Series Detectability

Pure gypsum samples show a detectable 975 nm center band depth at grain sizes 250-500 µm or greater (Figure 16; bands <0.01 are too small for detection). The 937-1013 band depth is detectable at all grain sizes 63-125 µm or greater and the 937-975 band depth is detectable at all grain sizes (Figure 15). The band is centered at 1001 nm (Table 2), but laboratory spectra reveal that this band is wide enough to be captured by Mastcam-Z's filter set (Figure 11). The 937-975 band depth shows detectable depths at all grain sizes and is the ideal filter combination to analyze potential gypsum on Mars.

In pure epsomite, the 975 nm center band depth, 937-1013 band depth, and 937-975 band depth are detectable at all tested grain sizes (Figure 15). Lab resolution band center ranges from 998 – 1001 nm, but similarly to gypsum, Mastcam-Z's filter set can capture this band given its width (Table 2). The 937-1013 band depth shows the largest bands depths for pure epsomite and represents the most effective filter combination for constraining hydration in potential martian epsomites.

Bimodal Mixtures Detectability

Results show that even small amounts of anhydrite masks hydration bands in gypsum-anhydrite mixtures. The addition of a mere 10% sample volume amount of anhydrite results in a band depth reduction that drives the 975 nm center band depth and 937-1013 band depth below the 1% detection threshold (Figure 16). The 937-975 band depth remained detectable with 10-20% anhydrite, but at >20% anhydrite, detection of hydration bands in gypsum-anhydrite mixtures fails (Figure 16). Larger grain sizes were demonstrated to produce more significant band depths. 500-1000 μm may represent the finest size of an anhydrite-gypsum mixture possessing detectable hydration signature and larger grain sizes of this mixture may prove more favorable. Gypsum-bassanite mixtures exhibit no detectable hydration band at any concentration (Figure 16). Larger grain size mixtures may be detectable, but with a mere 10% bassanite addition rendering bands at 500-1000 μm undetectable, detection of consistently shallow Ca-sulfate hydration bands may be difficult. The 975 nm center band depth consistently shows the deepest bands out of the three tested features. To constrain hydration in gypsum-bassanite mixtures, if larger grain sizes of this mixture are to be encountered on Mars, the 937 nm, 975 nm, and 1013 nm filters should be used in tandem. Pure bassanite and bassanite-anhydrite mixtures lack a detectable band depth at any tested condition. Percent reductions of these band depths show no clear trend with concentration; assumptions cannot be made about the ability to detect hydration in bassanite-anhydrite mixtures at larger grain sizes.

Pure kieserite at 500-1000 µm lacks a detectable 975 nm center band depth (Figure 16). Epsomite-kieserite mixtures have detectable hydration bands at all concentrations. Addition of 90% kieserite reduces the 937-1013 band depth and 937-975 band depth significantly, but the resulting band depths remain more than double the detection threshold. For the 975 nm center band depth, 90% kieserite results in a band that is barely detectable (Figure 16). Hydration is likely detectable in epsomite-kieserite mixtures at smaller grain sizes where band depths shallow, although the 975 nm center band depth may be less effective when more kieserite is present. The 937-975 band depth is the deepest band in this sample set and recommended for analyzing potential epsomite-kieserite mixtures. Epsomite and hexahydrite mixtures exhibit significant absorption bands at all concentrations. Increasing hexahydrite concentration results in notable percent reduction of band depths, but none significant enough to reduce a band below 4x the detection threshold (Figure 16). Epsomite-hexahydrite mixtures retaining detectable hydration bands at smaller grains sizes is likely. The 975 nm center band depth shows no clear concentration trend. The 937-975 band depth shows the deepest bands for these mixtures and is ideal to constrain hydration in epsomite-hexahydrite mixtures. In hexahydrite-kieserite mixtures, the 937-975 band depth and 937-1013 band depth are detectable at all concentrations (Figure 16). The 975 nm center band depth becomes undetectable with the addition of 80% kieserite and 90% kieserite addition results in a barely detectable 937-1013 band depth and 937-975 band depth (Figure 16). Hydration in kieserite-dominated hexahydrite-kieserite mixtures may be troublesome to constrain at smaller grain sizes. The 937-975 band depth exhibits the deepest bands and is the advised feature to use for identifying hydration in potential hexahydrite-kieserite mixtures.

Dust Contamination Series Detectability

The addition of JSC Mars-1 significantly increases absorption at blue and green wavelengths. Rich in iron-oxides, the red-brown dust simulant absorbs light in this wavelength range. Dust contamination rendered hydration undetectable in all gypsum-anhydrite mixtures (which is expected

given that anhydrite significantly reduces hydration bands on its own), but also resulted in pure gypsum no longer showing a detectable band (Figure 16). Calcium sulfate hydration bands are characteristically weak; even 5% sample volume contamination presents significant challenge to identifying hydration in calcium sulfates. Significant absorption of blue-green light is also observed in contaminated epsomite-kieserite samples. Epsomite displays prominent hydration bands and hydration remains detectable via the 975 nm center band depth at 80-100% epsomite, 937-1013 band depth at 80-100% epsomite, and 937-975 band depth at 60-100% (Figure 16). In 100% epsomite hydration bands remain significant. Homogenous epsomite deposits may retain discernable hydration features in instances of minimal dust contamination at smaller grain sizes. Kieserite addition significantly shallows hydration bands in dust contaminated mixtures (Figure 16) and smaller grain sizes may pose challenge. The 937-975 band depth exhibits the deepest bands and is the recommended feature to use for dust contaminated Mg-sulfate deposits. Mars-2020 will likely encounter rocks with levels of dust contamination exceeding what was used in this study, based on the experience of the Curiosity mission (e.g. Bradley et al., 2017). Larger dust contents could enhance hydration band masking far beyond what is observed in this work. However, in the exceptionally dusty Columbia Hills, negative slopes between 934 and 1009 nm indicative of hydration were successfully observed with Pancam, even on Ca-sulfate veins and hydrated silica outcrops where the surface dust had not been removed (e.g. Rice et al., 2010; Farrand et al., 2016).

The dataset presented here offers critical insights on the potential use of Mastcam-Z to identify hydration in sulfate minerals. The 937-1013 band depth and 937-975 band depth generally exhibit stronger signals than the 975 nm center band depths. Apart from the grain size series samples, 937-975 band depth exceeds 937-1013 band depth. The 937-975 band depth stands as the optimal feature to constrain hydration signatures in sulfate deposits with Mastcam-Z. The addition of the 975 nm filter

improves our ability to constrain hydration signatures in hydrated sulfates, but the 937 nm, 975 nm, and 1013 nm filters may not need to be used in tandem for most situations.

Beyond Mg- and Ca-sulfates, there are numerous hydrated minerals identified on Mars (e.g. Bibring et al., 2006; Mustard et al., 2008). Previous rover spectrometers have identified signs of hydration in a number of these without the addition of an ~975 nm filter (e.g. Rice et al., 2010; Squyres et al., 2012; Vaniman et al., 2014; Farrand et al., 2016). The success of past missions in constraining hydration in other phases with and without Mastcam-Z's updated ~975 nm filter bodes well for projecting Mastcam-Z's ability to discern hydration in minerals other than the sulfates address here. Similar work is needed to constrain how band morphology and detectability changes in those phases, but it can currently be assumed that the new ~975 nm filter will prove a critical addition to constraining hydration in a multitude of other Mars-relevant hydrated minerals.

2.4.2 Operational Considerations

Several variables demand keen attention during Mars rover operation. Power availability, data volume, and time constraints guide daily operational decisions for the ongoing Curiosity rover mission, and Mars-2020 will be similar in construction and technical operation. Several key operational considerations can be gleaned from the results of this work.

Through radioactive decay of plutonium-238, Curiosity's radioisotope thermoelectric generator (RTG) consistently generates power over time (Welch et al., 2013). Energy production proceeds at a pace that meets mission needs, but depletion of on-hand power is possible. To not exceed power budget, rover operators must continuously draft, revise, compromise, and sacrifice on proposed rover activities. The RTG allows six hours of operating time each martian day (Welch et al., 2013), and the energy needs of planned observations can further constrain that time block. Every rover action – including each filter shot in a multispectral image observation – consumes power. This work

demonstrates that the 975 nm and 937 nm filters most effectively identify hydration in sulfates in *most* cases (i.e. The down-drop in reflectance between the 975 nm and 937 nm filters due to the presence of hydration is greater in more tested samples than the down-drop between the 1013 nm and 937 nm or the 975 nm center band depth). Acquiring two-filter observations, opposed to three-filter, alleviates power consumption.

Data volume presents a similar challenge. The amount of data the rover can store, transmit to relay satellites, and downlink to Earth is limited. As with power, multispectral filter image necessitates some portion of data volume be reserved. What data transits to Earth requires daily deliberation. Constraining hydration in sulfates with two filters, as opposed to three, reduces the data requirement.

Science operations adhere to specified time blocks based on factors such as illumination, thermal conditions, visibility, etc. These finite constraints also dictate rover activities. Two-filter hydration images reduce time costs, making these observations more manageable in planning phases.

2.4.3 Spectral Trends

This dataset also provides insight on the nature of VNIR hydration bands in Ca/Mg-sulfates beyond the operation of Mastcam-Z. The results presented here verify previous laboratory observations that overall reflectance increases with grain size (e.g., Clark et al., 1990). Light travels longer distances through larger grains, increasing the opportunity for photons to be absorbed in the crystal lattice (e.g. Clark and Roush, 1984; Hapke, 2012). Larger grains have lower surface area/volume ratio for reflection to occur.

In pure mineral samples at 500-1000 µm grain size, band depth increases substantially with hydration state in hydrated sulfates. Hemi-hydrated ($0.5H_2O$) bassanite shows a minimal laboratory resolution band depth of 0.0012. Epsomite ($7H_2O$) exhibits a band depth of 0.0793, ~6600% greater than bassanite and gypsum ($2H_2O$) shows a band depth of 0.0303, ~2500% greater than bassanite. Gypsum

and epsomite represent H_2O content increases of factors of four and 14 from bassanite, but the increase in band depth greatly exceeds these factors – there is positive correlation between wt.% H_2O and band depth, but it is not linear (Figure 17).

Band position for vibrational processes is governed by the mode of vibration as it relates to the molecular geometry of the given mineral. Thus, this property is not necessarily dependent on the abundance of H_2O and not expected to show any meaningful relationship with H_2O content. Results show no correlation between band position and hydration state (Figure 18). Anhydrite is not included in these figures because anhydrite hydration bands are the result of adsorbed water (see discussion in Section 2.4.1).

Spectral mixing effects in hydrated Ca/Mg-sulfates are non-linear. Generally, band depth decreases with additional mixing of less hydrated phases. However, percent band depth reduction with each 10% increment of the less hydrated phase experiences some variation (Figure 16). To test the accuracy of linear mixing modeling to characterize the spectra and absorption bands presented in this work, a simple linear mixing operation was performed on the epsomite-kieserite set. Pure epsomite and pure kieserite were linearly mixed using the equation MixedSpectrum = (Spectrum1*X) + (Spectrum2*(1-X)), where X is the decimal fraction of kieserite relative to epsomite. These modeled spectra were over-plotted with laboratory spectra (Figure 19) and band depths were calculated and compared to laboratory samples (Table 4). Modeled spectra exhibit noticeably larger band depths in most cases than laboratory spectra and are more reflective at shorter wavelengths. Error in band depth ranges from 6.3-38.5% using the linear mixing model (Table 4). In most cases the band position is shifted to 1000 nm from 1001 nm in modeled spectra (shifts from 998 nm to 1019 nm in 10% epsomite sample). It is clear from this data that linear mixture modeling is not recommended for understand the spectral properties of hydrated sulfate mixtures on Mars. The efficacy of non-linear unmixing models then becomes an important question. With known mixture concentrations, this dataset presents intriguing

opportunity to test non-linear unmixing models such as the popular Hapke model (Hapke, 2012) which was applied to phyllosilicate and sulfate mixtures by Stack and Milliken, 2015 and the Shkuratov model (Shkuratov et al., 1999) used on mafic minerals by Poulet and Erard, 2004.

2.4.4 Caveats and Limitations

There are a few key limitations and known sources of error in this dataset that must be addressed to aid the interpretation of results. For example, the laboratory conditions likely effected the observations of anhydrite, as the spectrum of 100% anhydrite shows a small absorption band centered at 964 nm (Figure 12). A band at this position is likely the result of hydration and suggests the presence of adsorbed water in the samples. In intrinsically hydrated minerals (all other minerals used in this study), the presence of adsorbed water contamination is difficult to discern from the structural H_2O/OH. Anhydrite, industrially used as a desiccant, readily absorbs moisture from its surroundings (Hammond and Withrow, 1933). Exposure to extant humidity during sample prep and analysis can potentially lead to water adsorption on anhydrite grains. Cloutis et al. (2006) documented similar hydration of anhydrite under ambient conditions. A humidity-controlled experiment chamber could have prevented this contamination, but was not available for this study. Hydration via ambient humidity also potentially explains pure anhydrite showing a deeper hydration band than pure bassanite. Cloutis et al. (2006) also suggests fluid inclusions or incipient alteration as potential causes of anhydrite hydration bands.

To simulate regolith contamination, samples were thoroughly mixed with the Mars JSC-1. No other methods of dust contamination, such as thin coatings, were applied. While it is anticipated that near-outcrop fragments and particulate deposits will be similarly intermixed with martian regolith, there is also the case where dust lies atop pristine material as a thin coating. This situation prevails throughout the bulk of the martian surface (e.g. Bishop et al., 2002). Studying the spectral effects of thin dust coatings is exceptionally difficult. Investigation of this phenomenon requires creating polished, near-flat

uniform Ca/Mg-sulfate substrates (difficult to do with such a soft and friable material), simulating airfall deposition of uniform grain size contaminant, and measuring coating thickness with microscopy, as performed with basaltic andesite substrates by Johnson and Grundy, 2001. The spectral effects of dust coatings on hydrated sulfates (and other Mars-relevant hydrated minerals) remains a valuable unexplored dataset.

Samples were mixed with plastic stirrers due to the lack of precision powder mixing equipment. Mixing was performed for over one minute, but the possibility of random preferential organization of grains when poured into the sample holders could not controlled. Calcium and magnesium sulfate powders are similar in appearance, rendering this potential error impossible to visually constrain.

For grain size series samples, clear trends are present. But, in laboratory resolution spectra of powdered samples (excluding the whole rock selenite sample), the largest band depths did not occur in the largest grain size fractions. A possible explanation is that spectra were contaminated as light interacted with the inner edges of the sample holders. Large grains crumbled when packed forcefully into the sample holder. To avoid destruction of large grains samples were loosely packed, resulting in voids the sample. It is possible that these voids allowed light to interact with the holder unobstructed and impact the spectra of these samples. Increased surface area of smaller grains may also explain this band depth discrepancy. Surface-to-volume ratio increases when samples are broken down into smaller grain sizes. This smaller ratio leads to an increase in reflectance and band depth shallowing, as seen in data for the grain size series samples. However, increased surface-to-volume ratio also creates more surfaces for adsorbed water to attach to. If the increase in band depth caused by additional adsorbed water exceeds the decrease in band depth resulting from increased surface-to-volume ratio, this may have caused smaller grain size bands to appear larger and explain the observed discrepancy.

2.5 Conclusions

Mastcam-Z will use a new filter set designed to be more sensitive to spectral features based on past experiences. The results of this work help to define Mastcam-Z's ability to constrain hydration signatures in Ca- and Mg-sulfates, the effects of various conditions on these hydration signatures, and what filter combinations are most effective to analyze potential hydrated Ca- and Mg-sulfates on Mars. The major findings presented here include:

1. Spectra reveal that the new ~975 nm filter constrains portions of the right bounds of the ~950-1000 nm hydration band in Ca/Mg-sulfates, offering resolution of band morphology not previously available. This additional band resolution allows for a new effective means to constrain hydration: the 937-975 band depth, which shows deeper bands than the 937-1013 band depth (the only means of constraining hydration with Mastcam) in *most* cases.

2. Bimodal mixing of hydrated sulfates affects depths of hydration bands in Ca/Mg-sulfates due to heterogeneous hydration states. The band depth shallowing that occurs is dependent on the hydration states of each component and their relative concentrations. For mixtures of Mg-sulfates, band shallowing does not pose significant risk of rendering bands undetectable to Mastcam-Z due to the prominent hydration bands of epsomite and hexahydrite, which possess high H_2O/SO_4 ratios. For Ca-sulfates, only gypsum-anhydrite mixtures composed of primarily gypsum retain some detectability.

3. Dust contamination of Mg/Ca-sulfates with small quantities of Mars JSC-1 significantly reduces reflectance in the green-blue wavelength region and shallows hydrations bands. In gypsum-anhydrite mixtures, 5% sample volume dust contamination obscures hydration bands to Mastcam-Z. In epsomite-kieserite mixtures, dust contamination significantly limits detectability, with detectable bands only being confined to epsomite-dominant mixtures.

4. Grain size effects in these samples corroborate the previous understanding of reflectance/absorption effects in long grains. Pure epsomite and gypsum samples generally exhibit deeper laboratory and Mastcam-Z band depths with increased grain size. Grain size is an important variable when investigating potential martian Ca/Mg-sulfates for signs of hydration.

5. Mixtures of hydrated Ca/Mg-sulfates cause nonlinear spectral combinations. These spectra cannot be effective explained by linear models and nonlinear spectral mixing models must be tested before we can effectively rely solely on models to understand spectral mixing on Mars. This work provides useful data to test nonlinear mixing models.

2.6 Future Work

Although this study provides an important dataset and intriguing filter combinations for identifying hydration signatures on Mars with Mastcam-Z, more work is needed. Numerous hydrated minerals exist on Mars that bear hydration bands in Mastcam-Z's effective wavelength range. To better understand how these minerals will appear to Mastcam-Z, similar work is needed addressing hydration band morphology in these minerals both at laboratory resolution and Mastcam-Z convolved resolution. Dust contamination also remains a significant issue and intermixed Mars dust simulant, as done in this study, represents only one piece of the problem. There still exists the prevalent case where a thin layer of dust overlays intriguing alteration minerals. Cases where this overlying dust may not be easily removed by rover equipment may occur and to optimize how Mastcam-Z handles these situations, worked is needed studying the spectral effects of thin uniform dust coatings.

3.0 DISTINGUISHING GEOLOGIC UNITS AND ALTERATION MINERALOGY AT MARS 2020 CANDIDATE LANDING SITES WITH VISIBLE-TO-NEAR-INFRARED SPECTROSCOPY: IMPLICATIONS FOR MASTCAM-Z

3.1 Introduction

3.1.1 Reflectance Spectroscopy from Orbit: CRISM

Our current understanding of martian surface mineralogy can largely be attributed to the high-resolution hyperspectral orbital spectrometers CRISM (Murchie et al., 2007, 2009) and OMEGA (Bibring et al., 2004, 2006). The work described here analyzes specific regions on Mars with CRISM imagery, warranting an in-depth explanation of CRISM's capabilities.

CRISM detects wavelengths 362-3920 nm using two detectors (VNIR detector from 362-1053nm and SWIR detector from 1002-3920) with a spectral resolution of 6.55nm/channel. CRISM has an aperture of 100 mm and focal length of 441 mm which allow for a 2.12° field of view and pixel angular size of 61.5 μrad (Murchie et al., 2007). The instrument is composed of three main parts: The Optical Sensor Unit (OSU), the Gimbal Motor Electronics (GME), and the Data Processing Unit (DPU). The OSU houses the spectrometers and optical equipment responsible for image capture. The GME enables function of the gimbal to scan surfaces at different angles, compensating for image distortion effects caused by spacecraft motion. Gimbal motion causes the bowtie-like dimensions of high-resolution CRISM images (as seen in Figures 26, 28, 29, 34, 41, 47, and 48); the field of view narrows as the camera becomes perpendicular to the surface and widens as the camera moves away from perpendicular. The DPU processes all optical data and allows the instrument to communicate with the MRO spacecraft. Summary products – mathematical parameters corresponding to key spectral features of certain minerals – are used to guide mineral identification with CRISM (Pelkey et al., 2007; Viviano-Beck et al., 2014), allowing users to quickly identify spectral endmembers in a scene. CRISM observations are often

paired with images taken by the MRO Context Imager (CTX), an orbital panchromatic stereo imager capable of 6 m/pixel resolution (Zurek and Smrekar, 2007) and the MRO High Resolution Imaging Science Experiment (HiRISE), an orbital color imager capable of 0.25m/pixel resolution (McEwen et al., 2007). Use of these instruments in tandem with CRISM produces maps illustrating relationships between geomorphology and mineralogy.

CRISM acquires spectral observations of Mars' surface in two modes: "multispectral mapping" and "targeted". The multispectral mapping mode provides near-global coverage at limited resolution (72 wavelength channels and 100-200 m/pixel spatial resolution) to document absorption features indicative of key endmember mineral phases (Murchie et al., 2007, 2009). This resolution discerns broad mineral classes but is unlikely to uniquely identify specific minerals. The gimbal is inactive in multispectral mapping mode and CRISM acquires spectra as MRO passes, longitudinally, across the planet – these observations are referred to as 'pushbroom' observations in reference to this motion. The targeted mode maps a small region with the complete hyperspectral resolution of the instrument and a spatial resolution of 15-19 m/pixel. The gimbal is employed to scan a single area without apparent motion distortion (Murchie et al., 2007, 2009). The broad global mineralogy constrained by multispectral mapping observations helps identify regions of interest for targeted hyperspectral observations.

3.1.2 Spectral Features of Martian Surface Mineralogy Detectable By CRISM

Diagnostic absorption bands (e.g., Figure 20) arising from the processes discussed in Section 1.2 are used to identify mineral classes and species on Mars. The absorption features discussed in this section are widely used to constrain martian surface mineralogy from orbit and necessary to the interpretation of this work's result.

SWIR observation reveals that Mars' igneous crustal rocks are composed of pyroxene, olivine (e.g., Breuer et al., 1993; Halliday et al., 2001; Nimmo and Tanaka, 2005) and feldspars that have been

identified by thermal IR spectroscopy (e.g., Christensen et al., 2000). Olivines exhibit broad absorption bands in the 1000 nm region (Figure 20b), varying from 105001080 nm with composition from Fo_{90} to Fo_{10} (e.g., King and Ridley, 1987; Clark et al., 1999). Pyroxenes exhibit broad absorption bands in the 1000 nm and 2000 nm regions (Figure 20b) that vary in exact band position with pyroxene composition (e.g., Cloutis and Gaffey, 1991).

Mineral-bound water and hydroxyl can be determined by diagnostic vibrational bands: a 1400 nm OH stretching overtone and a combination of OH stretching with H-O-H bending resulting in a 'doublet' band near 1900 nm (Figure 20a). Thus, the presence of a 1400 nm band alone indicates that only OH is present and the presence of a 1900 nm band indicates that water is also present. The strength of these bands is a function of the amount of H_2O and OH present (e.g., Clark et al., 1999).

Sulfate minerals exist in numerous Hesperian-aged deposits on Mars (e.g., Bibring et al., 2006; Ehlmann and Edwards, 2014). Fe(II)-sulfates exhibit bands in the 900-1200 nm range that appear similar to the broad 1000 nm bands of olivines and pyroxenes (e.g., Cloutis et al., 2006), however Fe(II) sulfates are also typically hydrated and show additional diagnostic bands. Most hydrated sulfates display bands in the 2100-2700 nm region (Figure 20a), particularly near 2550 nm and 2100 nm (e.g., Bishop and Murad, 2005; Cloutis et al., 2006). Jarosite and alunite show bands near 1850 nm, 2270 nm, and 2630 nm for jarosite and 1760 nm, 2170 nm, and 2530 nm for alunite (e.g., Bishop and Murad, 2005).

Phyllosilicates are prevalent in layered sedimentary stratigraphy on Mars (e.g., Grotzinger and Milliken, 2012), in some massive, nonlayered deposits (e.g., Poulet et al., 2005; Bibring et al., 2006; Bishop et al., 2008; Ehlmann and Edwards, 2014), and can be constrained by absorption bands in the 2200-2300 nm region (Figure 20a). Hydrated Fe/Mg smectites show absorptions near 2280-2300 nm, in addition to hydration bands at 1400 and 1900 nm (e.g., Frost et al., 2002). Illite and muscovite show bands at 1400 nm, 2200 nm, and 2350nm (e.g., Clark et al., 1990). Montmorillonite is common in

numerous deposits and exhibits prominent bands near 1900 nm and 2200 nm, with a minor 1400 nm band (e.g., Poulet et al., 2005). A doublet band near 2200 nm occurring with a 1400 nm band is indicative of kaolinite (e.g., Bishop et al., 2008) and Fe-bearing chlorites show a band near 2340 nm and minor bands at 2250 nm and 1900 nm (e.g., Bishop et al., 2002).

Carbonates are widespread in martian dust (Bandfield et al., 2003) and are commonly associated with olivine (e.g., Ehlmann et al., 2008b; Carter and Poulet, 2012; Niles et al., 2013; Goudge et al., 2015). Calcite and dolomite are known to exhibit numerous absorption features in the 1600 – 2550 nm region (Figure 20a) and broad doublet bands near 1200 nm (e.g., Gaffey, 1985). Carbonates also display diagnostic bands near 2300 and 2500 nm that vary with cation composition (e.g., King et al., 2014) – band position shifts longward from Mg- → Fe- → Ca-carbonate (e.g., King et al., 2014).

3.1.4 Mars 2020 Candidate Landing Sites

Investigating ancient environments with orbital spectroscopy is an important aspect of Mars rover landing site selection and mineral identification aids our understanding of past chemical and aqueous conditions. The MSL landing site selection process involved five community workshops during which sites were proposed, ranked, and incrementally eliminated (e.g., Grant et al., 2011). Mineralogy assessed from orbit played a key role in understanding candidate sites' geologic diversity, potential habitability, and potential for biosignature preservation (e.g., Grant et al., 2011).

The selection of landing sites for the 2020 mission will proceed in a similar fashion. As of now, three sites are being evaluated to serve as Mars-2020's field area (Figure 22): the Columbia Hills of Gusev Crater, NE Syrtis Major, and Jezero Crater. CRISM hyperspectral images, particularly SWIR observations, have played a key role in mineralogical characterization of these sites.

Jezero Crater, a 49 km diameter impact crater in the located within the NE Syrtis region (Figure 22), is an ancient crater lake environment featuring two Noachian-aged inlet channels and an outlet

channel extending from a breached section of the northeast crater rim (e.g., Fassett and Head, 2005; Schon et al., 2012; Goudge et al., 2017). The Jezero crater watershed contains over ~640 km of drainage channels within a ~15,000 km^2 catchment area (Schon et al., 2012) that drove lake depths to exceed ~450 m before crater breach occurred (Fassett and Head, 2005). Two depositional fans are preserved in the crater (Fassett and Head, 2005; Goudge et al., 2017) – one at the mouth of each inlet channel. The western fan is more clearly defined than the heavily eroded northern fan. CRISM SWIR observations have detected Fe/Mg-smectites on both deltaic units, olivine variably altered to Mg-carbonate on the northern delta and in terrain west of the western delta, and pyroxenes throughout the region (e.g., Goudge et al., 2015; Salvatore et al., 2017) Alteration minerals in these deposits are interpreted to be detrital, having been eroded and delivered from the NE Syrtis region via the large Jezero crater watershed (e.g., Ehlmann et al., 2008b, 2008a, 2009). Covering most of the crater floor and embaying deltaic landforms, a spectrally-bland volcanic unit caps the crater's regional stratigraphy. Jezero Crater offers a large, potentially Noachian-aged, open-basin lake environment featuring two large deltaic fans that transported Syrtis Major phyllosilicates and olivine/Mg-carbonate assemblages as a potential Mars 2020 landing site.

Syrtis Major Planum (Figure 23) is a low-albedo region of Mars west of the 1900 km Noachian-aged Isidis basin (e.g., Nimmo and Tanaka, 2005). Syrtis Major is interpreted to be a volcanic province related to the Isidis-forming impact event (e.g., Hiesinger and Head, 2004). As identified by CRISM SWIR observations, NE Syrtis Major is characterized by two main regional units: an overlying olivine unit and an underlying low-Ca pyroxene unit (e.g., Ehlmann and Mustard, 2012; Bramble et al., 2017). Clay-rich deposits (predominantly Fe/Mg-smectites, with some Al-phyllosilicates) are interbedded with the low-Ca pyroxene material in some exposures. The olivine unit exhibits variable alteration to Mg-carbonate and serpentine. Exposed stratigraphy at NE Syrtis spans a large portion of Mars history (e.g., Mustard et al., 2010; Ehlmann and Mustard, 2012; Bramble et al., 2017): an early-Hesperian lava capping unit

underlain by layered sulfate material comprised of jarosite and polyhydrated sulfates, then the olivine/Mg-carbonate unit, and finally, the early Noachian basement composed of low-Ca pyroxene and clays. This impressive stratigraphy spanning the Noachian-Hesperian transition offers temporal interpretation of deposition and a diverse alteration mineralogy – potentially due to extensive surface interaction of volcanic material with hydrothermally-heated sulfur-rich waters (e.g., Ehlmann and Mustard, 2012; Bramble et al., 2017) – for Mars-2020 to explore.

The Columbia Hills landing site is located within Gusev crater and is the landing site of MER Spirit (2004-2011) (Figure 24). Gusev is a 166 km Noachian-aged impact crater in the Aeolis quadrangle (Squyres et al., 2004a, 2004b, 2006; Arvidson et al., 2006). The 700km outflow channel Ma'adim Vallis – one of the largest outflow channels on the planet – extends from the southern rim of the crater (e.g., Cabrol et al., 1998; Irwin et al., 2002). Much of the basin floor is Hesperian-aged volcanic plains of olivine and pyroxene (e.g., Golombek et al., 2006; McSween et al., 2006) and the Columbia Hills are likely remnants of the central peak of the impact basin that have undergone extensive erosion (e.g., McCoy et al., 2008; van Kan Parker et al., 2010). The dark volcanic plains surrounding the Columbia Hills are subject to recurrent dust devil activity that leaves "trails" (curvilinear, low-albedo features where dust has been removed) patterning the landscape (Greeley et al., 2006).

Most knowledge of the Columbia Hills mineralogy comes from the discoveries of the Spirit rover. While CRISM SWIR has been a valuable tool for constraining mineralogy at other regions, much of the Columbia Hills is partially to completely obscured by a millimeters thick coating of dust (e.g., Arvidson et al., 2006) that has hindered mineral detections from orbit. Signatures of Mg-carbonate and Al/Fe/Mg-phyllosilicates have been identified in CRISM SWIR (Carter and Poulet, 2012), but are limited spatially. During Spirit's mission, "fresh" (nearly dust-free) soils were uncovered by dragging of Spirit's inoperative right, front wheel (e.g., Arvidson et al., 2006) and analyses revealed Mg/Fe/Ca-carbonates, phyllosilicates, hydrated silica, hydrated sulfates, ferric sulfates, Ca/Fe(III)-phosphates, nanophase ferric-

oxides, hematite, halite, and allophane (Ming et al., 2006; Clark et al., 2007; Lane et al., 2008; Wang et al., 2008; Rice et al., 2010).

The Columbia Hills also harbors "Home Plate", a plateau composed of partially-altered basaltic pyroclastic material that was the subject of substantial investigation by Spirit (e.g., Squyres et al., 2007; Arvidson et al., 2008; Schmidt et al., 2008). The geomorphology and mineralogy of the Columbia Hills are consistent with alteration of mafic crust or volcanoclastic material by near-neutral hot springs, acid-sulfate fumaroles, or groundwater brines (e.g., Schmidt et al., 2008; Yen et al., 2008). Opaline silica deposits at Home Plate are morphologically and spectrally similar to biologically-mediated silica material in the hydrothermal region of El Tatio, Chile (Ruff and Farmer, 2016); these compelling similarities have spurred questions about the past habitability and biosignature preservation potential of the ancient hydrothermal system within the Columbia Hills.

3.1.3 CRISM Imaging Spectroscopy Analysis

To aid in landing site selection and the future Mastcam-Z investigation, this work examines CRISM SWIR and VNIR spectral observations of each site. Apart from the Columbia Hills (investigated by Spirit's Pancam), the mineralogy of these sites has been characterized from orbit by CRISM SWIR exclusively (e.g. Ehlmann and Mustard, 2012; Goudge et al., 2015). There has been no orbital VNIR study of any landing site. This work aims to develop spectral parameters that can distinguish key geologic/mineralogic units in CRISM imagery that have been convolved to simulated Mastcam-Z bandpasses for each landing site. CRISM SWIR is used to determine the mineralogy at each site and Mastcam-Z convolved CRISM VNIR is then explored to develop spectral parameters that the future Mars-2020 rover can best use to distinguish these units. Two key hypotheses are addressed:

1) Mastcam-Z VNIR parameters can be developed from convolved CRISM observations that distinguish the prominent geologic/mineralogic units at each landing site.

2) VNIR spectra from orbit show sensitivity to prominent geologic features, but the primary control on VNIR spectral variability from orbit is the distribution of iron-oxide-rich dust.

3.2 Methods

Representative CRISM observations were acquired for each candidate site from the NASA Planetary Data Server (Table 7 and Figure 25). CRISM observations were selected to fit three specific criteria: they were used in previously published work, they included the main units/deposits supporting candidacy of the site, and they included material that is either within proposed site landing ellipses or part of a postulated "drive-to" region (regions outside of the ellipse that are compelling enough to warrant extended travel after the rover has landed). Two CRISM observations were used for the Columbia Hills due to significant the seasonal variations in dust activity in the region revealed by Spirit (Lemmon et al., 2015). Lemmon et al. (2015) corroborates broader work determining that martian dust lifting varies with solar longitude (L_s) – the Mars-Sun angle measured from the northern hemisphere used to describe martian seasons (Murphy, 1999). The use of two Columbia Hills observations serves to document spectral changes that may occur between seasons due to fluctuating dust conditions. For NE Syrtis, three observations were selected. Although the regional geology is well documented, the geology of the landing ellipse has yet to be fully characterized. Two observations were selected covering the landing ellipse to test spectral parameters developed at the observation south of the ellipse in regions where mineralogic and geologic units have been extensively studied in the literature.

Corresponding CRISM SWIR and VNIR observations for each Observation ID were prepared for analysis using the CRISM Analysis Toolkit (CAT) plugin for ENVI (Environment for Visualizing Images). CAT is a suite of ENVI and IDL tools designed by the CRISM science team and Brown University to automate the standard methods used to prepare CRISM data for more sophisticated spectral analysis. In CAT, first, a photometric correction was applied to correct the sunlight incidence angle in the scene ($Spectrum_{Original}/cos\Theta$). A 'volcano-scan' correction was then applied to remove spectral contributions

from the martian atmosphere by dividing the spectral data in the scene by spectra acquired over a region above which there is no atmosphere: the summit of Olympus Mons. The Pelkley 2-Wavelength Volcano Scan, the most recently developed volcano scan method, was used (McGuire et al., 2009). Columnar bias in spectral data was smoothed out using the 'Remove Stripes' tool. CRISM SWIR summary parameters are notoriously noisy, bearing horizontal or vertical 'striping' that skews histograms. While the CRISM Analysis Toolkit contains a variety of tools for mitigating this striping and MTRDR (Map-Projected Targeted Reduced Data Records) observations released by the CRISM team undergo a sophisticated data cleaning procedure, not all spectral striping can be removed. Spectral striping is evident in all CRISM SWIR summary parameters present in this study despite MTRDR observations being used. These effects are primarily constrained to summary parameters and do not significantly affect the interpretations of this work. Lastly, a map projection was applied using the corresponding Derived Data Records (DDR) for each scene. DDR files contain observational conditions/locations allowing for quick map projection to the GCS_Mars_2000 coordinate system. Processed imagery was exported as 3-dimensional floating-point arrays for further manipulation in IDL. The latest CRISM summary products (Viviano-Beck et al., 2014) were calculated for each observation (Table 8) and exported as 3-dimensional arrays.

CRISM VNIR observations were convolved to Mastcam-Z bandpass resolution following the methodology of Bell et al., 2006. Transmission profiles for Mastcam-Z filters are not yet characterized; Mastcam bandpasses were used for this convolution, with the 805 nm filter being duplicated and shifted to 975 and 600 nm to simulate the new Mastcam-Z filter positions (Figure 3). These bandpasses were used to interpolate reflectance values at each band and the remainder of the CRISM VNIR data was discarded, resulting in 3-dimensional arrays with data only at wavelengths for the theoretical Mastcam-Z filters.

MERSpect, an IDL-based operations package developed by the MER Pancam team for the manipulation of multispectral image data, and currently maintained by the MSL Mastcam team, was used to analyze the CRISM observations. CRISM SWIR summary products were used to determine spectral endmembers. CRISM SWIR parameters exist for many materials – some not relevant to this study, such as H_2O and CO_2 ices. Because no surface ice is observed at these sites, these, and other irrelevant, summary parameters were rejected as geologically implausible. After reasonable spectral endmembers were determined, individual reflectance spectra were acquired from representative endmember regions in MERSpect by extracting a single spectrum average of all pixels within a polygonal selection.

In CRISM data analysis, spectra of interest are often divided by a 'denominator' spectrum (Figure 26) that represents a bulk composition the user wishes to remove from the spectra of a region of interest (Murchie et al., 2009). Due to the similarity of martian terrains, spectra that are not processed via this 'ratio method' can look largely similar and diagnostic absorption bands may not be visible. Dividing a spectrum of interest by some denominator spectrum to tease out minute spectral differences is a staple technique in CRISM data analysis, but this method is not without potential for error. Dividing spectra from two regions containing starkly diverse alteration mineralogies could produce spectra showing differences that could be misinterpreted for mineral identification. Dividing two spectra that are too spectrally similar could produce data with no distinct bands at all. During this study, I was careful to select denominator spectra that represented a composition likely to be found throughout the entire study region, but not of importance for constraining and mapping alteration mineralogy. For the Columbia Hills, denominator spectra came from the broad volcanic plains in regions largely free of dust devil tracks and small impact craters. In Jezero Crater denominator spectra came from the crater floor. And in NE Syrtis denominator spectra came from the abundant dark dune fields throughout the region.

Extracted spectra were characterized to determine the wavelength position of major absorption bands and compared to terrestrial and martian analog mineral spectra from the WWU Spectral Database and 'Minerals Identified through CRISM Analysis' (MICA) spectral libraries, respectively. The MICA spectral library contains confirmed CRISM spectra for a variety of minerals on the martian surface (Viviano-Beck et al., 2014). Mineral detections were also compared to results of previous work to corroborate findings. CRISM SWIR data is prone to significant noise (causes of which will be discussed in section 3.4.4) and common practice is to remove data (Figure 26) from exceptionally noisy regions (often 1000-1200 nm and 1600-1700 nm in this work) in otherwise telling CRISM spectra (e.g., Ehlmann and Mustard 2012; Goudge et al., 2015). The 1600 nm region is often noisy due to an instrument filter boundary at ~1650 nm (Murche et al., 2009). All CRISM SWIR spectra presented in this work exclude anomalous spectral spikes.

In Mastcam-Z convolved data, band depths and band ratios were used to identify spectral parameters that highlighted key mineralogic and geologic units at each site. Because rock composition, dust contamination, and light conditions vary between regions, spectral parameters were found for each scene independently. A trial and error process was employed to identify spectral parameters showing correlation to geomorphic units of interest. In many regions, spectral parameters were found that did not correlate to the geomorphology of a region and were discarded. To consider a spectral parameter useful, the parameter needed to correspond to rock units that could reasonably be identified by a traversing rover. Spectral variability between the Mastcam-Z VNIR filters is somewhat limited and several 'endmember' parameter groups consisting of different filter combinations highlighted similar geologic units. However, parameter groups varied significantly in how completely the prominent geologic units were highlighted. The parameters shown in this work highlighted the most terrain of their corresponding geologic units.

Standard RGB composites were made using the RGB Bayer filter bands at 640 nm, 554 nm, and 495 nm to simulate real-color imagery. However, overlapping band coverage in multi/hyperspectral imagers can render minute color intensity differences between bands difficult to discern. To accentuate minute color differences, decorrelation stretches (e.g., Gillespie et al., 1986) were created for each scene to document overall color variability in the left and right eyes of Mastcam-Z, respectively. Decorrelation stretches remove interband coloration correlation and enhance color differences by calculating the correlation matrix of selected bands (also referred to as the 'rotation matrix'), calculating 'stretching vectors' from the reciprocal of the square-root of correlation matrix eigenvalues, and multiplying these stretching vectors by the rotation matrix (Alley, 1999). These significantly exaggerated RGB color images can then be used to determine where minute spectral differences occur in regions that are seemingly nonunique in standard VNIR imagery. Three bands are required for each stretch and were chosen to span the wavelength coverage of each eye. The 805 nm stereo band shared by both eyes was only applied to the decorrelation stretch for the right eye. The right-eye decorrelation stretch was generated using the 805 nm, 908 nm, and 1013 nm filters. The left-eye decorrelation stretch was generated using the 445 nm, 600 nm, and 751nm bands.

Mastcam-Z spectral parameters were exported from MERSpect as .TIFF rasters and imported into ArcGIS. These rasters were geoferenced and mapped onto CTX basemaps to visualize relationships between spectral parameters and geomorphology, creating Mastcam-Z parameter 'unit maps.' High-resolution digital elevation models made from HiRISE stereo images (e.g., Kirk et al., 2008) and were used to create 3D perspective models that RGB composites and Mastcam-Z parameter unit maps could be mapped on to create simulated Mastcam-Z reconnaissance imagery.

3.3 Mars-2020 Candidate Landing Sites: Results and Discussion

Mastcam-Z parameters, CRISM SWIR parameter mapping, and spectral analysis were done for each landing site independently. Large differences in spectral sensitivity and mineral distribution between landing sites warranted the development of parameters for each site individually. Given this approach, this section presents and discusses results for each landing site separately before a discussion of broader implications relevant to the results of all sites follows in Section 3.4. Maps of CRISM and Mastcam-Z parameters (Table 9) and the properties of associated reflectance spectra are discussed in this section. We do not consider these suggested Mastcam-Z parameters to correspond to a specific mineralogy, but they do correspond to rocks bearing key minerals in some cases and do distinguish important geologic units.

3.3.1 Jezero Crater Results

Seven regions of interest were investigated and chosen for spectra extraction in Jezero Crater (Figure 27): (1) Low-albedo material at the front of the western delta, (2) channelized, high-albedo terrain on the southwestern portion of the western delta, (3) a curved, elongate unit determined by Goudge et al. (2015) to be exposed remnants of the crater floor, (4) portions of the northern delta, (5) mottled terrain north of the crater rim, (6) hilly terrain north of the western delta, and (7) high-albedo hill units within the proposed landing ellipse.

The parameters BD_{554} (554 nm band depth), R_{600}/R_{805} (ratio of reflectance at 600 nm and 805 nm), and R_{805}/R_{908} (ratio of reflectance at 805 nm and 908 nm) were found to best correspond to the regions of interest. As revealed by Mastcam-Z parameter maps (Figure 28a,c,e; 29d), most of the western delta (excluding craters and the low-albedo delta front; region 2), the hilly and mottled terrain to the north (regions 5 and 6), portions of the northern delta and surrounding terrain (region 4), the landing ellipse hills (region 7), and hills to the southwest are distinguished by BD_{554}. R_{600}/R_{805}corresponds

to the exposed crater floor unit and surrounding terrain, the western delta front, portions of the northern delta, and the crater rim (Figure 28a,c,e; 29d). R_{805}/R_{908} highlights similar terrain as R_{600}/R_{805}, but also highlights terrain encircling the landing ellipse hills, in portions of the hilly terrain north of the western delta, numerous small impact craters, and at the contact between the western fan and the surrounding basin floor (Figure 28a,c,e; 29d). RGB color and decorrelation stretches (Figure 29a,b,c) corroborate trends observed in Mastcam-Z parameter maps showing sedimentary units and the basin floor/dark regions of the western fan as distinct endmembers.

CRISM SWIR summary parameters BD1900_2 (CRISM SWIR parameter sensitive to mineral-bound H_2O), D2300 (CRISM SWIR parameter sensitive to Fe/Mg-smectites), and MIN2295_2480 (CRISM SWIR parameter sensitive to Mg-carbonates) were mapped (Figure 28b,d,f) to determine the distribution of alteration minerals and compare the result to minerals previously found in Jezero Crater. Spectral signatures consistent with Mg-carbonate exist in the hilly terrain north of the western delta and extend south along the western edge of the CRISM observation. Mg-carbonate signatures are present in the northern fan and mottled terrain, as well (Figure 28d; 29e). Regions mapped orange/yellow indicate the presence of signatures consistent with both hydration (BD1900_2) and Fe/Mg-bearing phyllosilicates (D2300). These signatures can be found on the northern and southern ends of the western delta, the mottled terrain, northern delta, and landing ellipse hills (Figure 28b,d,f; Figure 29e). Limited hydration signatures are also present in the exposed crater floor unit and hills southward (Figure 29e). Mafic parameter mapping (Figure 29f) reveals abundant olivine and pyroxenes. Indicated by greenish-yellow to orange color, high- and low-calcium pyroxenes are concentrated in basin floor material embaying the front of the western delta and the southern reaches of the northern delta, in the crater rim, in hills to the southwest, within small impact craters to the northwest, and embaying the exposed crater floor unit (Figure 29f). Low-Ca pyroxene also dominates much of the channelized regions of the western delta (Figure 29f). Olivine detections are abundant in the northern delta, portions of the western delta, the

hilly terrain north of the western delta, portions of the exposed crater floor unit, and in hills to the south (Figure 29f).

In CRISM SWIR spectra (Figure 30), the low-albedo material at the western fan exhibits a spectrum with three notable absorption bands centered near 1370 nm, 1970 nm, and 2300 nm. The spectrum for the channelized material on the western delta also shows three notable absorption features: a doublet band 1915/2000 nm, a band at 2300 nm, and a small band at 2530 nm. The exposed crater floor spectrum shows a triplet band centered at 1930/1994/2060 nm, a shallow, broad band spanning 2170-2350 nm, a small band at 2555 nm, and a steep, positive slope spanning 1250-1800 nm. Mottled terrain, hilly terrain, and northern fan spectra bear several key features: a prominent increase in reflectance from 1250-1600 nm, a doublet band at 1940/1995 nm (1920/1995 nm for the northern delta), and two bands at 2310 nm and 2500 nm. The hill units within the landing ellipse display a small band at 1450 nm and prominent absorptions near 1950 nm and 2330 nm. Apart from the exposed crater floor unit and low-albedo western delta front, VNIR spectra (Figure 31) slope positively toward longer wavelengths. The western delta front spectrum exhibits a broad absorption longward of 530 nm. The northern delta, high-albedo hills, hilly terrain, mottled terrain, and channelized western delta region show absorption bands in MCZ VNIR spanning 445-676 nm, centered between 527 nm and 554 nm.

3.3.2 Jezero Crater Discussion

Parameter mapping of CRISM SWIR summary products at Jezero Crater revealed widespread alteration minerals and hydrated material throughout the region, consistent with previous studies (e.g., Goudge et al., 2014; Salvatore et al., 2017). Mg-carbonate signatures are abundant northwest of the western delta and occur in some regions of the northern delta (region 4), the mottled terrain north of the crater rim (region 5), and regions along the western edge of the observation. Fe/Mg-bearing phyllosilicate signatures dominate the western fan (regions 1 and 2) and the hill units (region 7) within

the landing ellipse. Hydration is detected throughout these regions. This mapping suggests that Jezero Crater is rich in alteration minerals that are clearly discernable from orbit and should presumably present little challenge to ground-based instruments able to investigate finer-scale occurrences.

Spectra from the western delta, the channelized high-albedo region (region 2) and low-albedo material at the delta front (region 1), exhibit notable absorption bands. The 1915 nm, 2300 nm, and 2530 nm bands in the channelized region spectrum correspond to the diagnostic band locations of MICA Mg-Carbonate and roughly align with RELAB magnesite. The wide 1400 nm O-H stretching overtone (Hunt, 1977; Clark et al., 1999) and 1900 nm hydration bands in both the channelized and low-albedo regions also correspond to wide bands in this region for USGS Saponite. USGS Saponite is used only as a proxy for Fe/Mg-smectites, which exhibit band position differences that can be >10 nm. This work does not claim any species to be saponite and merely provides a useful comparison spectrum helping distinguish Fe/Mg-bearing smectites from other broad classes. The low-albedo region shows a 2315 nm band consistent with USGS Saponite and characteristic of Fe/Mg-bearing smectites which bear diagnostic bands from 2280-2320 nm (e.g., Clark et al., 1990). Channelized western delta terrain contains potential Mg-carbonate and Fe/Mg smectite while the low-albedo material on the delta front may contain Fe/Mg smectites.

The exposed crater floor unit (region 3) represents and altered olivine-rich unit. Spectra from this unit show a steep increase in reflectance from 1250-1600 nm, possibly resulting from Fe^{2+} electronic transitions that produce a broad absorption centered near 1000 nm in olivines (e.g., King and Ridley, 1987; Kong et al., 2011). A triplet hydration band at 1900-2000 nm, a shallow, broad band spanning 2170-2350 nm, and a wide band at 2550 nm indicate some alteration phases are present. Concise discrimination of alteration species is not possible given the wide nature of these bands, but the presence of hydration and bands at wavelengths longward of 1600 nm in an olivine-like spectrum indicates some degree of alteration in an olivine-rich unit.

Rocks to the north are dominated by Mg-carbonate. Spectra from the northern delta (region 4), the mottled terrain (region 5), and the hilly terrain (region 6) exhibit a clear 1920-1940/1995 nm doublet hydration band and C-O stretching pairs near 2310 and 2500 nm. All three spectra show significant reflectance increases from 1250-1600 nm, possibly related to the broad Fe^{2+} 1000 nm band found in olivine. I interpret these units to represent olivine and Mg-carbonate alteration assemblages.

Within the landing ellipse, the high-albedo hills (region 7) show a minor O-H stretching overtone at 1450 nm, a broad hydration band centered at 1950 nm, and an Fe/Mg smectite absorption near 2320 nm. Band positions correspond with the USGS saponite comparison spectrum and, along with CRISM SWIR parameter maps, suggests Fe/Mg phyllosilicates dominate the mineralogy of this unit.

It is important to note that Mars conditions also can reduce the amplitude of certain diagnostic SWIR bands. OH/H_2O bands can appear significantly shallow or entirely absent in CRISM spectra, hindering accurate mineralogical detections and prompting researchers to often abandon use of the 1400 nm spectral band as a diagnostic tool. In Mars-like ambient conditions dehydrated OH/H_2O-bearing minerals lose diagnostic 1400/1900 nm hydration bands and upon rehydration these spectral signatures either remain lost or return significantly weaker (Morris et al., 2010, 2011). Clay mineral dehydration in Mars-like conditions collapses phyllosilicate interlayers, inhibiting rehydration and potentially stunting the reappearance of diagnostic hydration bands (Morris et al., 2010). Near-1400 nm OH bands are weak and/or non-existent in the spectra of phyllosilicate-bearing regions in Jezero Crater, showing the occurrence of this problem.

VNIR spectra show fewer spectral features than SWIR spectra. At Jezero Crater, most VNIR spectra are more reflective in red wavelengths than blue-green, apart from the low-albedo material at the western delta front. The low-albedo western delta material exhibits a broad absorption longward of 530 nm that may be the result of olivine Fe^{2+} transitions. The mottled and hilly terrain north of the

western delta, northern delta, channelized western delta terrain, and high-albedo hills in the landing ellipse show absorption features centered between 527 nm and 554 nm. Fe^{3+} transitions can give rise to a band near 530 nm (e.g., Kong et al., 2011). Jezero Crater rocks are iron-bearing with Fe^{3+} in regions associated with alteration minerals and possible Fe^{2+} associated with the darker regions of the western delta, potentially indicating an olivine component.

Mastcam-Z parameters at Jezero Crater distinguish sedimentary rock rich in H_2O, Mg-carbonate and/or Fe/Mg-smectites from regions darker in color and potentially more mafic. BD_{554} highlights regions of the western delta, hills within the landing ellipse, and altered rocks to the north that exhibit signatures of hydration, Fe/Mg-smectites, and Mg-carbonate. R_{600}/R_{805} highlights regions showing spectral signatures related to olivine in CRISM SWIR parameter maps. R_{805}/R_{908} highlights olivine-bearing regions and shows some sensitivity to Mg-carbonate bearing terrain northwest of the western delta and in the northern delta.

These parameters show significant spectral variability among geologic units in 3D-simulated reconnaissance images (Figure 32). BD_{554} is shown distinguishing altered rock to the north in angle #3 and the landing ellipse hills in angle #2. Angle #4 shows the western delta front highlighted by both R_{600}/R_{805} and R_{805}/R_{908}. Angle #1 shows BD_{554} sensitivity to altered rock in the north and R_{805}/R_{908} sensitivity to the Mg-carbonate unit northwest of the western delta.

3.3.3 NE Syrtis Results

Five regions of interest were investigated in the NE Syrtis HRLB8C2 scene: (1) a high-albedo star-shaped unit, (2) nodular units observed in the cliff face, (3) a triangular shaped plateau with small ridges on its top, (4) high-albedo rugged terrain, and (5) an elongate unit composed of ridge-forming rocks, and (Figure 33).

CRISM SWIR parameter mapping indicate several areas that contain spectral signatures consistent with hydrated sulfates (Figure 34b,d; 35e). These areas include the star-shaped unit (region 2), nodular units within the cliff face (region 1), and portions of the high-albedo rugged unit to the north (region 4). Signatures consistent with Fe/Mg-bearing phyllosilicates and Mg-carbonates often occur together (Figure 34b,d,f; 35e) and are correlated to olivine-bearing units in the mafic mineralogy map (Figure 35f), notably on the central plateau-forming units (region 3) and the ridge-forming terrain to the east and southeast. Mafic summary parameters reveal olivine largely in the plateau-forming units (including the triangular plateau; region 3) in the center of the observation, the ridge-forming terrain to the east and southeast (including the elongate ridged unit; region 5), and terrain to the north of the star-shaped unit (Figure 35f). High-Ca pyroxene-bearing material embays olivine-bearing units in numerous locations (Figure 35f). Low-Ca pyroxene is noted on the large southwest cliff-forming unit and in rugged terrain to the north (Figure 35f). Mastcam-Z parameters (Figure 34a,c,e; Figure 35d) correlate with specific geologic units highlighted by CRISM SWIR summary parameters (Figure 34b,d,f; 35e). The parameters R_{975}/R_{908} (ratio of reflectance at 975 nm and 908 nm), R_{805}/R_{975} (ratio of reflectance at 805 nm and 975 nm), and R_{751}/R_{445} (ratio of reflectance at 751 nm and 445 nm) were found to best correspond to the regions of interest. R_{975}/R_{908} corresponds well to regions highlighted by SINDEX2 (CRISM parameter sensitive to sulfate minerals): the star-shaped unit (region 2), nodular units (region 1), high-albedo cliff-forming units to the northwest, and portions (region 4) of the northern rugged unit (Figure 34a/c and Figure 35d). R_{805}/R_{975} shows correlation to terrain highlighted by OLINDEX3 (CRISM parameter sensitive to olivine) including the central plateaus units (region 3), terrain to the northwest, and some ridge-forming units to the east (region 5) and southeast (Figure 34a,c,e; 35d). R_{751}/R_{445} corresponds to the oval-shaped unit to the east of the star-shaped unit, the elongate ridged feature (region 5), and various ridged regions to the north (Figure 35a,c,e; 35d).

CRISM SWIR spectra (Figure 36) of these units show several distinct absorption bands. The nodular unit spectrum shows a small absorption band near 1460 nm, a doublet band at 1950/1995 nm, an abrupt flattening from ~2000-2300 nm, and a subsequent downslope. The star-shaped feature shows a band at 1940 nm and a wide band from 2140-2350 nm; reflectance within this band decreases toward 2350 nm. Three distinct bands at 1915nm, 2290 nm, and 2500 nm exist within the triangular plateau spectrum. The rugged high-albedo feature bears notable absorptions at 1415 nm, 1675 nm, a doublet at 1930/1995 nm, 2210 nm, and 2395 nm, with an abrupt drop off in reflectance occurring thereafter. The elongate ridged unit shows three bands at 1950 nm, 2300 nm, a wide band spanning 2400-2560 nm, centered near 2510 nm, and a potential absorption near 2100 nm, although this feature is exceptionally shallow. CRISM VNIR/MCZ spectra (Figure 37) exhibit fewer spectral features than SWIR, but these features are notable. The rugged high-albedo terrain spectrum is roughly flat; however, an absorption band centered near 875 nm is noted. The nodular and star-shaped units exhibit VNIR spectra sloping positively toward longer wavelengths with broad absorptions centered near 875 nm. Spectra for the triangular plateau and northern rugged unit slope positively from 450-875 nm and 450-750 nm, respectively, before a drop-off in reflectance toward longer wavelengths.

3.3.4 NE Syrtis Discussion

Numerous diagnostic features are observed in NE Syrtis SWIR spectra (Figure 36) that are consistent with mineralogy previously described in the region (e.g. Ehlmann and Mustard 2012). The high-albedo star shaped feature (region 2) shows absorption bands in CRISM SWIR correlating to bands observed in a USGS jarosite laboratory spectrum (Figure 36): a 1940 nm hydration band and a wide band spanning 2140-2350 nm within which reflectance decreases toward 2350 nm. This wide band is the likely remnants of a doublet feature within this region associated with Fe-O-H vibration (e.g., Crowley et al., 2003). Showing a hydration doublet at 1950/1995 nm, an O-H stretching band near 1460 nm, and a roughly flat spectrum from ~2000-23000 nm, the nodular cliff face unit (region 1) exhibits a spectrum

resembling the MICA polyhydrated sulfate example. These two units associate with the SINDEX2 CRISM SWIR parameter for sulfate signatures and likely represent jarosite-bearing and polyhydrated sulfate-bearing rock. These sulfate deposits do not exhibit 1400 nm hydration bands that are present in analog spectra.

The ridged triangular plateau (region 3) shows a hydration band at 1915 nm and a C-O stretching pair at 2290/2500 nm and resembles the MICA Mg-carbonate and RELAB Mg-carbonate spectra (Figure 36). CRISM SWIR parameter mapping shows OLINDEX3 correlation in this plateau, corroborated by a significant reflectance increase from 1250-1600 nm associated with Fe^{2+} electronic processes. This unit likely consists of olivine occurring with Mg-carbonate.

The elongate ridged unit (region 5) shows a hydration band near 1950 nm and bands centered near 2300 nm and 2510 nm, likely the result of C-O stretching (Figure 36). A shallow, potential dip in absorption occurs at around 2100 nm. Weak bands in the 2100 nm region are diagnostic of serpentine, which also bears bands near 2320 nm and 2510 caused by Mg-OH/metal-OH overtones (e.g., Viviano-Beck et al., 2014). The presence of this potential, albeit exceptionally shallow 2100 nm feature raises the possibility of serpentine occurring within this unit, as suggested by Ehlmann and Mustard (2012). Spectrum reflectance also increases sharply from 1250-1600 nm, indicating an olivine component. This unit likely consists of olivine and Mg-carbonate with potential associated serpentine. The ~1400 nm OH band is not present, potentially the result of phyllosilicate interlayer collapse (Morris et al., 2010).

The high-albedo rugged terrain (region 4) shows absorptions at 1415 nm due to O-H stretching, 1930/1995 nm due to H_2O, 2210 nm, and 2395 nm. The positions of these bands correspond with bands observed in USGS Kaolinite and would corroborate the Al-phyllosilicate identification in this region by Ehlmann and Mustard, 2012. Al-rich clays can be identified by a doublet near 2200 nm resulting from Al-OH vibrations and other potential bands near 2260 nm, 2350 nm, and 2440 nm resulting from Al-OH

stretch and bend combinations (e.g., Clark et al., 1990). This unit likely represents Al-phyllosilicate bearing rock.

VNIR spectra also show some bands revealing compositional clues (Figure 37). Both sulfate-bearing units and the kaolinite-bearing rugged terrain show spectra with broad bands centered near 875 nm, indicating Fe^{3+} transition. All spectra, apart from the rugged terrain is red-dominant. The ridged triangular plateau, elongate ridge, and star-shaped feature show wide absorptions in the 400-600 nm range – potentially the 530 nm Fe^{3+} transition. NE Syrtis rocks bear signatures of Fe^{3+} in all examined regions.

Mastcam-Z parameters at NE Syrtis are sentitive to sulfate-, Mg-carbonate-, olivine-, and high-Ca pyroxene-bearing units identified by SWIR mapping and representative spectra. R_{975}/R_{908} is sensitive to terrain distinguished by sulfates parameter SINDEX2 in CRISM SWIR parameter maps, including the nodular features, the star-shaped unit, and parts of the rugged unit in the north (although the spectrum of this unit is consistent with Al-bearing phyllosilicates). R_{805}/R_{975} selects regions corresponding to olivine, high-Ca pyroxene, and Mg-carbonate in SWIR parameter maps. R_{751}/R_{445} distinguishes the elongate ridged feature showing a potential 2100 nm absorption band that was mapped by Ehlmann and Mustard (2012) as serpentine-bearing. Because digital elevation models are not available for the region covering CRISM observation HRLB8C2, simulated Mastcam-Z reconnaissance images are not producible for this region at the time of this writing.

Mastcam-Z parameters for NE Syrtis were developed using the HRLB8C2 CRISM observation because HRLB8CS has been extensively investigated by other researchers (e.g. Ehlmann and Mustard, 2012). Their work enabled corroboration of CRISM SWIR mineral detections to better constrain minerals contained within geologic units highlighted by potential Mastcam-Z parameters. With Mars 2020 landing site selection ongoing at the time of this writing, the attention of the community has turned toward the

geology within the proposed NE Syrtis landing ellipse. Ongoing efforts have gleaned some understanding of the local mineralogy and geology, namely the extent of carbonate-bearing deposits in the local stratigraphy. To test the efficacy of the suggested parameters, mapping was conducted for FRT174F4 and FRT1642E (Figure 37), two CRISM scenes covering the full expanse of the proposed NE Syrtis landing ellipse. Blue regions in the alteration mineralogy parameter composite (Figure 38e) display the location of carbonate-bearing deposits and blue regions in the mafic mineralogy parameter map (Figure 38f) show that olivine coexists with Mg-carbonate, as in FRTB8C2. Extracted spectra (Figure 39) bear a near-1900 nm hydration band and a 2300/2500 nm C-O stretching pair, confirming carbonate composition. These Mg-carbonate bearing units exhibit notable spectral differences in VNIR despite exhibiting similar bands in SWIR. The Mastcam-Z parameter composite shows no spatial correlation between the Mg-carbonate units in the CRISM SWIR map and the regions defined by R_{805}/R_{908} (which distinguishes carbonate-bearing material in FRTB8C2). Thus, suggested Mastcam-Z parameters may only be sensitive to region-specific spectral conditions and some other variable (aside from rock composition) may be controlling VNIR spectral variability on Mars. Given that much of the martian surface is covered by some amount of iron-oxide-rich dust that varies in thickness, it is possible that regional variations in dust conditions could be controlling the observed spectral differences. However, it is important to discuss that CRISM detector performance has declined with time. Effectiveness of the instrument's cooling system has waned, causing warmer detector temperatures to increase spectral noise (e.g., Carter et al., 2013). FRT174F4 and FRT1642E were acquired four years after MRO was inserted into Mars' orbit and the spectra acquired contain abundant noise spikes (Figure 39). While absorption bands for Mg-carbonates are clear in these spectra, the data quality of these observations is called into question.

3.3.5 Columbia Hills Results

Thee three key regions in the Columbia Hills were investigated using parameter maps and selected for spectra extraction (Figure 40): (1) portions of the eroded southwestern hills, (2) Home Plate,

and (3) portions of the high-albedo northern hills. Results of this mapping and spectral analysis are presented herein.

MCZ VNIR parameters developed for the Columbia Hills distinguish between the NE/SW volcanic plains, the NW/SE volcanic plains, the northern (region 3)/eastern Columbia Hills, the eroded southwestern Columbia Hills (region 1), and mafic sand dunes (Figure 41a,c; 42a,c) . R_{975}/R_{805} shown in red, highlights the bulk of the northern (region 3)/eastern Columbia Hills and the NE/SW volcanic plains. This parameter highlights more Columbia Hills terrain in FRT929F than FRT3192 (the selected CRISM observations for the Columbia Hills). R_{751}/R_{451} and R_{805}/R_{908} highlight the NW/SE volcanic plains, the eroded southwestern hills (region 1), and mafic sand deposits. FRT3192 shows significantly increased signal strength for R_{751}/R_{451} and R_{805}/R_{908} over FRT929F. CRISM SWIR summary parameters (Figure 41b,d) show a similar bimodal spectral variability between the NE/SW and NW/SE plains. This mapping reveals low-Ca pyroxene dominating the northern/eastern Columbia Hills and the immediately surrounding plains (Figure 41c,d) . Olivine signatures constitute the bulk of the mafic mineralogy in the southwestern hills and lowlands areas within the Columbia Hills complex (Figure 42b,d). High-Ca pyroxene occurs within small impact craters and in known mafic sand dunes (Figure 42b,d). Olivine is also present in numerous impact basins and ejecta blankets (Figure 42b,d). Significant detections of olivine and high-Ca pyroxene are noted in volcanic plains northwest and southeast of the Columbia Hills (Figure 41b,d). High-Ca pyroxene detections are more prominent in the northwest in FRT3192 and in the southeast in FRT929F (Figure 41b,d). Parameter detections in the southwest and northeast are confined to crater basins and ejecta blankets. Decorrelation stretches and MCZ RGB imagery (Figure 43) corroborate some of the spectral trends observed in MCZ VNIR and CRISM SWIR parameter maps. The NW/SE volcanic plains are darker in color than the light-brown NE/SW plains. The south/southwestern hills and the north/eastern hills also exhibit this color contrast. Dark, linear features abundant in the volcanic plains, regions where dust-devils have removed dust from the surface (e.g., Greeley et al., 2006), are darker,

more abundant, and more visually pronounced in FRT929F than FRT3192 (Figure 43a,d). FRT929F shows an overall darker surface than FRT3192. Simulated decorrelation stretches for the left and right eyes of Mastcam-Z show similar color disparity between NW/SE and NE/SW regions (Figure 43b,c,e,f). NW/SE regions are red in decorrelation stretches, indicating increased sensitivity to the 445 nm filter in the left eye and the 805 nm filter in the right eye. NE/SW regions are blue in decorrelation stretches indicating increased sensitivity to the 751 nm filter in the left eye and 1012 nm filter in the right eye.

Home Plate (region 2) and northern hills (region 3) SWIR spectra in FRT3192 slope positively toward longer wavelengths from 1040-2600 nm (Figure 44b). No notable absorption bands are observed. Southwestern hills (region 1) spectra in FRT3192 show a notable increase in reflectance from 1200-1600 nm (Figure 44b). In FRT929F, spectra from all three regions increase in reflectivity from ~1400-1600 nm and ~1900-2100 nm. This 1900-2100 nm reflectance increase includes a small absorption band centered near 2000 nm (Figure 44b). Home Plate and the northern hills SWIR spectra in FRT929F overall slope positively toward longer wavelengths, whereas the southwestern hills spectra shows minimal slope change (Figure 44b). In VNIR spectra (Figure 44a), FRT3192 Home Plate and northern hills spectra slope positively toward longer wavelengths. This slope is steepest from ~450-750 nm. FRT3192 southwestern hills spectra slope negatively toward longer wavelengths and absorption bands are present at 600 nm and 840 nm (Figure 44a). FRT929F Home Plate and northern hills spectra also slope positively toward longer wavelengths. Home Plate and the northern hills spectra from both CRISM scenes display a shallow, wide absorption band spanning 750-975 nm that centers near 870 nm (Figure 44a). Southwestern hills spectra in this scene slope negatively toward longer wavelengths, show a small absorption band centered near 530 nm, and a broad absorption band from 600-1050 nm (Figure 44a).

3.3.6 Columbia Hills Discussion

CRISM SWIR summary parameters at the Columbia Hills reveal a predominantly mafic mineralogy from orbit. No summary parameters were identified that highlight the known alteration mineralogies (e.g., Figure 42). However, SWIR spectra of the eroded southwestern hills (region 1) in FRT3192 exhibit a broad increase in reflectance from ~1250-1600nm, which is typically characteristic of olivine on Mars (e.g., Viviano-Beck et al., 2014).

Overall, the Columbia Hills' mineralogy is difficult to constrain from orbit, aside from the potential presence of olivine and pyroxene. This dearth of diagnostic spectral signatures is characteristic of the Columbia Hills and can be attributed to significant dust cover in the region. That is not to suggest there is no alteration mineralogy to be explored at the Columbia Hills – Spirit rover operations revealed a wide variety of mineral deposits indicative of extensive past aqueous activity (e.g., Arvidson et al., 2008; Farrand et al., 2016); however, alteration deposits identified by the Spirit rover at the Columbia Hills often span small spatial areas. With the ~18 m pixel size of investigated CRISM imagery, important alteration deposits investigated by Spirit are often subpixel-size from orbit and are, therefore, difficult to accurately constrain. (Carter and Poulet, 2012) identified carbonate and phyllosilicate-rich units from orbit, however these detections encompassed a small number of pixels in each case and were not reproducible in this work.

While SWIR spectra in the Columbia Hills showed little significant variability (Figure 44b), VNIR and MCZ spectra reveal two spectral endmembers (Figure 44a): red dominant and blue dominant. In both CRISM observations, spectra taken from Home Plate (region 2) and the northern hills (region 3) show significant red reflectance (relative to blue-green) and an absorption signature spanning 750-975 nm (Figure 44a). Fe^{3+} electronic transition processes can give rise to a broad absorption band within this region, often centered near 850 nm (e.g., Kong et al., 2011). Southwestern hills spectra, as evidenced by

the dark, blue-black color of the region in simulated Mastcam-Z RGB, show greater blue reflectance than green-red (Figure 44a). The southwestern hills spectrum in FRT3192 shows a broad absorption centered near 850 nm, likely the result of Fe^{3+} transitions and a band centered near 600 nm of unknown origin (Figure 44a). The southwestern hills in FRT929F shows a broad absorption stretching longward of 600 nm. This may be the beginning of a broad, 1000 nm centered Fe^{2+} transition band for olivine. VNIR spectra, thus, abundant Fe^{3+} bearing-material in the Columbia Hills and the southwestern hills may also bear Fe^{2+} contained in olivine.

At the Columbia Hills, Mastcam-Z VNIR parameters are sensitive to the volcanic plains, mafic sand dunes, and Columbia Hills rock. R_{751}/R_{445} nm highlights the northern (region 3)/eastern Columbia Hills and R_{600}/R_{805} and R_{805}/R_{908} distinguish the surrounding volcanic plains, mafic sands within the Columbia Hills, and small impact crater fill and ejecta (as shown in the simulated Mastcam-Z 3D perspective views in Figure 43). CRISM SWIR summary parameters show pockets of high-Ca pyroxene occurring in regions related to mafic sand dunes and within small craters. R_{805}/R_{908} corresponds well to these regions, suggesting this parameter may be sensitive to the spectral properties of high-Ca pyroxene at the Columbia Hills.

The sensitivity of these parameters varied significantly between the two tested CRISM images. As mentioned in the methods section, Lemmon et al., 2015 analyzed years of Spirit atmospheric data and described several seasonal fluctuations in dust activity in the region that recur annually. FRT3192 and FRT929F were acquired by CRISM at L_s of 139° and 12°. Among the most notable seasonal dust cycles identified by Lemmon et al. (2015) was a period of oscillating dust cover from 0-135° L_s. These two observations roughly fall within that season and, as evidenced by differences in RGB color and dust devil patterns, represent time periods of significantly different surface dust conditions. Spectral variability between the two scenes is likely a reflection of surface dust distribution controlling the 'redness' of the region.

Given the significant variability in signal strength of these parameters between observations (between dust seasons), it is not recommended that these parameters be widely used on the ground at the Columbia Hills. The Spirit rover enabled ground-truthing of several VNIR spectral parameters for this region. Farrand et al. (2016) outlines several Pancam spectral parameters. For Mastcam-Z operation in the Columbia Hills, it is recommended that these proven parameters be modified (Table 10) to the Mastcam-Z bandpasses.

3.4 Broad Discussion

3.4.1 VNIR Spectral Variability on Mars and Implications for Future Rover Missions

The inability of R_{805}/R_{908} to detect mineralogically similar units in a different region of NE Syrtis and the differences between spectral parameter sensitivity in the Columbia Hills between seasons raise a crucial question: are Mastcam-Z VNIR spectral parameters primarily sensitive to mineralogy, or does some other surficial material or photometric property, varying from region to region, govern VNIR spectral properties observed from orbit? Most of Mars' surface is covered by varying amounts of a global, anhydrous, iron-oxide-rich basaltic dust distributed by aoelian activity (e.g., McSween and Keil, 2000) (McSween and Keil, 2000). The prominent red reflectance of this material dominates the visible wavelengths. Some Mastcam-Z parameters correlate to visible color differences in simulated Mastcam-Z RGB Bayer composites (for example, some parameters highlight regions of the hills and surrounding plains that are red-brown in RGB versus regions that are black in RGB). Given the extent of red-brown martian regolith, this color correlation, disparities in parameter sensitivity through seasonal dust cycles at Columbia Hills, and disparities in parameter sensitivity spatially in different NE Syrtis regions, Mastcam-Z VNIR parameters may be primarily highlighting differences in surface color caused by surficial deposits and not bedrock composition. Thus, it is possible that these parameters are most sensitive to the color effects caused by varying dust cover. The suggested Mastcam-Z spectral

parameters do show sensitivity to regions with different chemical/mineralogical compositions, but it is important to consider that sensitivity may be region specific and controlled by variations in dust cover.

Orbital VNIR spectra have been underutilized and not well studied in the literature. Absorption bands in the SWIR wavelengths are diagnostic of numerous alteration minerals, presenting a more attractive wavelength range for orbital mineral identification, but this work demonstrates that VNIR parameters can be developed from orbit that are sensitive to the broad scale spectral variability in a single region. Region-specific parameters may also show some degree of variation based on season. Mapping of different seasons in the Columbia Hills in this work reveals that season-dependent dust activity has significant effect on the overall color and, therefore, the spectral variability of a region. This region-specific spectral variability can be used to devise preliminary filter combinations to perform reconnaissance with multispectral imagers. Spectral parameters suggested in this work, parameter maps created using those parameters, and comparisons to SWIR spectral parameter maps offer a unique dataset providing researchers with VNIR parameters to test once Mastcam-Z is on the surface. Parameters can be used to ground-truth differences in spectral variability occurring as seasons change and potentially expedite the identification of spectral endmembers for reconnaissance in the initial phases of the mission. Similar datasets would be useful for any future ground-based Mars mission featuring a multispectral imaging system.

3.4.2 Implications for the SuperCam Instrument

While Mastcam-Z will only be sensitive to reflectance in the VNIR, the Supercam instrument (successor to the ChemCam instrument on MSL Curiosity) will be sensitive to reflectance at longer wavelengths (1300 – 2600 nm; Clegg et al., 2015; Maurice et al., 2015). Unlike Mastcam-Z, SuperCam cannot acquire wide, stereo panoramic images. SuperCam is a point spectrometer capable of spot diameters ~45 µm at a 1.5 m distance and ~200 µm at a 7 m distance (Maurice et al., 2012, 2015).

Despite the small targetable region, SuperCam's SWIR will be sensitive to diagnostic bands of alteration minerals. Mastcam-Z will provide the first spectral reconnaissance on the ground, determining broad endmember compositions from a distance, potentially using parameters developed by this work, with the goal of identifying locations for sampling and caching. SuperCam benefits from this analysis, as Mastcam-Z reconnaissance would provide spots of interest for SuperCam analysis. This analysis pipeline can allow composition distribution to be mapped along the rover traverse and help pinpoint outcrops for thorough analysis with instruments requiring direct outcrop contact such as the Planetary Instrument for X-Ray Lithochemistry (PIXL; Allwood et al., 2016) and the Scanning Habitable Environments with Raman and Luminescence for Organics and Chemicals (SHERLOC; Beegle et al., 2014).

3.5 Conclusions

This work developed VNIR spectral parameters for the Mastcam-Z instrument at each Mars-2020 candidate landing site and investigated the primary controls on VNIR spectral variability at these regions. Data reveals the dominant minerals at each landing site and the efficacy of Mastcam-Z to corroborate broad-scale spectral distinctions observed from orbit. The key conclusions of this work are summarized as follows:

1. At Jezero Crater, simulated Mastcam-Z parameters correspond to regions known to contain alteration minerals by CRISM SWIR, spectrally distinguishing dark-toned, olivine-rich regions, such as the western delta front and exposed crater floor unit, Mg-carbonate bearing terrain north of the western delta and within the northern delta, and phyllosilicate-rich units – the high albedo hills within the landing ellipse and light-toned regions of the western delta.

2. South of the proposed landing ellipse in NE Syrtis, parameters were developed that correlate with CRISM SWIR summary parameters in the region. These parameters

distinguish sulfate-bearing units near/within the large cliff face, potentially kaolinite-bearing rugged terrain, olivine and Mg-carbonate bearing plateaus, some high-Ca pyroxene signatures, and the elongate ridge containing a potential serpentine component.

3. Within the NE Syrtis landing ellipse, Mastcam-Z VNIR parameters that distinguish Mg-carbonate bearing units in southern NE Syrtis fail to corroborate SWIR Mg-carbonate detections. Varying distribution of red iron-oxide dust may account for this discrepancy and may be the primary control on VNIR spectral properties on Mars.

4. At the Columbia Hills, simulated Mastcam-Z parameters derived from CRISM observations can distinguish the northern Columbia Hills, the eroded and darker-toned southern Columbia Hills, color differences between the NE/SW and NW/SE volcanic plains, and known mafic sand deposits.

5. Spectral parameters vary in extent between Columbia Hills observations acquired during different seasons. Dust conditions vary seasonally in this region and notable differences in regional color between the two different-time-of-season observations correlate to the extent of Mastcam-Z spectral parameters, suggesting that seasonal dust variation is a primary control on VNIR spectral variability.

3.6 Future Work

While this work has demonstrated that orbital hyperspectral data can be useful in performing preliminary reconnaissance for in-development ground-based multispectral imaging systems, more work can expand upon the conclusions made here. To better understand how martian dust plays a role in the VNIR variability of orbital spectra, comprehensive work quantifying changes in spectral 'redness' and band depth as a function of L_s is needed. This could be accomplished by performing VNIR spectral analysis on a wide array of CRISM images acquired at different L_s for a variety of regions. At present,

more CRISM observations would be required – few regions have multiple CRISM observations taken over the same area like the Columbia Hills. Constraining how L_s is directly related to VNIR spectral variability at future Mars mission landing sites could provide valuable data for fine-tuning preliminary parameters for future multispectral imagers.

To further support the use of orbitally-derived VNIR spectral parameters, this technique can be tested prior to the launch of Mars 2020. The wealth of experience provided by the Mastcam instrument aboard the Curiosity rover can provide this ground-truthing opportunity. I am currently developing CRISM-derived Mastcam parameters for mineralogic stratigraphy observed in Mt. Sharp using methods like those employed for this study. These orbital parameters can then be tested on the ground by Mastcam imagery (and compared to current Mastcam parameters) to determine the effectiveness of orbitally-derived VNIR spectral parameters.

CRISM is not the only orbital instrument that can be used to expand this work. The HiRISE instrument can acquire high-resolution 3-color imagery using 14 CCDs sensitive to visible-to-near infrared light (Delamere et al., 2010): 10 for red (RED), 2 for near-SWIR (SWIR), and 2 for blue-green (BG) Each grouping of CCDs constitutes a color "filter" sensitive to specific wavelength ranges: 550-850 nm for RED, <600 nm for BG, and <800nm for SWIR. Delamere et al. (2010) has outlined several ways in which HiRISE color imagery can be used to assess the composition of surface material. RGB composites using the SWIR, RED, and BG channels for red, green, and blue respectively show surface dust as yellow, sand and lithified rock as cyan to violet, and frost and ice as blue-white. Comparing these sorts of data products to CRISM VNIR could serve as a useful check on which Mastcam-Z parameters are sensitive to dust and which are sensitive to lithified rock. In HiRISE imagery, it is also possible to distinguish between material containing primary mafic minerals and material containing altered minerals. SWIR/BG ratios and BG/RED ratios for ferrous minerals are generally clustered, whereas SWIR/BG ratios are typically greater than BG/RED ratios in ferric minerals. This HiRISE data (in tandem with CRISM data) allow for a

clearer understanding of the stratigraphic contacts of these mineral phases given HiRISE's superior spatial resolution. This technique also provides further means to check the sensitivity of suggested Mastcam-Z parameters on Mars, identifying which parameters may be pinpointing spectral differences inherent to local alteration minerals and which parameters are not. The set of suggested Mastcam-Z parameters in this study provides a useful dataset to the ability of HiRISE and CRISM VNIR to work in tandem and the ability of these specific Mastcam-Z parameters to distinguish alteration minerals.

REFERENCES

Allen, C.C., Morris, R.V., Lindstrom, D.J., Lindstrom, M.M., Lockwood, J.P., 1997. JSC Mars-1-Martian regolith simulant, in: Lunar and Planetary Science Conference.

Alley, R., 1999. Algorithm Theoretical basis document for: decorrelation stretch.

Allwood, A.C., Wade, L.A., Hurowitz, J.A., 2016. PIXL Investigation on the Mars 2020 Rover. LPI Contrib. 1980.

Arvidson, R.E., Gooding, J.L., Moore, H.J., 1989. The Martian surface as imaged, sampled, and analyzed by the Viking landers. Rev. Geophys. 27, 39–60.

Arvidson, R.E., Ruff, S.W., Morris, R.V., Ming, D.W., Crumpler, L.S., Yen, A.S., Squyres, S.W., Sullivan, R.J., Bell, J.F., Cabrol, N.A., others, 2008. Spirit Mars rover mission to the Columbia Hills, Gusev Crater: Mission overview and selected results from the Cumberland Ridge to Home Plate. J. Geophys. Res. Planets 113.

Arvidson, R.E., Squyres, S.W., Anderson, R.C., Bell, J.F., Blaney, D., Brueckner, J., Cabrol, N.A., Calvin, W.M., Carr, M.H., Christensen, P.R., others, 2006. Overview of the spirit Mars exploration rover mission to Gusev Crater: Landing site to Backstay Rock in the Columbia Hills. J. Geophys. Res. Planets 111.

Baldridge, A.M., Hook, S.J., Grove, C.I., Rivera, G., 2009. The ASTER spectral library version 2.0. Remote Sens. Environ. 113, 711–715.

Bandfield, J.L., Glotch, T.D., Christensen, P.R., 2003. Spectroscopic identification of carbonate minerals in the Martian dust. Science 301, 1084–1087.

Bayly, J.G., Kartha, V.B., Stevens, W.H., 1963. The absorption spectra of liquid phase H2O, HDO and D2O from 0· 7 μm to 10 μm. Infrared Phys. 3, 211–222.

Beegle, L.W., Bhartia, R., DeFlores, L.P., Asher, S.A., Burton, A.S., Clegg, S.M., Conrad, P.G., Edgett, K.S., Ehlmann, B.L., Langenhorst, F., 2014. SHERLOC: scanning habitable environments with Raman & luminescence for organics & chemicals, an investigation for 2020, in: AGU Fall Meeting Abstracts.

Bell, J.F., Godber, A., McNair, S., Caplinger, M.A., Maki, J.N., Lemmon, M.T., Van Beek, J., Malin, M.C., Wellington, D., Kinch, K.M., 2017. The Mars Science Laboratory Curiosity Rover Mast Camera (Mastcam) Instruments: Pre-Flight and In-Flight Calibration, Validation, and Data Archiving. Earth Space Sci.

Bell, J.F., Joseph, J., Sohl-Dickstein, J.N., Arneson, H.M., Johnson, M.J., Lemmon, M.T., Savransky, D., 2006. In-flight calibration and performance of the Mars Exploration Rover Panoramic Camera (Pancam) instruments. J. Geophys. Res. Planets 111.

Bell, J.F., Maki, J.N., Mehall, G.L., Ravine, M.A., Caplinger, M.A., Mastcam-Z Team, 2016. Mastcam-Z: Designing a Geologic, Stereoscopic, and Multispectral Pair of Zoom Cameras for the NASA Mars 2020 Rover. LPI Contrib. 1980, 4126.

Bibring, J.-P., Langevin, Y., Mustard, J.F., Poulet, F., Arvidson, R., Gendrin, A., Gondet, B., Mangold, N., Pinet, P., Forget, F., others, 2006. Global mineralogical and aqueous Mars history derived from OMEGA/Mars Express data. Science 312, 400–404.

Bibring, J.-P., Soufflot, A., Berthé, M., Langevin, Y., Gondet, B., Drossart, P., Bouyé, M., Combes, M., Puget, P., Semery, A., others, 2004. OMEGA: Observatoire pour la Minéralogie, l'Eau, les Glaces et l'Activité, in: Mars Express: The Scientific Payload. pp. 37–49.

Bishop, J.L., Dobrea, E.Z.N., McKeown, N.K., Parente, M., Ehlmann, B.L., Michalski, J.R., Milliken, R.E., Poulet, F., Swayze, G.A., Mustard, J.F., others, 2008. Phyllosilicate diversity and past aqueous activity revealed at Mawrth Vallis, Mars. Science 321, 830–833.

Bishop, J.L., Murad, E., 2005. The visible and infrared spectral properties of jarosite and alunite. Am. Mineral. 90, 1100–1107.

Bishop, J.L., Murchie, S.L., Pieters, C.M., Zent, A.P., 2002. A model for formation of dust, soil, and rock coatings on Mars: Physical and chemical processes on the Martian surface. J. Geophys. Res. Planets 107.

Bouley, S., Ansan, V., Mangold, N., Masson, P., Neukum, G., 2009. Fluvial morphology of Naktong Vallis, Mars: A late activity with multiple processes. Planet. Space Sci. 57, 982–999.

Bradley, N.J., Schmidt, M.E., Bray, S.L., Perrett, G.M., 2017. Determining Dust Coverages on Rocks from MAHLI Images: Methodology and APXS Comparison, in: Lunar and Planetary Science Conference.

Bramble, M.S., Mustard, J.F., Salvatore, M.R., 2017. The geological history of Northeast Syrtis Major, Mars. Icarus 293, 66–93.

Brauhart, C.W., Huston, D.L., Groves, D.I., Mikucki, E.J., Gardoll, S.J., 2001. Geochemical mass-transfer patterns as indicators of the architecture of a complete volcanic-hosted massive sulfide hydrothermal alteration system, Panorama District, Pilbara, Western Australia. Econ. Geol. 96, 1263–1278.

Breuer, D., Spohn, T., Wüllner, U., 1993. Mantle differentiation and the crustal dichotomy of Mars. Planet. Space Sci. 41, 269–283.

Bridges, J.C., Grady, M.M., 2000. Evaporite mineral assemblages in the nakhlite (martian) meteorites. Earth Planet. Sci. Lett. 176, 267–279.

Broadwater, J., Banerjee, A., 2010. A generalized kernel for areal and intimate mixtures, in: Hyperspectral Image and Signal Processing: Evolution in Remote Sensing (WHISPERS), 2010 2nd Workshop On. IEEE, pp. 1–4.

Brown, A.J., Walter, M.R., Cudahy, T.J., 2005. Hyperspectral imaging spectroscopy of a Mars analogue environment at the North Pole Dome, Pilbara Craton, Western Australia. Aust. J. Earth Sci. 52, 353–364.

Cabrol, N.A., Grin, E.A., Landheim, R., Kuzmin, R.O., Greeley, R., 1998. Duration of the Ma'adim Vallis/Gusev crater hydrogeologic system, Mars. Icarus 133, 98–108.

Carr, M.H., Head III, J.W., 2010. Geologic history of Mars. Earth Planet. Sci. Lett., Mars Express after 6 Years in Orbit: Mars Geology from Three-Dimensional Mapping by the High Resolution Stereo Camera (HRSC) Experiment 294, 185–203. https://doi.org/10.1016/j.epsl.2009.06.042

Carter, J., Poulet, F., 2012. Orbital identification of clays and carbonates in Gusev crater. Icarus 219, 250–253.

Carter, J., Poulet, F., Bibring, J.-P., Mangold, N., Murchie, S., 2013. Hydrous minerals on Mars as seen by the CRISM and OMEGA imaging spectrometers: Updated global view. J. Geophys. Res. Planets 118, 831–858.

Chicarro, A., Martin, P., Trautner, R., 2004. The Mars Express mission: an overview, in: Mars Express: The Scientific Payload. pp. 3–13.

Christensen, P.R., Bandfield, J.L., Smith, M.D., Hamilton, V.E., Clark, R.N., 2000. Identification of a basaltic component on the Martian surface from Thermal Emission Spectrometer data. J. Geophys. Res. Planets 105, 9609–9621.

Clark, B.C., Arvidson, R.E., Gellert, R., Morris, R.V., Ming, D.W., Richter, L., Ruff, S.W., Michalski, J.R., Farrand, W.H., Yen, A., others, 2007. Evidence for montmorillonite or its compositional equivalent in Columbia Hills, Mars. J. Geophys. Res. Planets 112.

Clark, R.N., King, T.V., Klejwa, M., Swayze, G.A., Vergo, N., 1990. High spectral resolution reflectance spectroscopy of minerals. J. Geophys. Res. Solid Earth 95, 12653–12680.

Clark, R.N., others, 1999. Spectroscopy of rocks and minerals, and principles of spectroscopy. Man. Remote Sens. 3, 3–58.

Clark, R.N., Roush, T.L., 1984a. Reflectance spectroscopy: Quantitative analysis techniques for remote sensing applications. J. Geophys. Res. Solid Earth 1978–2012 89, 6329–6340.

Clark, R.N., Roush, T.L., 1984b. Reflectance spectroscopy: Quantitative analysis techniques for remote sensing applications. J. Geophys. Res. Solid Earth 89, 6329–6340.

Clegg, S.M., Wiens, R.C., Maurice, S., Gasnault, O., Sharma, S.K., Misra, A.K., Newell, R., Forni, O., Lasue, J., Anderson, R.B., others, 2015. Remote geochemical and mineralogical analysis with supercam for the Mars 2020 rover, in: Lunar and Planetary Science Conference. p. 2781.

Cloutis, E., Craig, M., Kaletzke, L., McCormack, K., Stewart, L., 2006. HOSERLab: A new planetary spectrophotometer facility, in: 37th Annual Lunar and Planetary Science Conference. p. 2121.

Cloutis, E.A., Gaffey, M.J., 1991. Spectral-compositional variations in the constituent minerals of mafic and ultramafic assemblages and remote sensing implications. Earth Moon Planets 53, 11–53.

Cloutis, E.A., Hawthorne, F.C., Mertzman, S.A., Krenn, K., Craig, M.A., Marcino, D., Methot, M., Strong, J., Mustard, J.F., Blaney, D.L., others, 2006. Detection and discrimination of sulfate minerals using reflectance spectroscopy. Icarus 184, 121–157.

Crowley, J.K., Williams, D.E., Hammarstrom, J.M., Piatak, N., Chou, I.-M., Mars, J.C., 2003. Spectral reflectance properties (0.4–2.5 μm) of secondary Fe-oxide, Fe-hydroxide, and Fe-sulphate-hydrate minerals associated with sulphide-bearing mine wastes. Geochem. Explor. Environ. Anal. 3, 219–228.

Cull, S., Arvidson, R.E., Mellon, M.T., Skemer, P., Shaw, A., Morris, R.V., 2010. Compositions of subsurface ices at the Mars Phoenix landing site. Geophys. Res. Lett. 37.

Cull, S.C., Arvidson, R.E., Catalano, J.G., Ming, D.W., Morris, R.V., Mellon, M.T., Lemmon, M., 2010. Concentrated perchlorate at the Mars Phoenix landing site: Evidence for thin film liquid water on Mars. Geophys. Res. Lett. 37.

Delamere, W.A., Tornabene, L.L., McEwen, A.S., Becker, K., Bergstrom, J.W., Bridges, N.T., Eliason, E.M., Gallagher, D., Herkenhoff, K.E., Keszthelyi, L., 2010. Color imaging of Mars by the High Resolution Imaging Science Experiment (HiRISE). Icarus 205, 38–52.

Ehlmann, B.L., Anderson, F.S., Andrews-Hanna, J., Catling, D.C., Christensen, P.R., Cohen, B.A., Dressing, C.D., Edwards, C.S., Elkins-Tanton, L.T., Farley, K.A., 2016. The sustainability of habitability on terrestrial planets: Insights, questions, and needed measurements from Mars for understanding the evolution of Earth-like worlds. J. Geophys. Res. Planets 121, 1927–1961.

Ehlmann, B.L., Edwards, C.S., 2014. Mineralogy of the Martian surface. Annu. Rev. Earth Planet. Sci. 42, 291–315.

Ehlmann, B.L., Mustard, J.F., 2012. An in-situ record of major environmental transitions on early Mars at Northeast Syrtis Major. Geophys. Res. Lett. 39.

Ehlmann, B.L., Mustard, J.F., Fassett, C.I., Schon, S.C., Head III, J.W., Des Marais, D.J., Grant, J.A., Murchie, S.L., 2008a. Clay minerals in delta deposits and organic preservation potential on Mars. Nat. Geosci. 1, 355–358.

Ehlmann, B.L., Mustard, J.F., Murchie, S.L., Bibring, J.-P., Meunier, A., Fraeman, A.A., Langevin, Y., 2011. Subsurface water and clay mineral formation during the early history of Mars. Nature 479, 53–60.

Ehlmann, B.L., Mustard, J.F., Murchie, S.L., Poulet, F., Bishop, J.L., Brown, A.J., Calvin, W.M., Clark, R.N., Des Marais, D.J., Milliken, R.E., others, 2008b. Orbital identification of carbonate-bearing rocks on Mars. Science 322, 1828–1832.

Ehlmann, B.L., Mustard, J.F., Swayze, G.A., Clark, R.N., Bishop, J.L., Poulet, F., Des Marais, D.J., Roach, L.H., Milliken, R.E., Wray, J.J., others, 2009. Identification of hydrated silicate minerals on Mars using MRO-CRISM: Geologic context near Nili Fossae and implications for aqueous alteration. J. Geophys. Res. Planets 114.

Farrand, W.H., Bell III, J.F., Johnson, J.R., Rice, M.S., Hurowitz, J.A., 2013. VNIR multispectral observations of rocks at Cape York, Endeavour crater, Mars by the Opportunity rover's Pancam. Icarus 225, 709–725. https://doi.org/10.1016/j.icarus.2013.04.014

Farrand, W.H., Johnson, J.R., Rice, M.S., Wang, A., Bell, J.F., 2016. VNIR multispectral observations of aqueous alteration materials by the Pancams on the Spirit and Opportunity Mars Exploration Rovers. Am. Mineral. 101, 2005–2019.

Fassett, C.I., Head, J.W., 2011. Sequence and timing of conditions on early Mars. Icarus 211, 1204–1214.

Fassett, C.I., Head, J.W., 2005. Fluvial sedimentary deposits on Mars: Ancient deltas in a crater lake in the Nili Fossae region. Geophys. Res. Lett. 32.

Feldman, W.C., Mellon, M.T., Maurice, S., Prettyman, T.H., Carey, J.W., Vaniman, D.T., Bish, D.L., Fialips, C.I., Chipera, S.J., Kargel, J.S., 2004. Hydrated states of MgSO4 at equatorial latitudes on Mars. Geophys. Res. Lett. 31.

Frost, R.L., Kloprogge, J.T., Ding, Z., 2002. Near-infrared spectroscopic study of nontronites and ferruginous smectite. Spectrochim. Acta. A. Mol. Biomol. Spectrosc. 58, 1657–1668.

Gaffey, S.J., 1985. Reflectance spectroscopy in the visible and near-infrared (0.35–2.55 μm): Applications in carbonate petrology. Geology 13, 270–273. https://doi.org/10.1130/0091-7613(1985)13<270:RSITVA>2.0.CO;2

Gat, N., 2000. Imaging spectroscopy using tunable filters: a review, in: Proc. Spie. pp. 50–64.

Gendrin, A., Mangold, N., Bibring, J.-P., Langevin, Y., Gondet, B., Poulet, F., Bonello, G., Quantin, C., Mustard, J., Arvidson, R., others, 2005. Sulfates in Martian layered terrains: the OMEGA/Mars Express view. Science 307, 1587–1591.

Gillespie, A.R., Kahle, A.B., Walker, R.E., 1986. Color enhancement of highly correlated images. I. Decorrelation and HSI contrast stretches. Remote Sens. Environ. 20, 209–235.

Golden, D.C., Ming, D.W., Morris, R.V., Mertzman, S.A., 2005. Laboratory-simulated acid-sulfate weathering of basaltic materials: Implications for formation of sulfates at Meridiani Planum and Gusev crater, Mars. J. Geophys. Res. Planets 110, E12S07. https://doi.org/10.1029/2005JE002451

Golombek, M.P., Bridges, N.T., 2000. Erosion rates on Mars and implications for climate change: Constraints from the Pathfinder landing site. J. Geophys. Res. Planets 105, 1841–1853.

Golombek, M.P., Cook, R.A., Economou, T., Folkner, W.M., Haldemann, A.F.C., Kallemeyn, P.H., Knudsen, J.M., Manning, R.M., Moore, H.J., Parker, T.J., others, 1997. Overview of the Mars Pathfinder mission and assessment of landing site predictions. Science 278, 1743–1748.

Golombek, M.P., Crumpler, L.S., Grant, J.A., Greeley, R., Cabrol, N.A., Parker, T.J., Rice, J.W., Ward, J.G., Arvidson, R.E., Moersch, J.E., others, 2006. Geology of the Gusev cratered plains from the Spirit rover transverse. J. Geophys. Res. Planets 111.

Goudge, T.A., Mohrig, D., Cardenas, B.T., Hughes, C.M., Fassett, C.I., 2017. Stratigraphy and paleohydrology of delta channel deposits, Jezero crater, Mars. Icarus.

Goudge, T.A., Mustard, J.F., Head, J.W., Fassett, C.I., Wiseman, S.M., 2015a. Assessing the mineralogy of the watershed and fan deposits of the Jezero crater paleolake system, Mars. J. Geophys. Res. Planets 120, 775–808.

Goudge, T.A., Mustard, J.F., Head, J.W., Fassett, C.I., Wiseman, S.M., 2015b. Assessing the mineralogy of the watershed and fan deposits of the Jezero crater paleolake system, Mars. J. Geophys. Res. Planets 120, 775–808.

Graf, J.E., Zurek, R.W., Eisen, H.J., Jai, B., Johnston, M.D., DePaula, R., 2005. The Mars reconnaissance orbiter mission. Acta Astronaut. 57, 566–578.

Grant, J.A., Golombek, M.P., Grotzinger, J.P., Wilson, S.A., Watkins, M.M., Vasavada, A.R., Griffes, J.L., Parker, T.J., 2011. The science process for selecting the landing site for the 2011 Mars Science Laboratory. Planet. Space Sci. 59, 1114–1127.

Greeley, R., Whelley, P.L., Arvidson, R.E., Cabrol, N.A., Foley, D.J., Franklin, B.J., Geissler, P.G., Golombek, M.P., Kuzmin, R.O., Landis, G.A., others, 2006. Active dust devils in Gusev crater, Mars: observations from the Mars exploration rover spirit. J. Geophys. Res. Planets 111.

Grotzinger, J.P., Crisp, J.A., Vasavada, A.R., others, 2015. Curiosity's Mission of Exploration at Gale Crater, Mars. Elements 11, 19–26.

Grotzinger, J.P., Milliken, R.E., 2012. The sedimentary rock record of Mars: Distribution, origins, and global stratigraphy. Sediment. Geol. Mars 102, 1–48.

Grotzinger, J.P., Sumner, D.Y., Kah, L.C., Stack, K., Gupta, S., Edgar, L., Rubin, D., Lewis, K., Schieber, J., Mangold, N., others, 2014. A habitable fluvio-lacustrine environment at Yellowknife Bay, Gale Crater, Mars. Science 343, 1242777.

Gunn, M.D., Cousins, C.R., 2016. Mars surface context cameras past, present, and future. Earth Space Sci. 3, 144–162.

Halliday, A.N., Wänke, H., Birck, J.-L., Clayton, R.N., 2001. The accretion, composition and early differentiation of Mars. Space Sci. Rev. 96, 197–230.

Hammond, W.A., Withrow, J.R., 1933. Soluble Anhydrite as a Desiccating Agent. Ind. Eng. Chem. 25, 653–659. https://doi.org/10.1021/ie50282a018

Hapke, B., 2012. Theory of reflectance and emittance spectroscopy. Cambridge university press.

Hartmann, W.K., Winterhalter, D., Geiss, J., 2005. Chronology and physical evolution of planet Mars. Sol. Syst. Beyond—ten Years ISSI ISSI Bern SR-003 211–228.

Herzberg, G., 1945. Infrared and Raman spectra of polyatomic molecules. D. Van Nostrand Company.; New York.

Hiesinger, H., Head, J.W., 2004. The Syrtis Major volcanic province, Mars: Synthesis from Mars global surveyor data. J. Geophys. Res. Planets 109.

Hoke, M.R.T., Hynek, B.M., 2009. Valley network formation on the ancient highlands of Mars occurred in the late Noachian and early Hesperian epochs, in: Lunar and Planetary Science Conference. p. 1885.

Hunt, G.R., 1977. Spectral signatures of particulate minerals in the visible and near infrared. Geophysics 42, 501–513.

Irwin, R.P., Maxwell, T.A., Howard, A.D., Craddock, R.A., Leverington, D.W., 2002. A large paleolake basin at the head of Ma'adim Vallis, Mars. Science 296, 2209–2212.

Jakosky, B.M., Phillips, R.J., 2001. Mars' volatile and climate history. nature 412, 237–244.

Johnson, J.R., Achilles, C., Bell, J.F., Bender, S., Cloutis, E., Ehlmann, B., Fraeman, A., Gasnault, O., Hamilton, V.E., Le Mouélic, S., 2017. Visible/near-infrared spectral diversity from in situ observations of the Bagnold Dune Field sands in Gale Crater, Mars. J. Geophys. Res. Planets.

Johnson, J.R., Grundy, W.M., 2001. Visible/near-infrared spectra and two-layer modeling of palagonite-coated basalts. Geophys. Res. Lett. 28, 2101–2104.

King, S.J., Bishop, J.L., Brown, A.J., 2014. Spectral Properties of Ca-, Mg-, and Fe-bearing Carbonates and Implications for Mars, in: Eighth International Conference on Mars. p. 1177.

King, T.V., Ridley, W.I., 1987. Relation of the spectroscopic reflectance of olivine to mineral chemistry and some remote sensing implications. J. Geophys. Res. Solid Earth 92, 11457–11469.

Kirk, R.L., Howington-Kraus, E., Rosiek, M.R., Anderson, J.A., Archinal, B.A., Becker, K.J., Cook, D.A., Galuszka, D.M., Geissler, P.E., Hare, T.M., 2008. Ultrahigh resolution topographic mapping of Mars with MRO HiRISE stereo images: Meter-scale slopes of candidate Phoenix landing sites. J. Geophys. Res. Planets 113.

Klingelhöfer, G., Morris, R.V., Bernhardt, B., Schröder, C., Rodionov, D.S., Souza, P.A. de, Yen, A., Gellert, R., Evlanov, E.N., Zubkov, B., Foh, J., Bonnes, U., Kankeleit, E., Gütlich, P., Ming, D.W., Renz, F., Wdowiak, T., Squyres, S.W., Arvidson, R.E., 2004. Jarosite and Hematite at Meridiani Planum from Opportunity's Mössbauer Spectrometer. Science 306, 1740–1745. https://doi.org/10.1126/science.1104653

Kokaly, R.F., Clark, R.N., Swayze, G.A., Livo, K.E., Hoefen, T.M., Pearson, N.C., Wise, R.A., Benzel, W.M., Lowers, H.A., Driscoll, R.L., Klein, A.J., 2017. USGS Spectral Library Version 7 (USGS Numbered Series No. 1035), Data Series. U.S. Geological Survey, Reston, VA.

Kong, W.G., Wang, A., Freeman, J.J., Sobron, P., 2011. A comprehensive spectroscopic study of synthetic Fe2+, Fe3+, Mg2+ and Al3+ copiapite by Raman, XRD, LIBS, MIR and vis–NIR. J. Raman Spectrosc. 42, 1120–1129.

Lane, M.D., Bishop, J.L., Dyar, M.D., King, P.L., Parente, M., Hyde, B.C., 2008. Mineralogy of the Paso Robles soils on Mars. Am. Mineral. 93, 728–739.

Lemmon, M.T., Smith, P.H., Shinohara, C., Tanner, R., Woida, P., Shaw, A., Hughes, J., Reynolds, R., Woida, R., Penegor, J., others, 2008. The Phoenix surface stereo imager (SSI) investigation, in: Lunar and Planetary Science Conference. p. 2156.

Lemmon, M.T., Wolff, M.J., Bell, J.F., Smith, M.D., Cantor, B.A., Smith, P.H., 2015. Dust aerosol, clouds, and the atmospheric optical depth record over 5 Mars years of the Mars Exploration Rover mission. Icarus 251, 96–111.

Mangold, N., Carter, J., Poulet, F., Dehouck, E., Ansan, V., Loizeau, D., 2012. Late Hesperian aqueous alteration at Majuro crater, Mars. Planet. Space Sci. 72, 18–30.

Marzo, G.A., Davila, A.F., Tornabene, L.L., Dohm, J.M., Fairén, A.G., Gross, C., Kneissl, T., Bishop, J.L., Roush, T.L., McKay, C.P., 2010. Evidence for Hesperian impact-induced hydrothermalism on Mars. Icarus 208, 667–683.

Maurice, S., Cousin, A., Wiens, R.C., Gasnault, O., Parès, L., Forni, O., Meslin, P.-Y., Clegg, S., Team, C., 2012. Laser Induced Breakdown Spectroscopy (LIBS) spot size at Stand-off distances with ChemCam, in: Lunar and Planetary Science Conference.

Maurice, S., Wiens, R.C., Anderson, R., Beyssac, O., Bonal, L., Clegg, S., DeFlores, L., Dromart, G., Fischer, W., Forni, O., others, 2015. Science objectives of the SuperCam instrument for the Mars2020 rover, in: Lunar and Planetary Science Conference. p. 2818.

McCoy, T.J., Sims, M., Schmidt, M.E., Edwards, L., Tornabene, L.L., Crumpler, L.S., Cohen, B.A., Soderblom, L.A., Blaney, D.L., Squyres, S.W., others, 2008. Structure, stratigraphy, and origin of Husband Hill, Columbia Hills, Gusev Crater, Mars. J. Geophys. Res. Planets 113.

McEwen, A.S., Eliason, E.M., Bergstrom, J.W., Bridges, N.T., Hansen, C.J., Delamere, W.A., Grant, J.A., Gulick, V.C., Herkenhoff, K.E., Keszthelyi, L., 2007. Mars reconnaissance orbiter's high resolution imaging science experiment (HiRISE). J. Geophys. Res. Planets 112.

McGuire, P.C., Bishop, J.L., Brown, A.J., Fraeman, A.A., Marzo, G.A., Morgan, M.F., Murchie, S.L., Mustard, J.F., Parente, M., Pelkey, S.M., others, 2009. An improvement to the volcano-scan algorithm for atmospheric correction of CRISM and OMEGA spectral data. Planet. Space Sci. 57, 809–815.

McSween, H.Y., Keil, K., 2000. Mixing relationships in the Martian regolith and the composition of globally homogeneous dust. Geochim. Cosmochim. Acta 64, 2155–2166.

McSween, H.Y., Ruff, S.W., Morris, R.V., Bell, J.F., Herkenhoff, K., Gellert, R., Stockstill, K.R., Tornabene, L.L., Squyres, S.W., Crisp, J.A., others, 2006. Alkaline volcanic rocks from the Columbia Hills, Gusev crater, Mars. J. Geophys. Res. Planets 111.

Milliken, R.E., Edgett, K.S., Swayze, G., Clark, R.N., Thomson, B.J., Anderson, R., Bell III, J.F., 2009. Clay and sulfate-bearing rocks in a stratigraphic sequence in Gale Crater. Lunar Planet Sci 40 1479 Abstr.

Ming, D.W., Mittlefehldt, D.W., Morris, R.V., Golden, D.C., Gellert, R., Yen, A., Clark, B.C., Squyres, S.W., Farrand, W.H., Ruff, S.W., others, 2006. Geochemical and mineralogical indicators for aqueous processes in the Columbia Hills of Gusev crater, Mars. J. Geophys. Res. Planets 111.

Moroz, L.V., Basilevsky, A.T., Hiroi, T., Rout, S.S., Baither, D., Van Der Bogert, C.H., Yakovlev, O.I., Fisenko, A.V., Semjonova, L.F., Rusakov, V.S., 2009. Spectral properties of simulated impact glasses produced from martian soil analogue JSC Mars-1. Icarus 202, 336–353.

Morris, R.V., Graff, T.G., Achilles, C.N., Agresti, D.G., Ming, D.W., Golden, D.C., 2011. Visible and near-IR reflectance spectra of Mars analogue materials under arid conditions for interpretation of Martian surface mineralogy.

Morris, R.V., Ming, D.W., Golden, D.C., Graff, T.G., Achilles, C.N., 2010. Evidence for Interlayer Collapse of Nontronite on Mars from Laboratory Visible and Near-IR Reflective Spectra.

Murchie, S., Arvidson, R., Bedini, P., Beisser, K., Bibring, J.-P., Bishop, J., Boldt, J., Cavender, P., Choo, T., Clancy, R.T., others, 2007. Compact reconnaissance imaging spectrometer for Mars (CRISM) on Mars reconnaissance orbiter (MRO). J. Geophys. Res. Planets 1991–2012 112.

Murchie, S.L., Seelos, F.P., Hash, C.D., Humm, D.C., Malaret, E., McGovern, J.A., Choo, T.H., Seelos, K.D., Buczkowski, D.L., Morgan, M.F., others, 2009. Compact Reconnaissance Imaging Spectrometer for Mars investigation and data set from the Mars Reconnaissance Orbiter's primary science phase. J. Geophys. Res. Planets 114.

Murphy, J.R., 1999. The Martian atmospheric dust cycle: Insights from numerical model simulations, in: The Fifth International Conference on Mars. p. 6087.

Mustard, J.F., Adler, M., Allwood, A., Bass, D.S., Beaty, D.W., Bell III, J.F., Brinckerhoff, W.B., Carr, M., Des Marais, D.J., Drake, B., others, 2013. Report of the Mars 2020 science definition team. Posted July 154.

Mustard, J.F., Ehlmann, B.L., Skok, J.R., Des Marais, D., Mangold, N., Poulet, F., 2010. Intact stratigraphy traversing the phyllosilicate to sulfate eras at the Syrtis-Isidis contact, Mars, in: Lunar and Planetary Science Conference XLI, 2070.

Mustard, J.F., Murchie, S.L., Pelkey, S.M., Ehlmann, B.L., Milliken, R.E., Grant, J.A., Bibring, J.-P., Poulet, F., Bishop, J., Dobrea, E.N., others, 2008. Hydrated silicate minerals on Mars observed by the Mars Reconnaissance Orbiter CRISM instrument. Nature 454, 305–309.

Mutch, T.A., Binder, A.B., Huck, F.O., Levinthal, E.C., Morris, E.C., Sagan, C., Young, A.T., 1972. Imaging experiment: the Viking lander. Icarus 16, 92–110.

Nachon, M., Clegg, S.M., Mangold, N., Schröder, S., Kah, L.C., Dromart, G., Ollila, A., Johnson, J.R., Oehler, D.Z., Bridges, J.C., others, 2014. Calcium sulfate veins characterized by ChemCam/Curiosity at Gale crater, Mars. J. Geophys. Res. Planets 119, 1991–2016.

Nascimento, J.M., Bioucas-Dias, J.M., 2010. Unmixing hyperspectral intimate mixtures, in: Remote Sensing. International Society for Optics and Photonics, p. 78300C–78300C.

Nimmo, F., Tanaka, K., 2005. Early crustal evolution of Mars 1. Annu Rev Earth Planet Sci 33, 133–161.

Owen, T., 1992. The composition and early history of the atmosphere of Mars. Mars 818–834.

Pelkey, S.M., Mustard, J.F., Murchie, S., Clancy, R.T., Wolff, M., Smith, M., Milliken, R., Bibring, J.-P., Gendrin, A., Poulet, F., others, 2007. CRISM multispectral summary products: Parameterizing mineral diversity on Mars from reflectance. J. Geophys. Res. Planets 112.

Phebus, B.D., Johnson, A.V., Mar, B., Stone, B.M., Colaprete, A., Iraci, L.T., 2011. Water ice nucleation characteristics of JSC Mars-1 regolith simulant under simulated Martian atmospheric conditions. J. Geophys. Res. Planets 116.

Pieters, C.M., Hiroi, T., 2004. RELAB (Reflectance Experiment Laboratory): A NASA multiuser spectroscopy facility, in: Lunar and Planetary Science Conference.

Poulet, F., Erard, S., 2004. Nonlinear spectral mixing: Quantitative analysis of laboratory mineral mixtures. J. Geophys. Res. Planets 109.

Rice, M.S., Bell III, J.F., Cloutis, E.A., Wang, A., Ruff, S.W., Craig, M.A., Bailey, D.T., Johnson, J.R., de Souza Jr., P.A., Farrand, W.H., 2010. Silica-rich deposits and hydrated minerals at Gusev Crater, Mars: Vis-NIR spectral characterization and regional mapping. Icarus 205, 375–395. https://doi.org/10.1016/j.icarus.2009.03.035

Rice, M.S., Bell, J.F., III, Godber, A., Wellington, D., Fraeman, A.A., Johnson, J.R., Kinch, K.M., Malin, M.C., Grotzinger, J.P., 2013. Mastcam multispectral imaging results from the Mars Science Laboratory investigation in Yellowknife Bay. Eur. Planet. Sci. Congr. 2013 Held 8-13 Sept. Lond. UK Online Httpmeetingscopernicusorgepsc2013 IdEPSC2013-762 8, EPSC2013-762.

Ruff, S.W., Farmer, J.D., 2016. Silica deposits on Mars with features resembling hot spring biosignatures at El Tatio in Chile. Nat. Commun. 7, 13554.

Salvatore, M.R., Goudge, T.A., Bramble, M.S., Edwards, C.S., Bandfield, J.L., Amador, E.S., Mustard, J.F., Christensen, P.R., 2017. Bulk mineralogy of the NE Syrtis and Jezero crater regions of Mars derived through thermal infrared spectral analyses. Icarus.

Schmidt, M.E., Ruff, S.W., McCoy, T.J., Farrand, W.H., Johnson, J.R., Gellert, R., Ming, D.W., Morris, R.V., Cabrol, N., Lewis, K.W., others, 2008. Hydrothermal origin of halogens at Home Plate, Gusev crater. J. Geophys. Res. Planets 113.

Schon, S.C., Head, J.W., Fassett, C.I., 2012. An overfilled lacustrine system and progradational delta in Jezero crater, Mars: Implications for Noachian climate. Planet. Space Sci. 67, 28–45.

Shkuratov, Y., Starukhina, L., Hoffmann, H., Arnold, G., 1999. A model of spectral albedo of particulate surfaces: Implications for optical properties of the Moon. Icarus 137, 235–246.

Smith, P.H., Bell, J.F., Bridges, N.T., Britt, D.T., Gaddis, L., Greeley, R., Keller, H.U., Herkenhoff, K.E., Jaumann, R., Johnson, J.R., others, 1997. Results from the Mars Pathfinder camera. Science 278, 1758–1765.

Smith, P.H., Tomasko, M.G., Britt, D., Crowe, D.G., Reid, R., Keller, H.U., Thomas, N., Gliem, F., Rueffer, P., Sullivan, R., others, 1997. The imager for Mars Pathfinder experiment. J. Geophys. Res. Planets 102, 4003–4025.

Squyres, Arvidson, R.E., Bell, J.F., Brückner, J., Cabrol, N.A., Calvin, W., Carr, M.H., Christensen, P.R., Clark, B.C., Crumpler, L., others, 2004. The Opportunity Rover's Athena science investigation at Meridiani Planum, Mars. Science 306, 1698–1703.

Squyres, S.W., Aharonson, O., Clark, B.C., Cohen, B.A., Crumpler, L., De Souza, P.A., Farrand, W.H., Gellert, R., Grant, J., Grotzinger, J.P., others, 2007. Pyroclastic activity at home plate in Gusev Crater, Mars. Science 316, 738–742.

Squyres, S.W., Arvidson, R.E., Baumgartner, E.T., Bell, J.F., Christensen, P.R., Gorevan, S., Herkenhoff, K.E., Klingelhöfer, G., Madsen, M.B., Morris, R.V., 2003. Athena Mars rover science investigation. J. Geophys. Res. Planets 108.

Squyres, S.W., Arvidson, R.E., Bell, J.F., Brückner, J., Cabrol, N.A., Calvin, W., Carr, M.H., Christensen, P.R., Clark, B.C., Crumpler, L., others, 2004. The Spirit rover's Athena science investigation at Gusev crater, Mars. science 305, 794–799.

Squyres, S.W., Arvidson, R.E., Bell, J.F., Calef, F., Clark, B.C., Cohen, B.A., Crumpler, L.A., De Souza, P.A., Farrand, W.H., Gellert, R., others, 2012. Ancient impact and aqueous processes at Endeavour Crater, Mars. Science 336, 570–576.

Squyres, S.W., Arvidson, R.E., Bollen, D., Bell, J.F., Brueckner, J., Cabrol, N.A., Calvin, W.M., Carr, M.H., Christensen, P.R., Clark, B.C., others, 2006. Overview of the opportunity mars exploration rover mission to meridiani planum: Eagle crater to purgatory ripple. J. Geophys. Res. Planets 111.

Squyres, S.W., Grotzinger, J.P., Arvidson, R.E., Bell, J.F., Calvin, W., Christensen, P.R., Clark, B.C., Crisp, J.A., Farrand, W.H., Herkenhoff, K.E., others, 2004. In situ evidence for an ancient aqueous environment at Meridiani Planum, Mars. Science 306, 1709–1714.

Stack, K.M., Milliken, R.E., 2015. Modeling near-infrared reflectance spectra of clay and sulfate mixtures and implications for Mars. Icarus 250, 332–356.

Tosca, N.J., Knoll, A.H., McLennan, S.M., 2008. Water activity and the challenge for life on early Mars. Science 320, 1204–1207.

Tosca, N.J., McLennan, S.M., 2006. Chemical divides and evaporite assemblages on Mars. Earth Planet. Sci. Lett. 241, 21–31.

van Kan Parker, M., Zegers, T., Kneissl, T., Ivanov, B., Foing, B., Neukum, G., 2010. 3D structure of the Gusev Crater region. Earth Planet. Sci. Lett. 294, 411–423.

Vaniman, D.T., Bish, D.L., Chipera, S.J., Fialips, C.I., Carey, J.W., Feldman, W.C., 2004. Magnesium sulphate salts and the history of water on Mars. Nature 431, 663–665.

Vaniman, D.T., Bish, D.L., Ming, D.W., Bristow, T.F., Morris, R.V., Blake, D.F., Chipera, S.J., Morrison, S.M., Treiman, A.H., Rampe, E.B., others, 2014a. Mineralogy of a mudstone at Yellowknife Bay, Gale crater, Mars. Science 343, 1243480.

Vaniman, D.T., Bish, D.L., Ming, D.W., Bristow, T.F., Morris, R.V., Blake, D.F., Chipera, S.J., Morrison, S.M., Treiman, A.H., Rampe, E.B., others, 2014b. Mineralogy of a mudstone at Yellowknife Bay, Gale crater, Mars. Science 343, 1243480.

Vaniman, D.T., Chipera, S.J., 2006. Transformations of Mg-and Ca-sulfate hydrates in Mars regolith. Am. Mineral. 91, 1628–1642.

Vantiman, D.T., Martinez, G.M., Rampe, E.B., Bristow, T.F., Blake, D.F., Yen, A.H., Ming, D.W., Rapin, W., Meslin, P.-Y., Morookian, J.M., others, 2017. Calcium Sulfates at Gale Crater and Limitations on Gypsum Stability.

Velde, B., 2013. Origin and mineralogy of clays: clays and the environment. Springer Science & Business Media.

Viviano-Beck, C.E., Seelos, F.P., Murchie, S.L., Kahn, E.G., Seelos, K.D., Taylor, H.W., Taylor, K., Ehlmann, B.L., Wiseman, S.M., Mustard, J.F., others, 2014. Revised CRISM spectral parameters and summary products based on the currently detected mineral diversity on Mars. J. Geophys. Res. Planets 119, 1403–1431.

Wang, A., Bell, J.F., Li, R., Johnson, J.R., Farrand, W.H., Cloutis, E.A., Arvidson, R.E., Crumpler, L., Squyres, S.W., McLennan, S.M., others, 2008. Light-toned salty soils and coexisting Si-rich species discovered by the Mars Exploration Rover Spirit in Columbia Hills. J. Geophys. Res. Planets 113.

Wang, A., Haskin, L.A., Squyres, S.W., Jolliff, B.L., Crumpler, L., Gellert, R., Schröder, C., Herkenhoff, K., Hurowitz, J., Tosca, N.J., Farrand, W.H., Anderson, R., Knudson, A.T., 2006. Sulfate deposition in subsurface regolith in Gusev crater, Mars. J. Geophys. Res. Planets 111, E02S17. https://doi.org/10.1029/2005JE002513

Warren, J., 1999. Evaporites: their evolution and economics. Wiley-Blackwell.

Welch, R., Limonadi, D., Manning, R., 2013. Systems engineering the Curiosity rover: a retrospective, in: System of Systems Engineering (SoSE), 2013 8th International Conference On. IEEE, pp. 70–75.

Wellington, D.F., Bell, J.F., Johnson, J.R., Kinch, K.M., Rice, M.S., Godber, A., Ehlmann, B.L., Fraeman, A.A., Hardgrove, C., 2017. Visible to near-infrared MSL/Mastcam multispectral imaging: Initial results from select high-interest science targets within Gale Crater, Mars. Am. Mineral. 102, 1202–1217.

Wray, J.J., Squyres, S.W., Roach, L.H., Bishop, J.L., Mustard, J.F., Dobrea, E.Z.N., 2010. Identification of the Ca-sulfate bassanite in Mawrth Vallis, Mars. Icarus 209, 416–421.

Yen, A.S., Morris, R.V., Clark, B.C., Gellert, R., Knudson, A.T., Squyres, S., Mittlefehldt, D.W., Ming, D.W., Arvidson, R., McCoy, T., others, 2008. Hydrothermal processes at Gusev Crater: An evaluation of Paso Robles class soils. J. Geophys. Res. Planets 113.

Zurek, R.W., Smrekar, S.E., 2007. An overview of the Mars Reconnaissance Orbiter (MRO) science mission. J. Geophys. Res. Planets 112.

FIGURES

(Figure number and caption BELOW images)

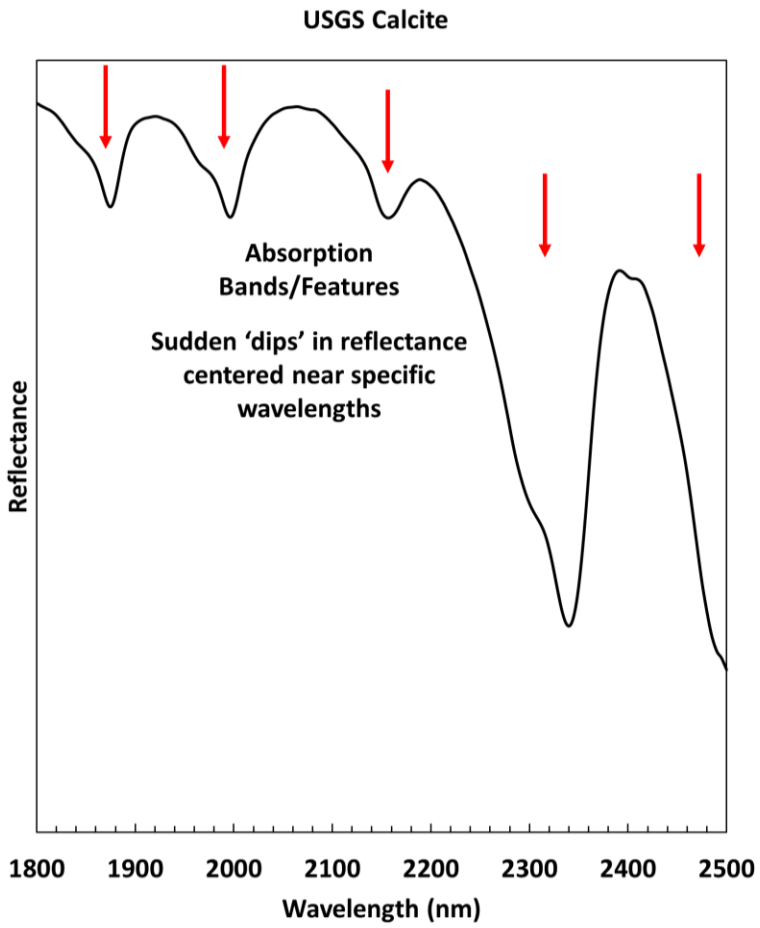

Figure 1: Portion of calcite_gds304.4124 spectrum from the US Geological Survey (USGS) Spectral Library (Kokaly et al., 2017) with locations of major absorption bands labeled. Reflectance has been stretched to increase clarity of absorption bands. Identification of absorption bands is dependent on band position and absolute reflectance values are often redacted in manipulated data.

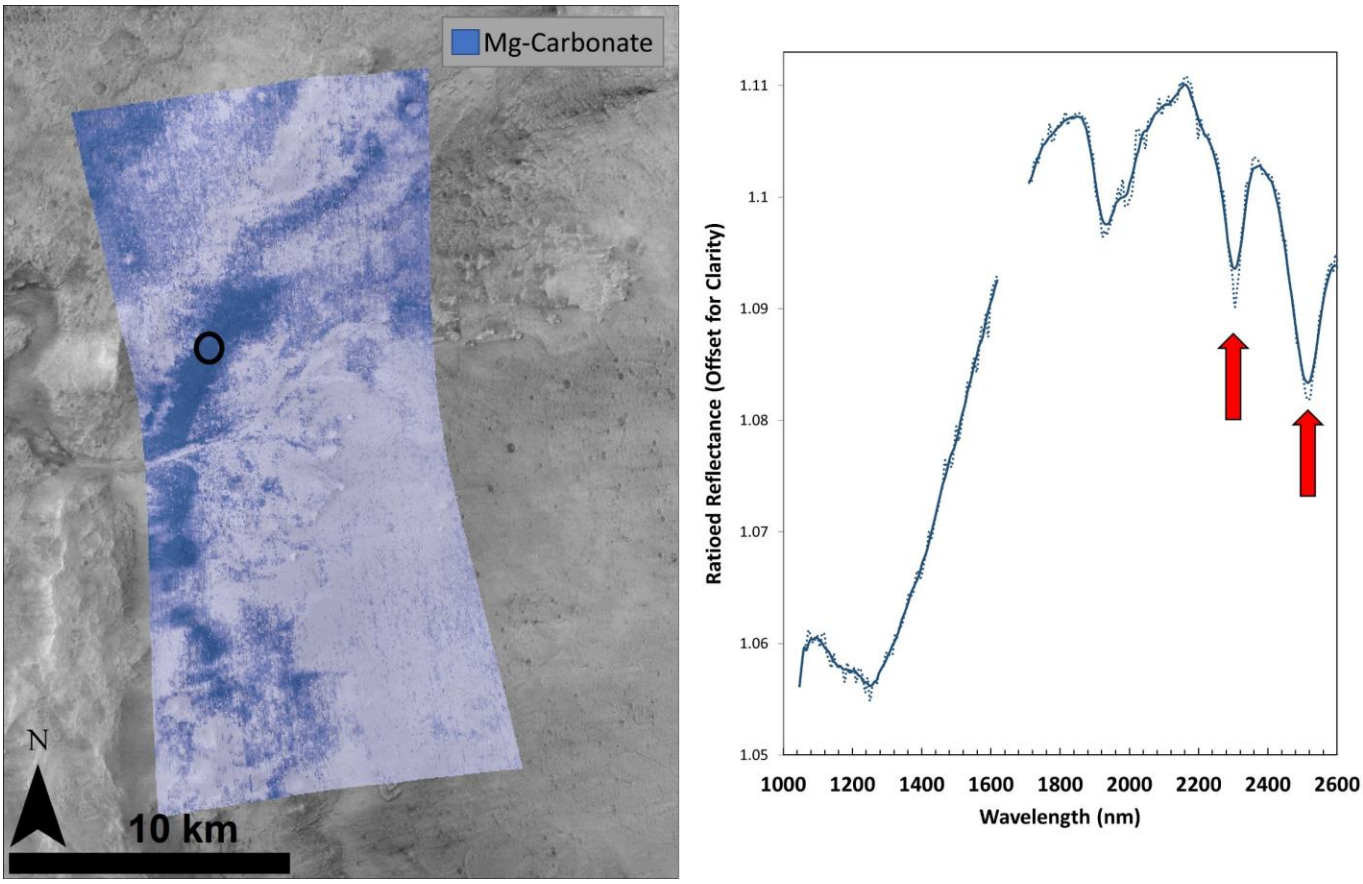

Figure 2: (Left) CRISM spectral parameter MIN2295_2480 applied to CRISM image HRL000040FF from the Jezero Crater region (one of the Mars-2020 candidate landing sites) overlain on Context Camera (CTX; see Section 3.1) image D14_032794_1989. MIN2295_2480 is a CRISM spectral parameter sensitive to absorptions at 2295 nm and 2480 nm to constrain the presence of the ~2300 nm and ~2500 nm absorption bands in Mg-sulfates (Viviano-Beck, 2014). (Right) CRISM SWIR spectrum acquired from pixels within the black oval in the spectral parameter map. Dotted line is the original CRISM spectrum. Solid line is the spectrum after being smoothed by a 7-pixel boxcar average. Significant noise in the 1600-1700 nm region has been removed. The spectrum features prominent absorptions near ~2300 nm and ~2500 nm related to carbonates. Given presence of these absorption bands in terrain highlighted by the CRISM parameter for Mg-carbonates, dark blue terrains in the parameter map are likely Mg-carbonate-bearing.

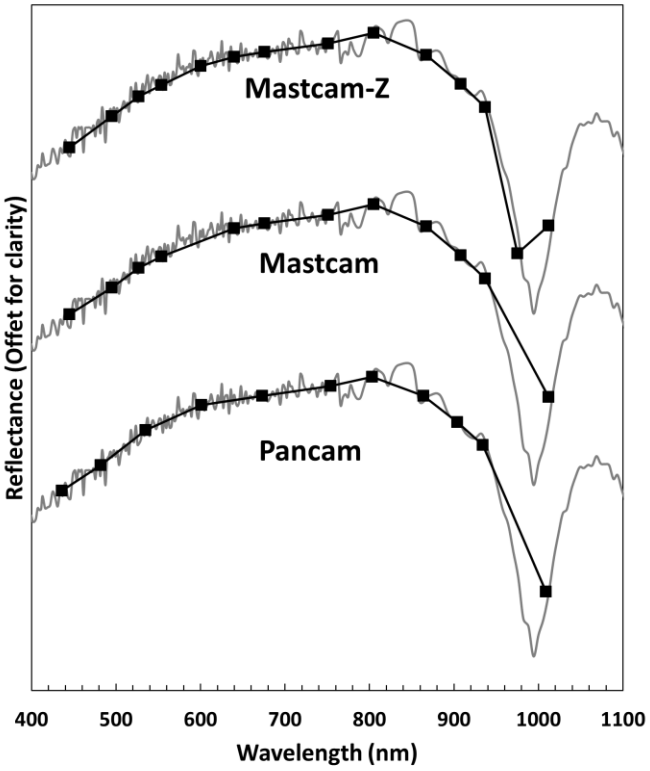

Figure 3: Pancam, Mastcam, and Mastcam-Z convolved spectra of USGS gypsum_su2202.8850 (Kokaly et al., 2017). Grey lines are original laboratory resolution spectra, black lines are convolved spectra. Black squares correspond to instrument filter positions. Plots have been vertically offset to eliminate overlap, improving visual clarity. The ~975nm filter on Mastcam-Z improves resolution in the 950-1000 nm region where hydration bands may occur.

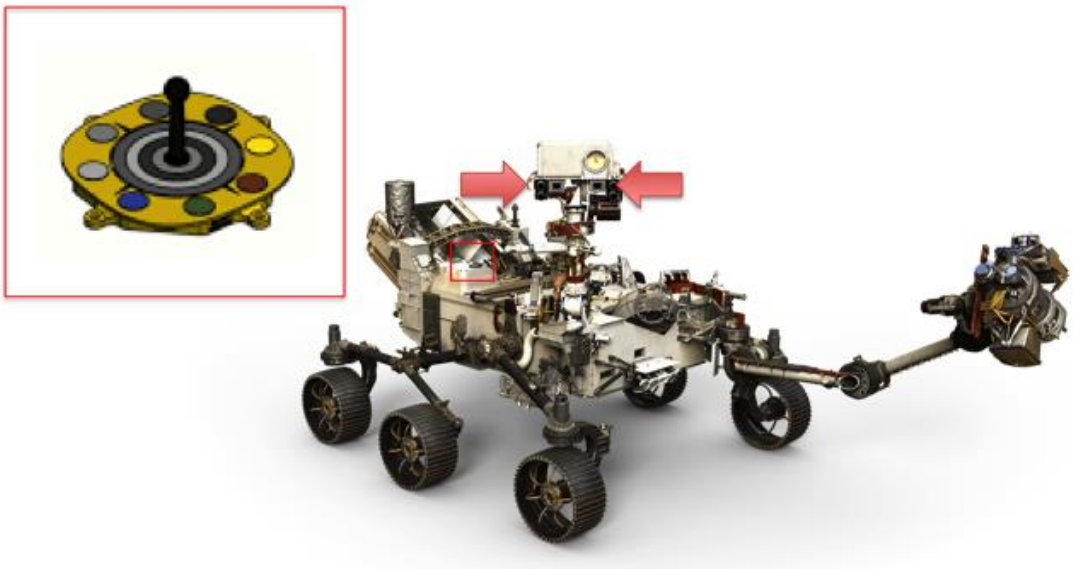

Figure 4: High-definition illustration of the Mars-2020 rover. Location of the dual Mastcam-Z cameras indicated by red arrows and Mastcam-Z calibration target and zoomed schematic located in red inset box.

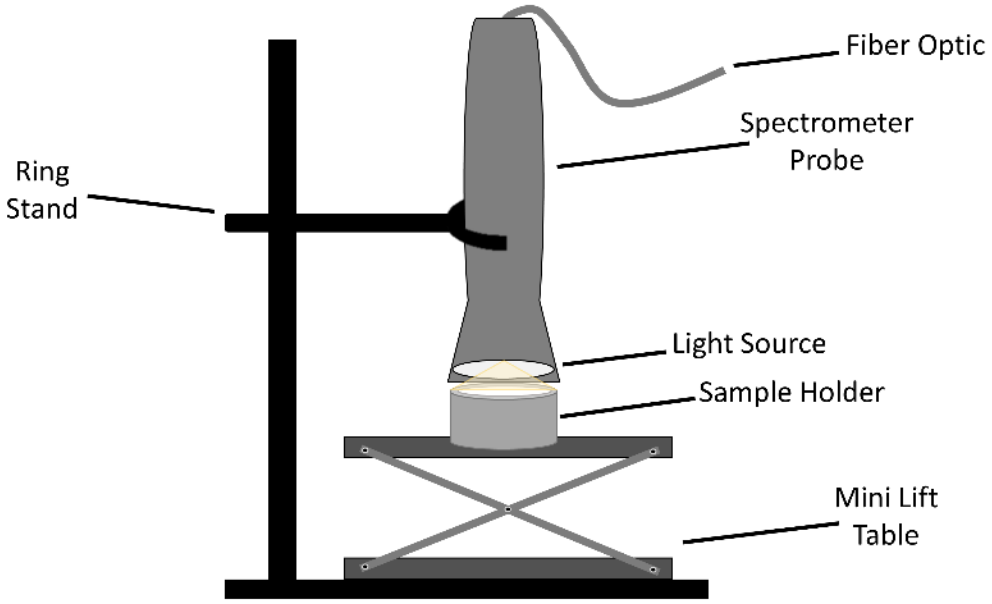

Figure 5: Cartoon showing the ring stand-spectrometer probe apparatus used for data collection. The spectrometer probe was mounted facing downward on a ring stand clamp and brought into contact with the raised sample holder.

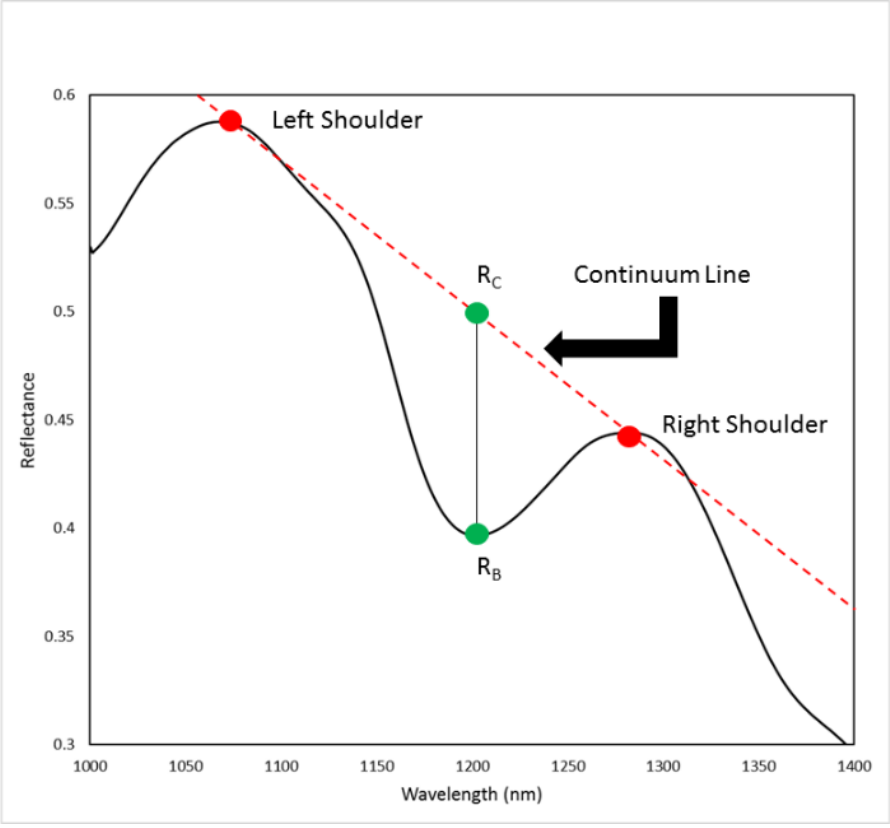

Figure 6: Illustration of the band depth calculation process for a hypothetical band. Left and right shoulder values must be chosen at locations above the band center on the analyzed spectrum. Band depth calculates the percent drop of the measured spectrum at band center below the reflectance of the continuum line at band center. R_C is the reflectance of the continuum line at the center wavelength of the band. R_B is the reflectance of the spectrum at the center wavelength of the band.

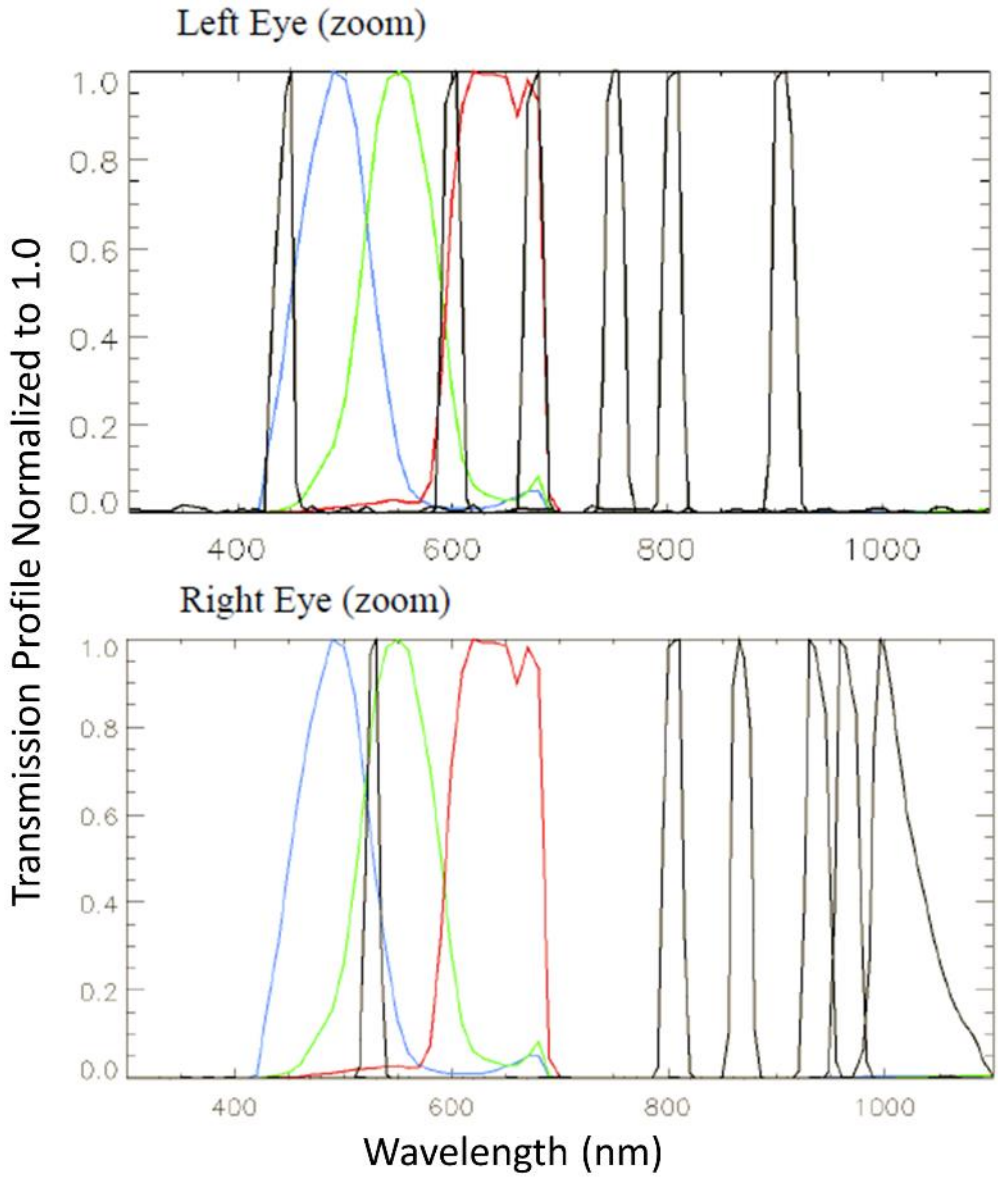

Figure 7: Hypothetical transmission profiles for the left and right eyes of Mastcam-Z. X-axis is wavelength in nanometers and Y-axis is transmission strength.

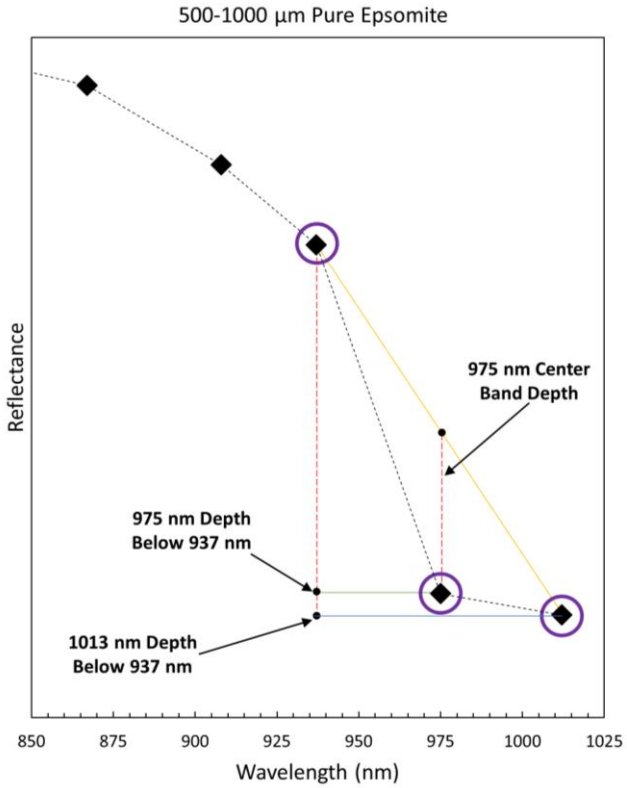

Figure 8: Diagram showing what each calculated band depth represents. The dashed black line is the Mastcam-Z resolution spectrum. Black diamonds are the Mastcam-Z filter positions. Dashed red lines represent band depths (the calculated decreases in reflectance). The solid yellow line is the continuum line between 937 nm and 1013 nm. The solid green and blue lines are the points at which the 937-975 band depth and the 1013-depth-below-975 are calculated.

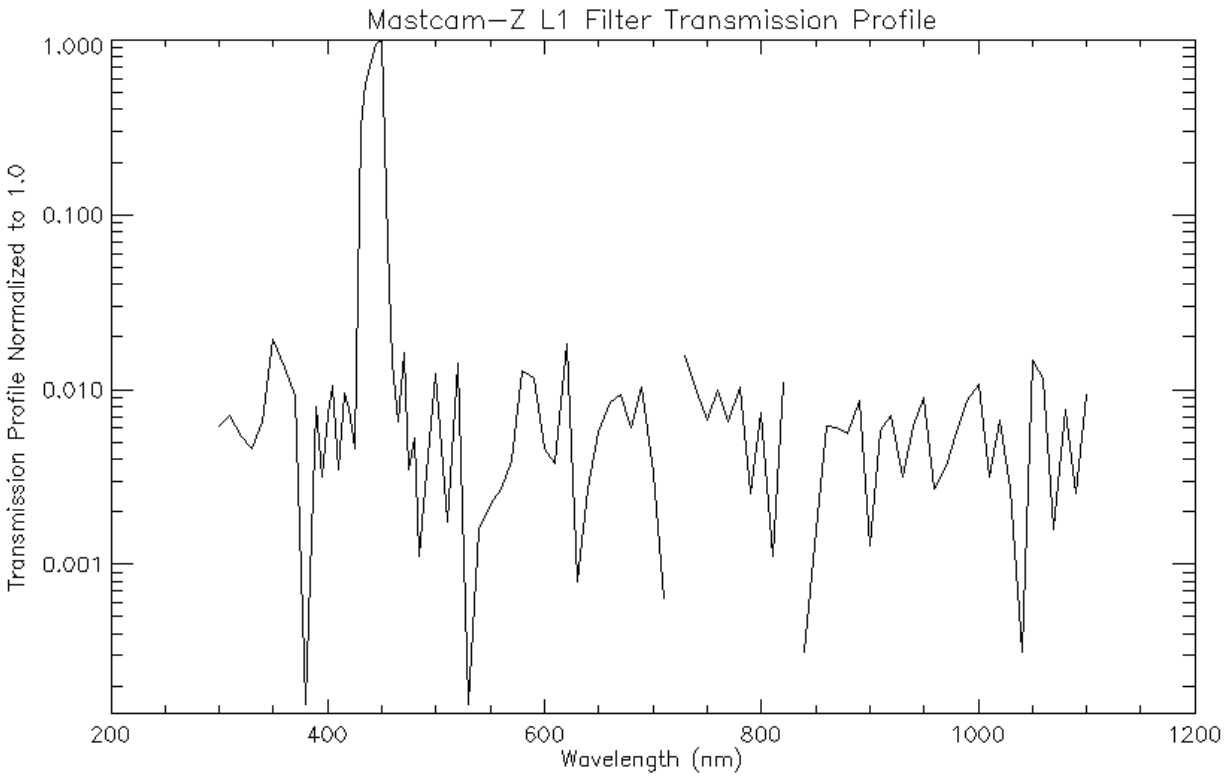

Figure 9: Hypothetical transmission profile for the 445 nm filter. The 445 nm bandpass in the left eye includes some light sensitivity at all wavelengths. These small windows of additional light sensitivity are not ideal and allow noise into images taken using this filter.

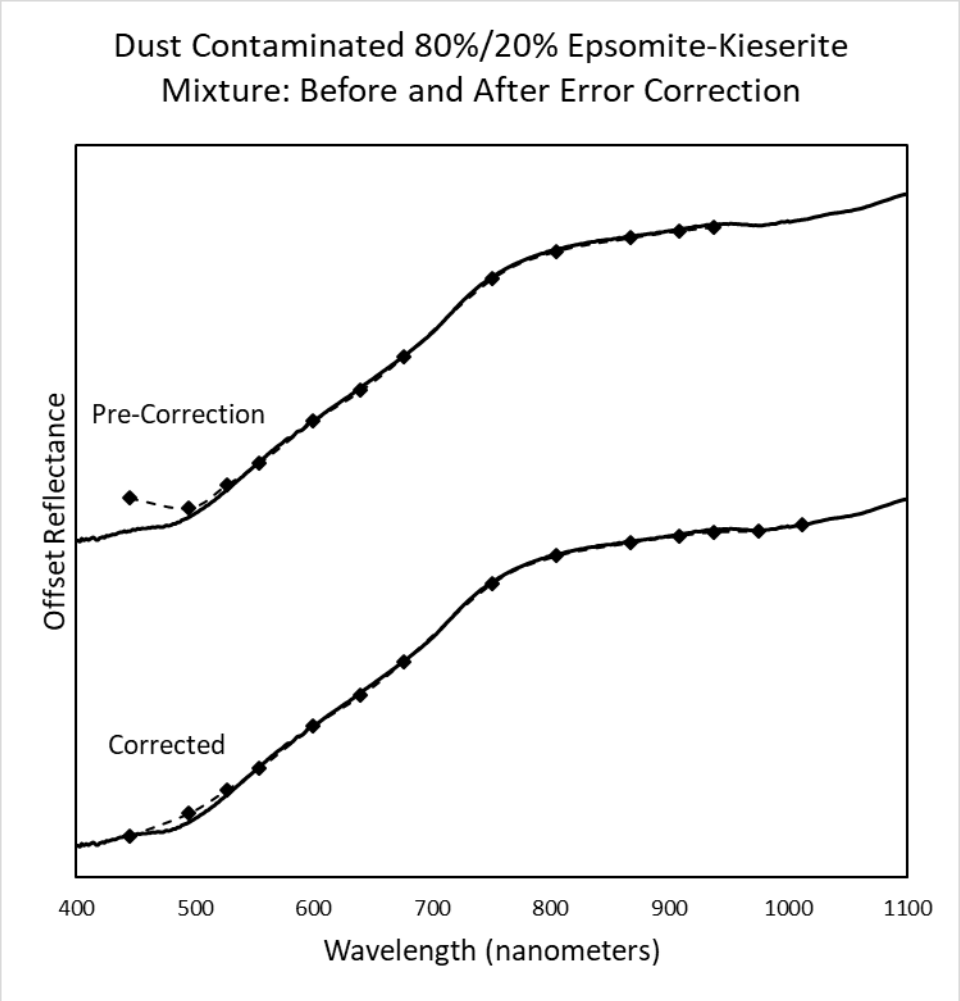

Figure 10: Spectrum for the dust contaminated 80% epsomite, 20% kieserite mixture before and after correction of the 445nm band position. Dashed line is the Mastcam-Z convolved spectrum, solid line is the laboratory spectrum.

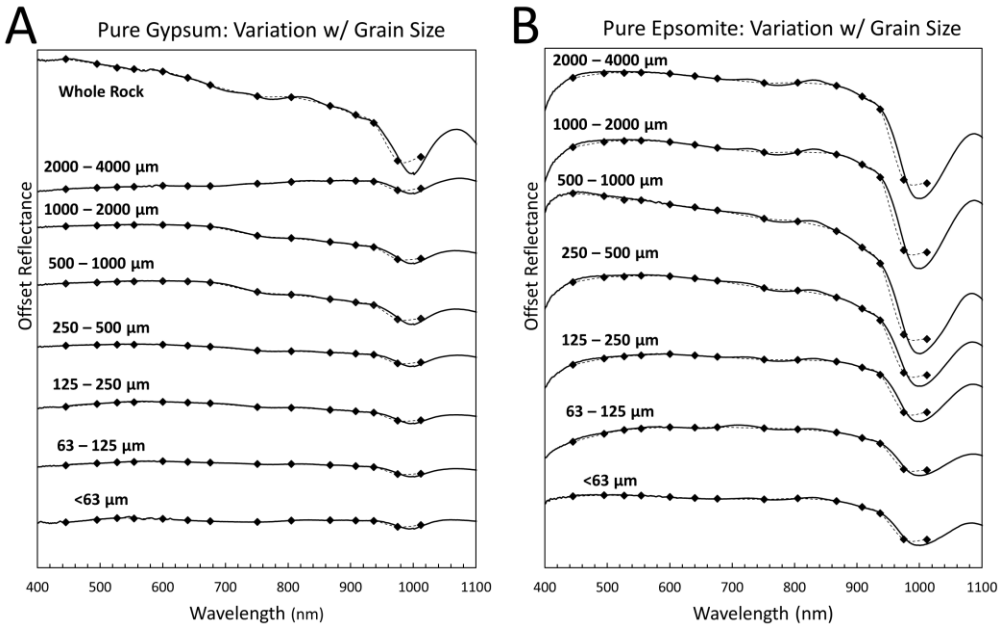

Figure 11: A – Pure gypsum spectra for different grain size fractions. B – Pure epsomite spectra for different grain size fractions. Dashed line is the Mastcam-Z convolved spectrum, solid line is the laboratory spectrum. Absolute reflectance values have been offset by an arbitrary amount to separate curves and improve figure clarity.

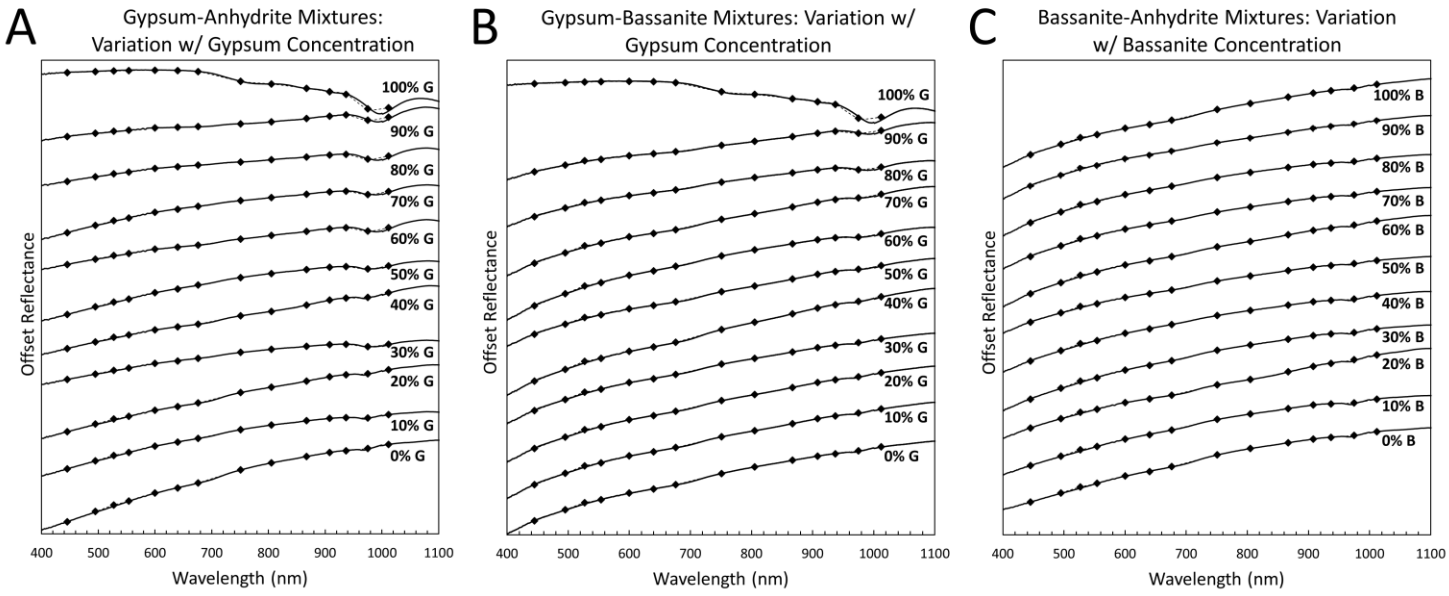

Figure 12: A – Gypsum-anhydrite mixture spectra. B – Gypsum-Bassanite mixture spectra. C – Bassanite-Anhydrite mixture spectra. Dashed line is the Mastcam-Z convolved spectrum, solid line is the laboratory spectrum. Absolute reflectance values have been offset by an arbitrary amount to separate curves and improve figure clarity.

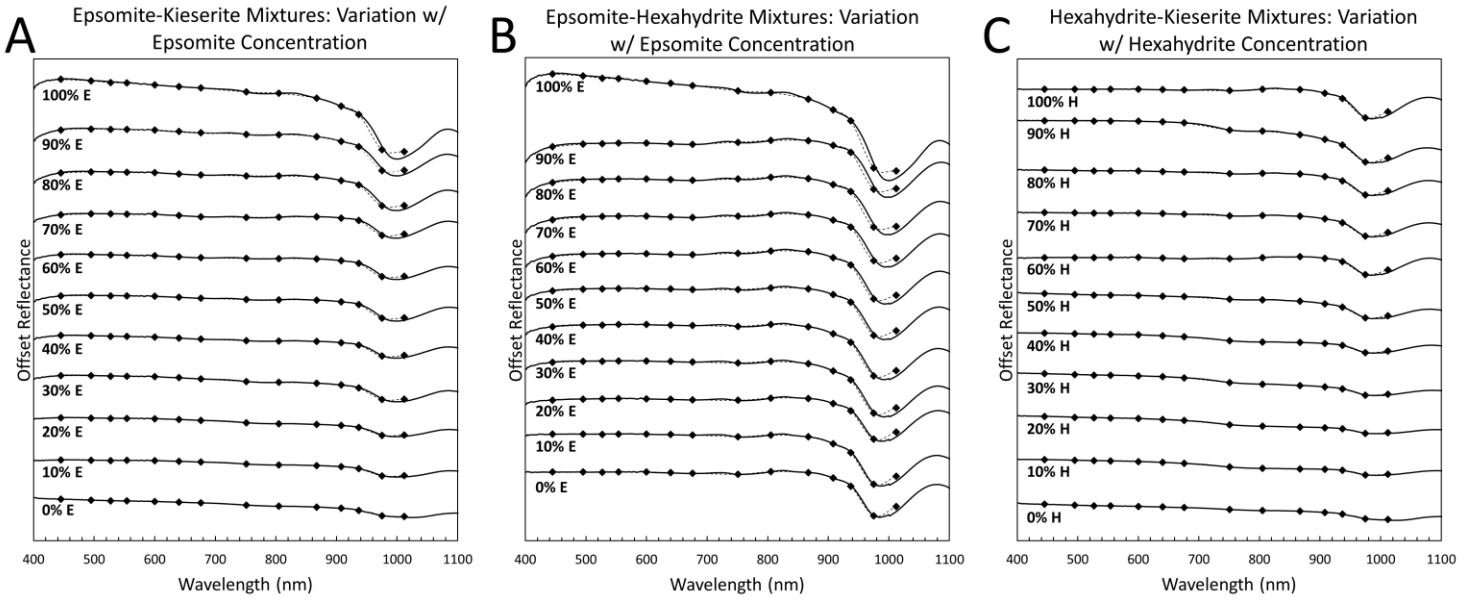

Figure 13: A – Epsomite-Kieserite mixture spectra. B – Epsomite-Hexahydrite mixture spectra. C – Hexahydrite-Kieserite mixture spectra. Concentration of more hydrated phase increases in 10% increments from top to bottom. Dashed line is the Mastcam-Z convolved spectrum, solid line is the laboratory spectrum. Absolute reflectance values have been offset by an arbitrary amount to separate curves and improve figure clarity.

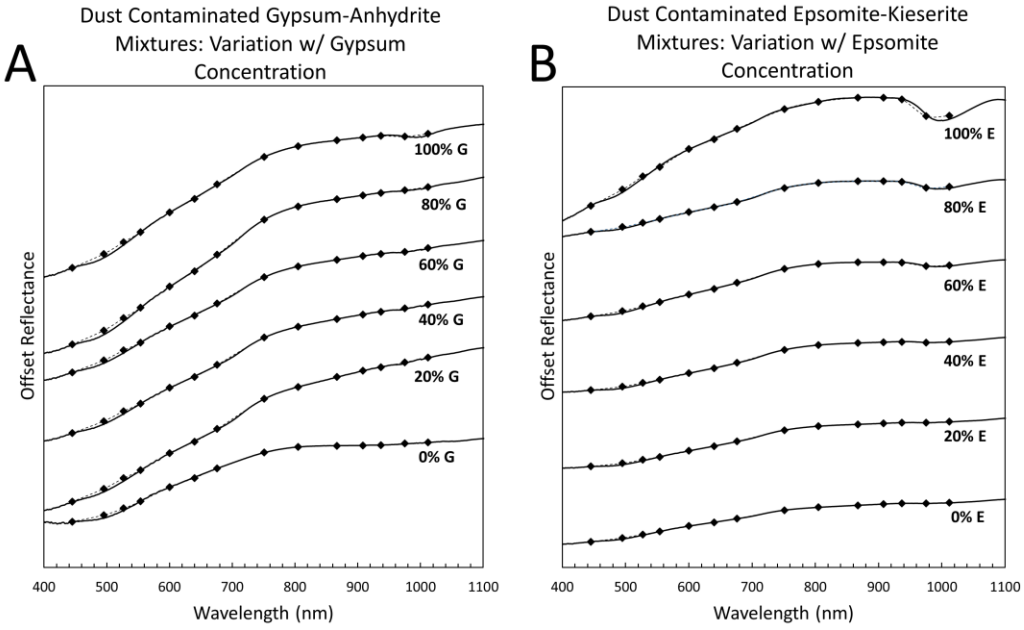

Figure 14: A – Dust contaminated Gypsum-Anhydrite mixture spectra. B – Dust contaminated Epsomite-Kieserite mixture spectra. Concentration of more hydrated phase increases in 20% increments from top to bottom. Dashed line is the Mastcam-Z convolved spectrum, solid line is the laboratory spectrum. Vertical offset has been applied to each spectrum for plot clarity. Reflectance values are not listed; vertically offset reflectance values are not real.

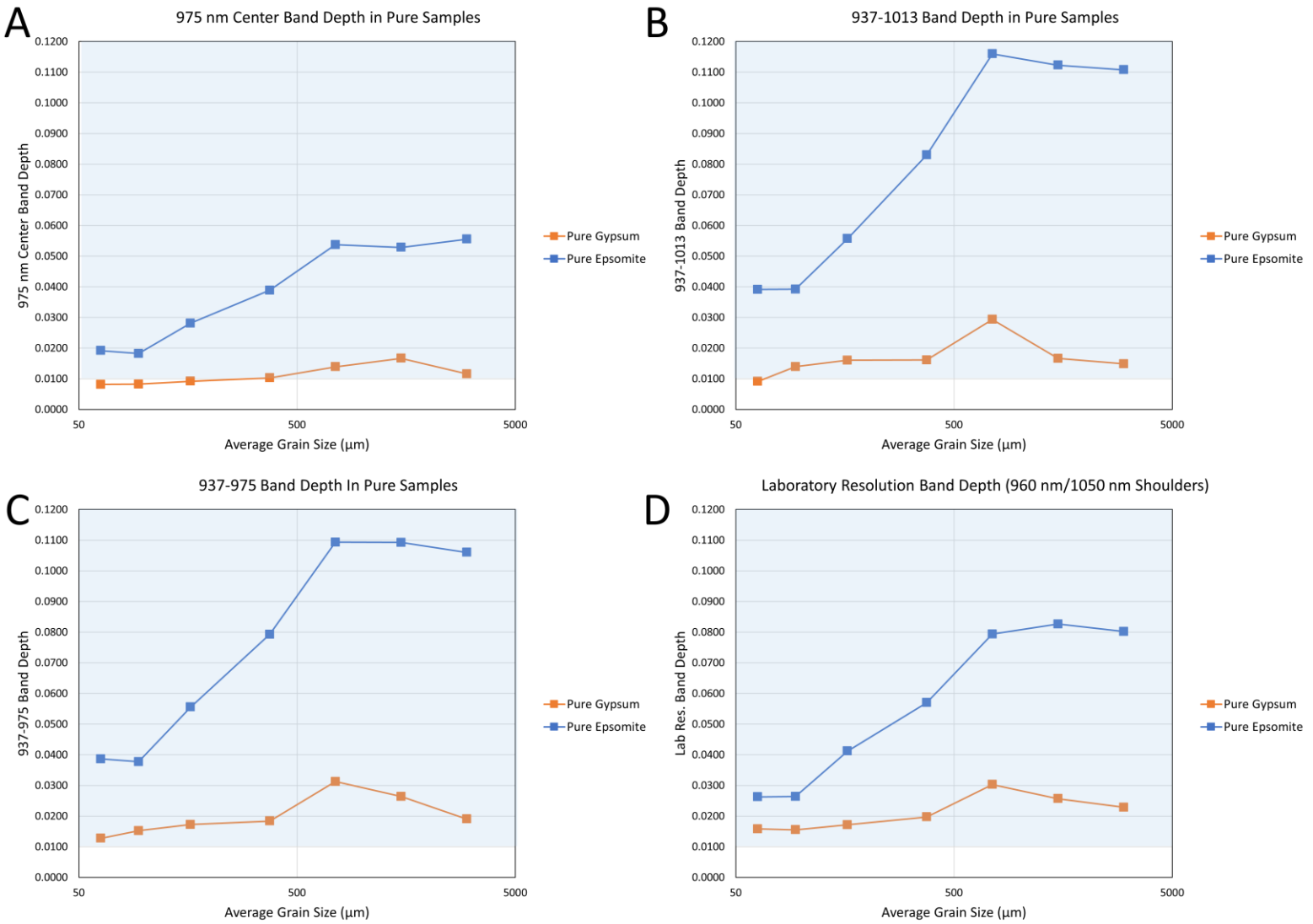

Figure 15: A – 975 nm Center Band Depth for pure epsomite and gypsum samples. B – 937-1013 band depth for pure epsomite and gypsum samples. C - 937-975 band depth for pure epsomite and gypsum samples. D - Lab Resolution Band Depth (960 nm and 1050 nm as shoulder positions) in pure epsomite and gypsum samples. Blue shaded region indicates a band that is detectable to Mastcam-Z.

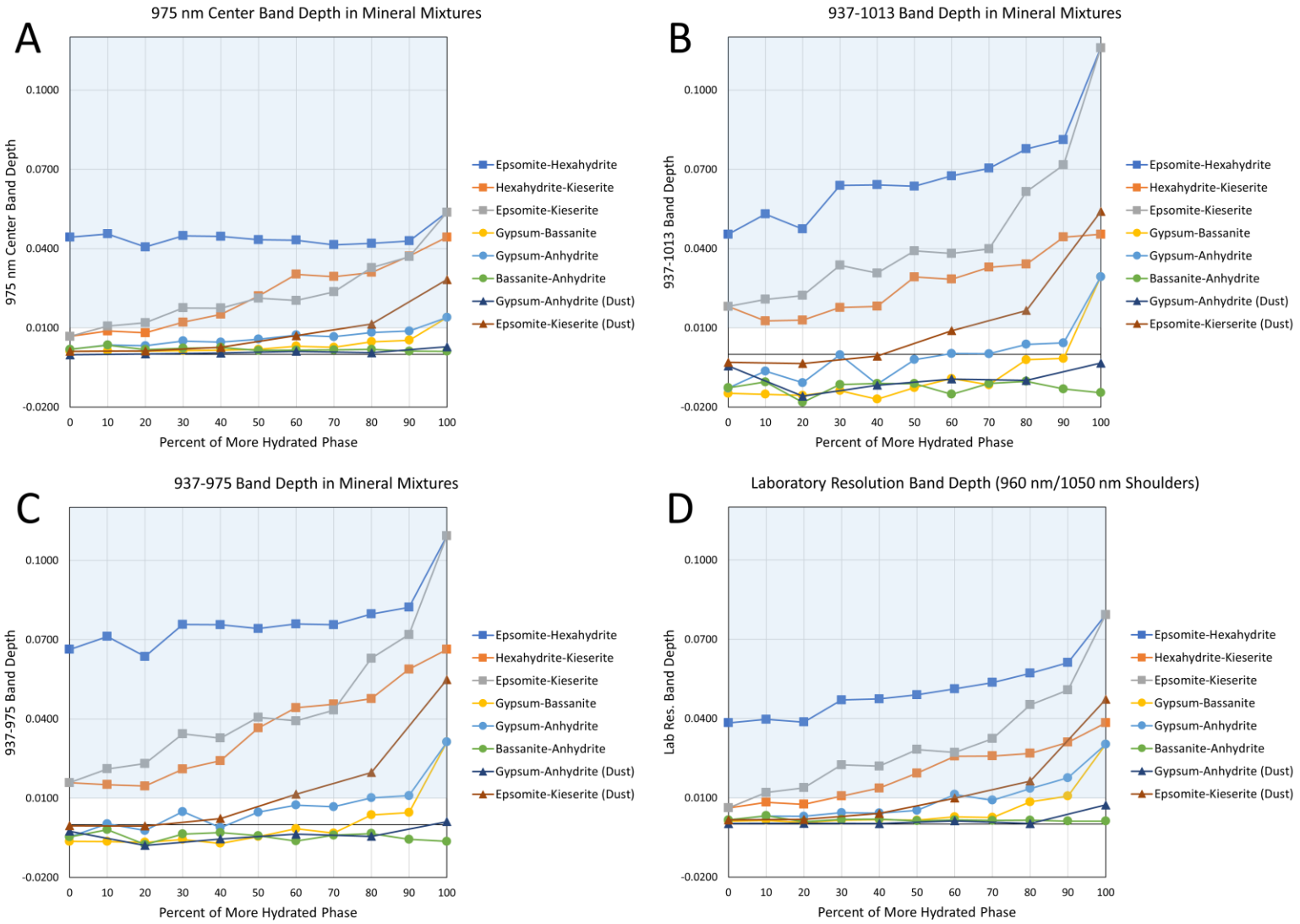

Figure 16: A – 975 nm Center Band Depth for all mixtures. B – 937-1013 band depth for all mixtures. C - 937-975 band depth for all mixtures. D - Lab Resolution Band Depth for all mixtures. Blue shaded region indicates a band that is detectable to Mastcam-Z. Epsomite-Hexahydrite/Epsomite Kieserite and Gypsum-Bassanite/Gypsum-Anhydrite have the same values at 100% of the more hydrated phase. Hexahydrite-Kieserite/Epsomite-Kieserite and Gypsum-Anhydrite/Bassanite-Anhydrite have the same values at 0% of the more hydrated phase.

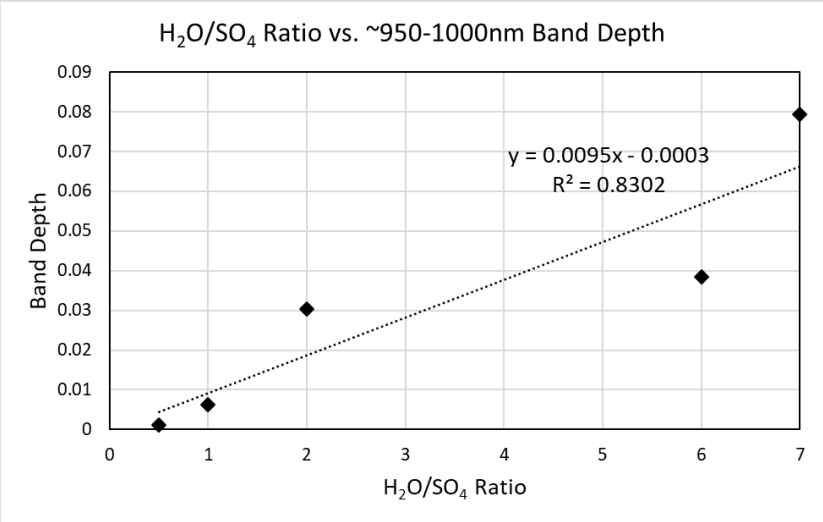

Figure 17: Change in band depth with H_2O/SO_4 ratio for pure 500-1000 µm hydrated Ca/Mg-sulfates with linear trendline. Depth of the ~950-1000 nm absorption band is noted to depend significantly on amount of bound water.

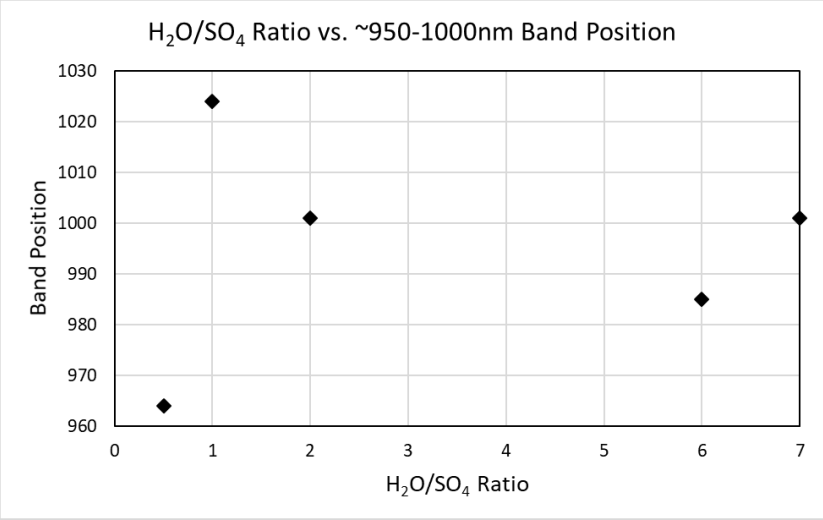

Figure 18: Change in band position with H_2O/SO_4 ratio for pure 500-1000 µm hydrated sulfates. Position of the ~950-1000 nm absorption band does not exhibit a dependence on amount of bound water.

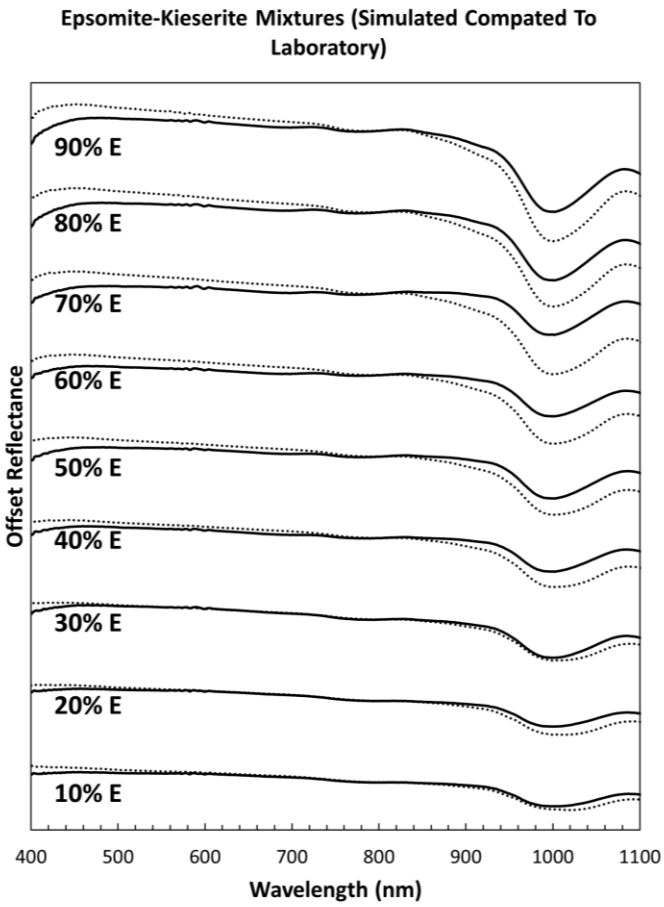

Figure 19: Reflectance spectra of epsomite-kieserite mixtures. Solid lines are laboratory spectra, dotted lines are linear mixing model versions of laboratory counterparts.

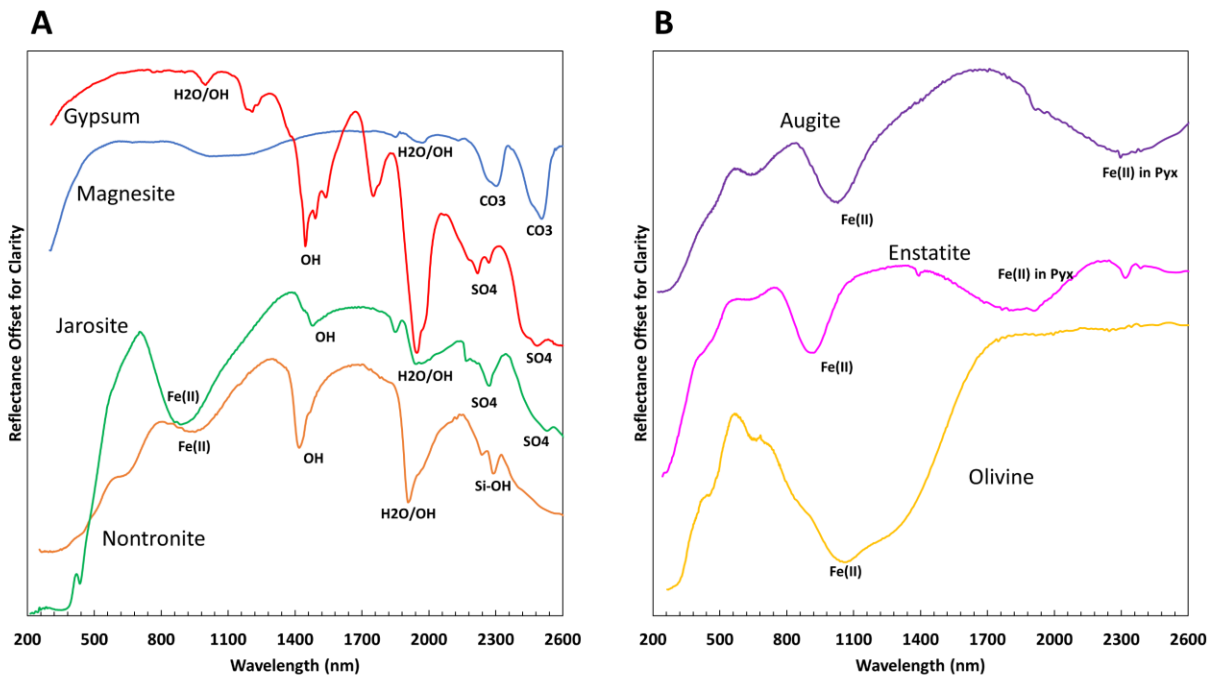

Figure 20: Example spectra of Mars-relevant mineral species. A: alteration mineral species. B: mafic mineral species. Olivine, augite, jarosite, enstatite, and nontronite spectra come from the USGS Spectral Library and the magnesite and gypsum spectra come from RELAB. Reflectance has been offset for visual clarity. Spectra may have been acquired at different times with varying instruments and lab setups which effects the relative depth of absorption bands; it should not be assumed from this figure that any mineral possess inherently deeper absorption bands than another.

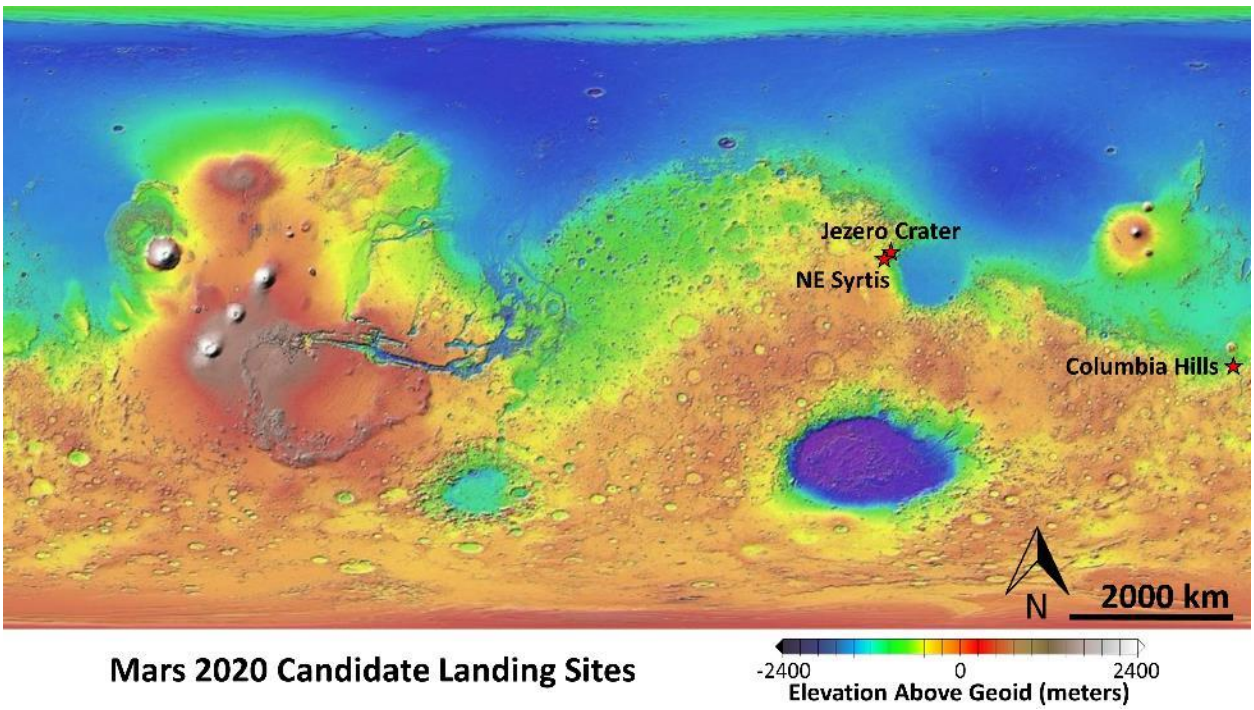

Figure 21: Mars MOLA (Mars Orbiter Laser Altimeter) global map showing the locations of the 3 candidate landing sites for Mars 2020.

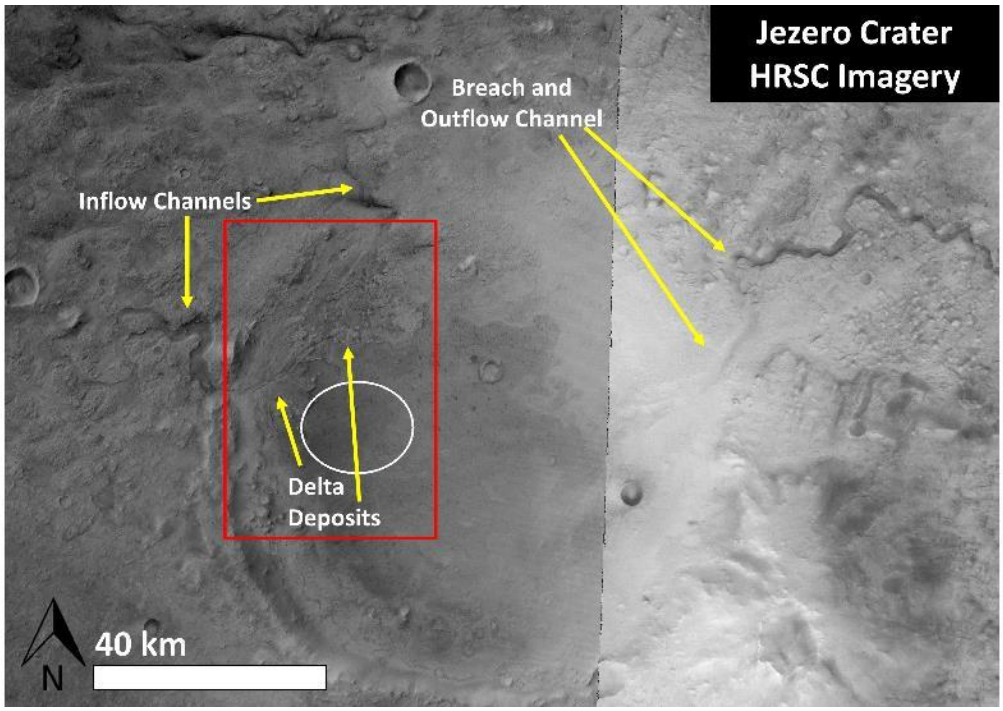

Figure 22: HRSC images H0988_0000 and H2228_0002 of Jezero crater showing the Mars 2020 landing ellipse (white oval), delta deposits, and inflow/outflow channels. The red rectangle outlines the study area investigated by this work.

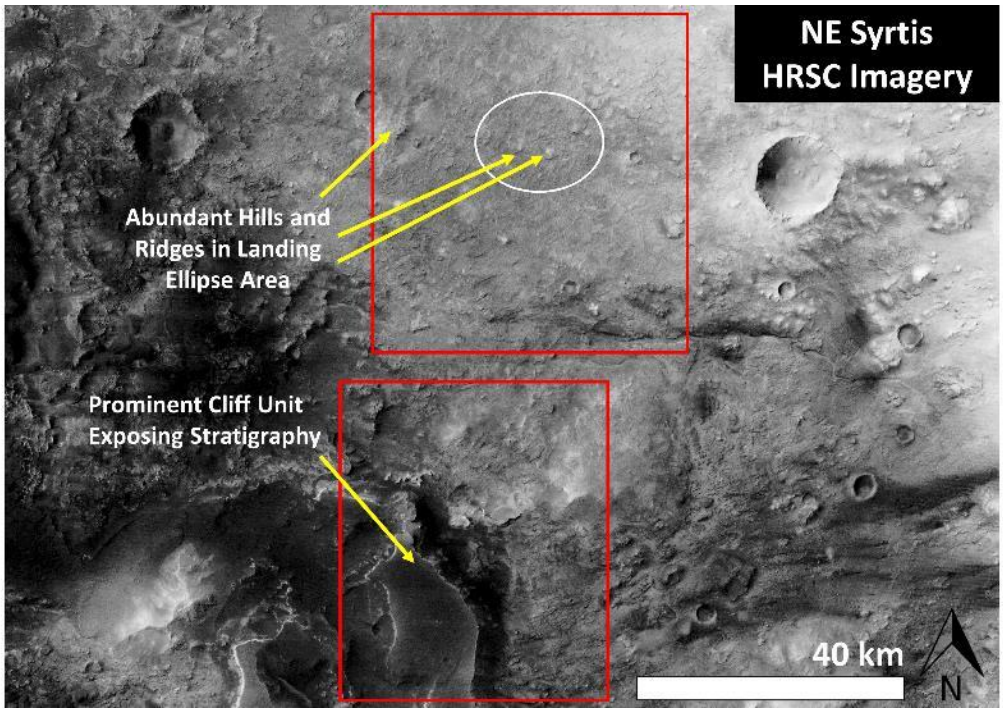

Figure 23: HRSC image H0988_0000_ND3 of the NE Syrtis region showing the Mars 2020 landing ellipse (white ellipse) and prominent geologic features. Red rectangles outline the study areas investigated by this work.

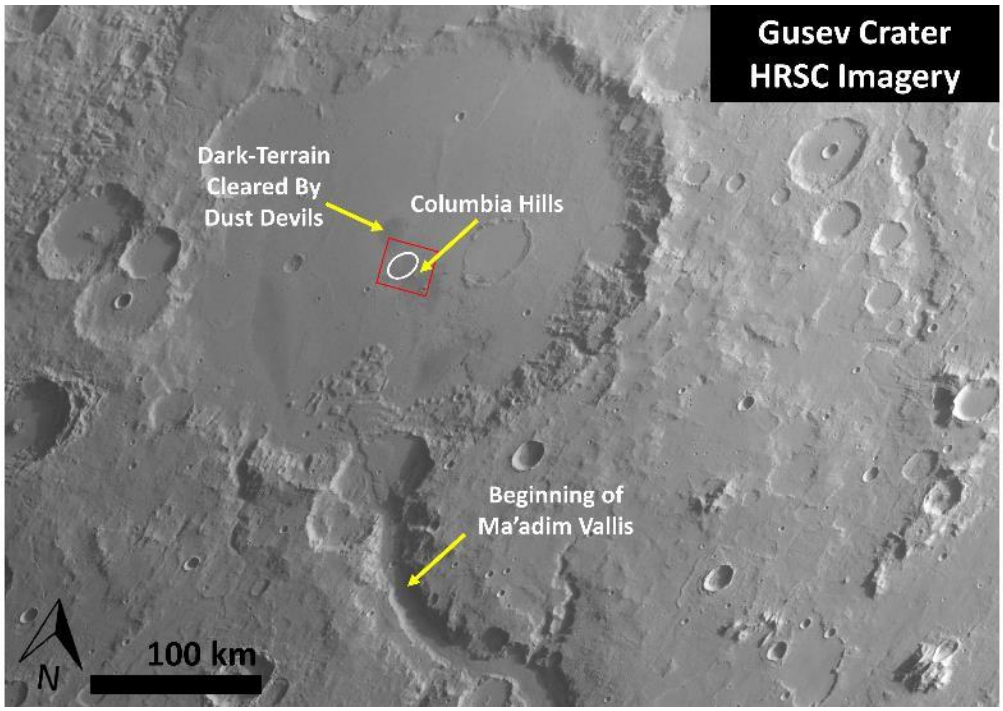

Figure 24: HRSC image H0637_0000_ND3 of Gusev crater showing the Mars 2020 landing ellipse (white oval), the location of the Columbia Hills site, the dark terraub immediately surrounding the Columbia Hills, and the beginning of the Ma'adim Vallis channel. The red rectangle outlines the study area investigated by this work.

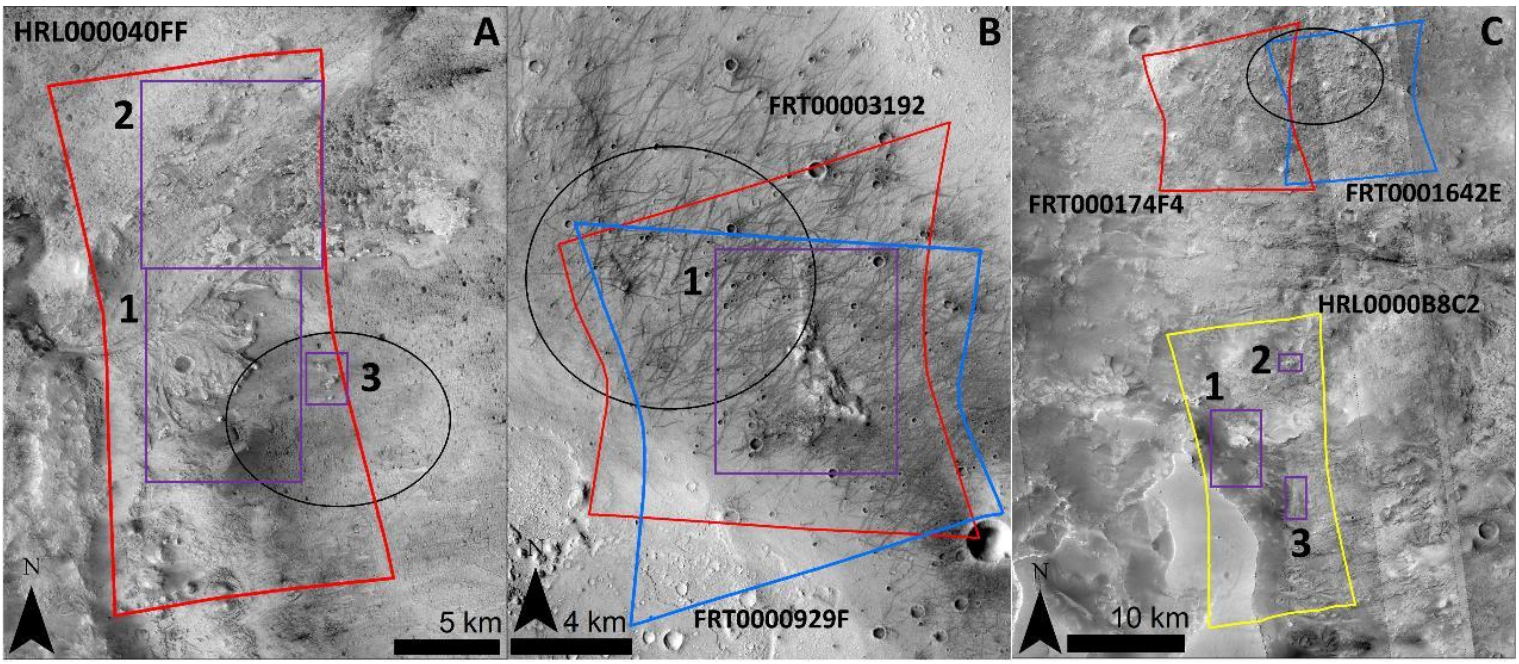

Figure 25: From left to right, CRISM observation outlines and landing ellipses on CTX imagery at Jezero Crater (image D14_032794_1989), Columbia Hills (image D06_029415_1653), and NE Syrtis (images B18_016720_1978, B_19_016931_1975, F05_037818_1977, and P06_003376_1987). Red/blue/yellow outlines are full extents of CRISM observations used in this study, black ovals are outlines of the preliminary landing ellipses as defined by the Mars-2020 engineering team. Purple boxes indicate regions of interest that will be spectrally examined in detail. Regions of interest for each site are numbered. CRISM observation

IDs are included next to observation outlines. It is customary to remove the zeroes in CRISM IDs; going forward, IDs will be presented in an FRTXXXX format.

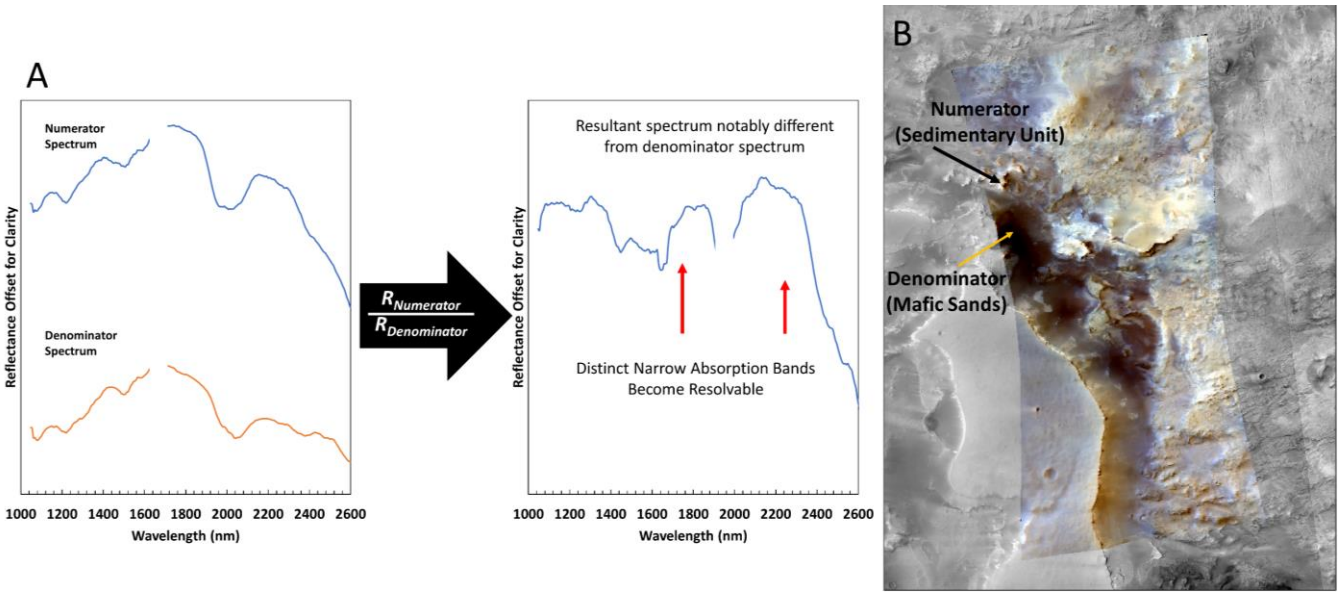

Figure 26: (A) Blue numerator spectrum from a sedimentary region in NE Syrtis was divided by the orange denominator spectrum from nearby mafic sand dunes to remove spectral similarities between the two units and isolate spectral properties unique to the sedimentary unit. This process revealed distinct narrow absorption bands near 1400 nm and 1900 nm. (B) CRISM RGB imagery overlain on CTX images B18_016720_1978 and B_19_016931_1975 of NE Syrtis showing location of numerator and denominator spectra.

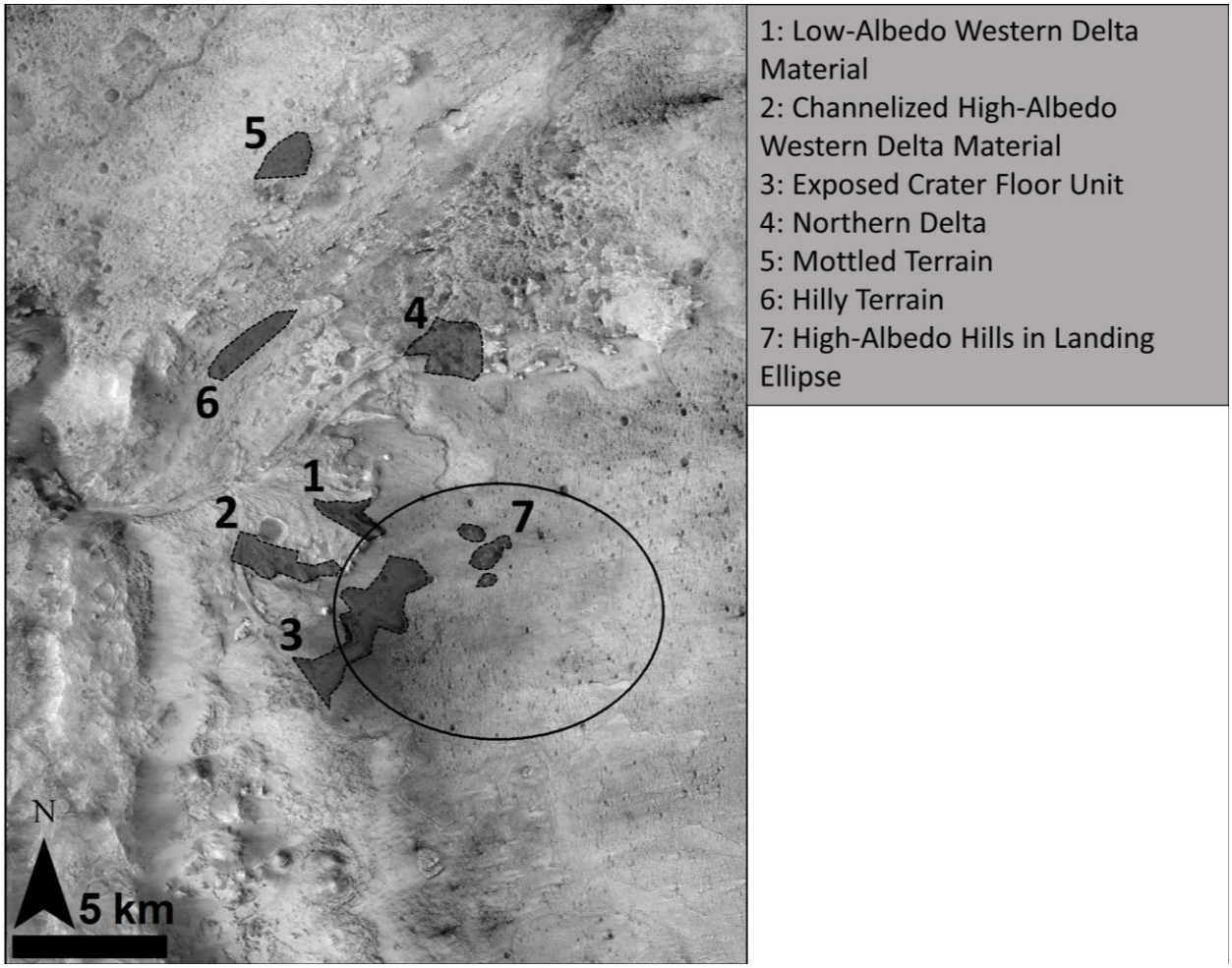

Figure 27: CTX image D14_032794_1989 of the Jezero Crater region showing geologic units of interest that were chosen for spectral extraction. Black oval is the proposed Mars 2020 landing ellipse. These units will be discussed in this section's results.

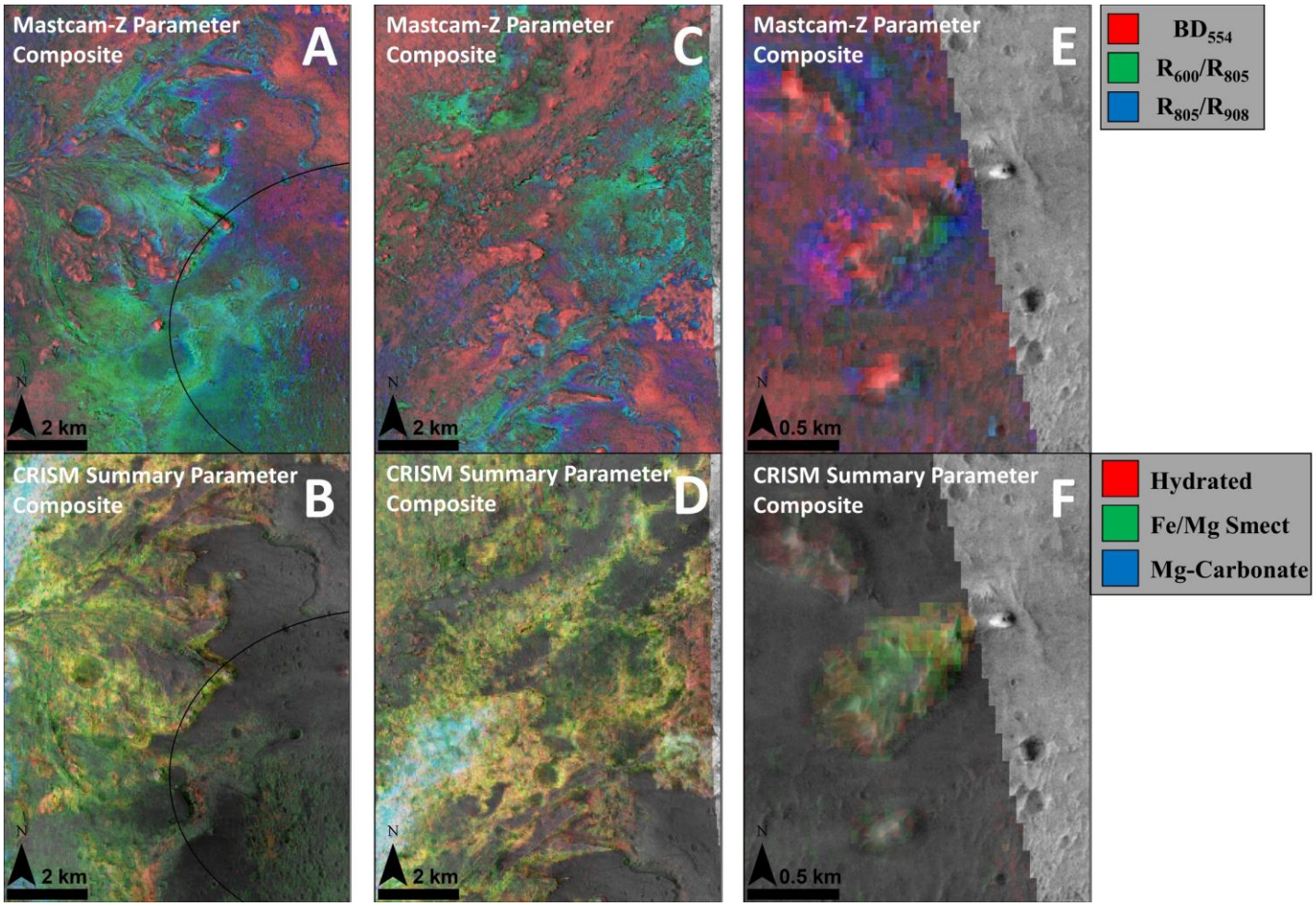

Figure 28: (A) Mastcam-Z parameter composite for Jezero region of interest #1. Black partial-oval is the proposed landing ellipse. (B) CRISM SWIR summary parameter composite for Jezero region of interest #1. Black partial-oval is the proposed landing ellipse. (C) Mastcam-Z parameter composite for Jezero region of interest #2. (D) CRISM SWIR summary parameter composite for Jezero region of interest #2. (E) Mastcam-Z parameter composite for Jezero region of interest #3. (F) CRISM SWIR summary parameter composite for Jezero region of interest #3. All parameters are overlain on CTX image D14_032794_1989.

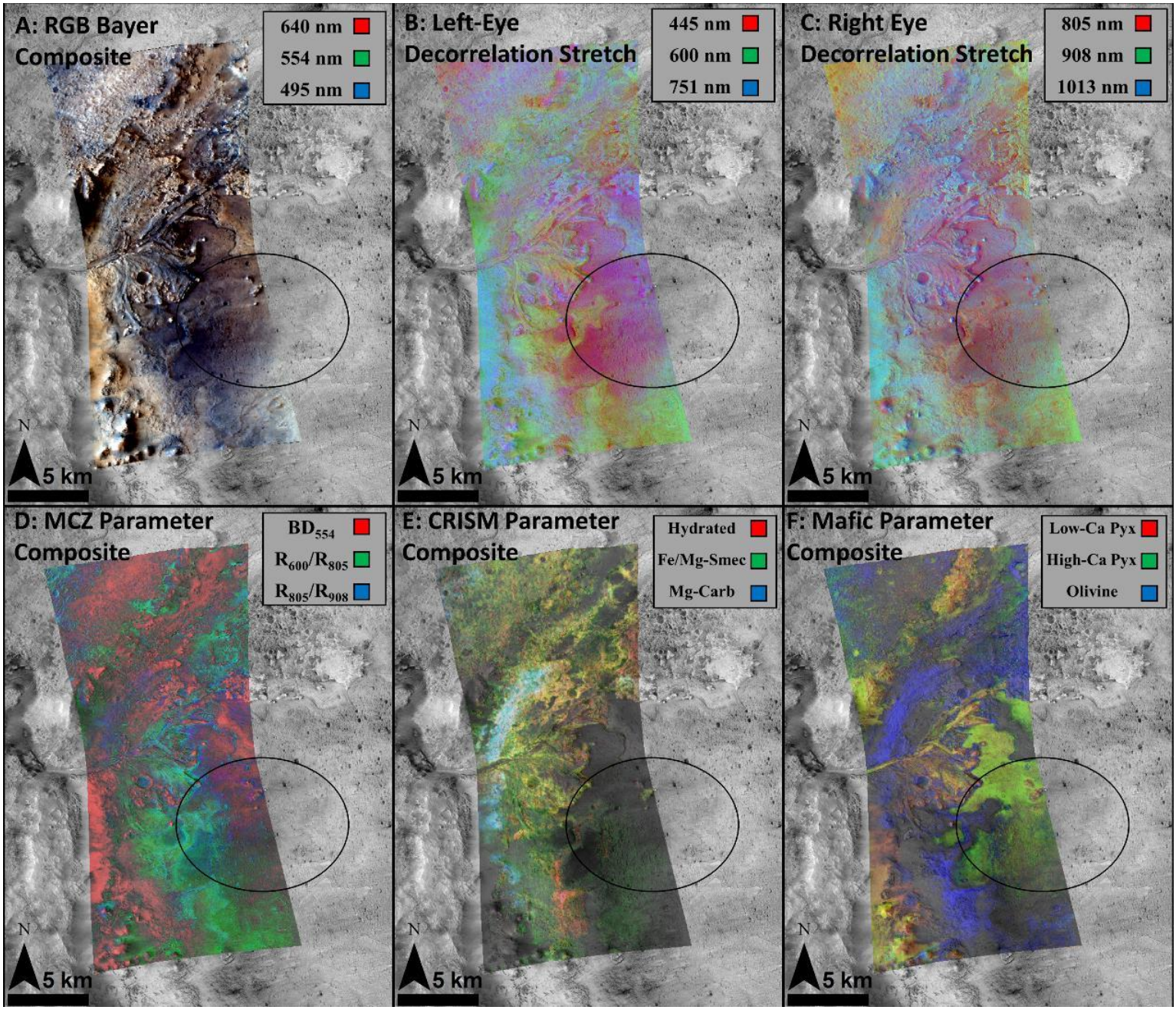

Figure 29: (A) Mastcam-Z RGB Bayer filter composite to simulate Mastcam-Z real-color imagery. (B) Left eye decorrelation stretch. (C) Right eye decorrelation stretch. (D) Mastcam-Z parameter composite. (E) CRISM SWIR summary parameter map for alteration mineralogy. (F) CRISM SWIR summary parameter map for mafic mineralogy. All parameters are overlain on CTX image D14_032794_1989. Black ovals are the proposed Mars-2020 landing ellipse

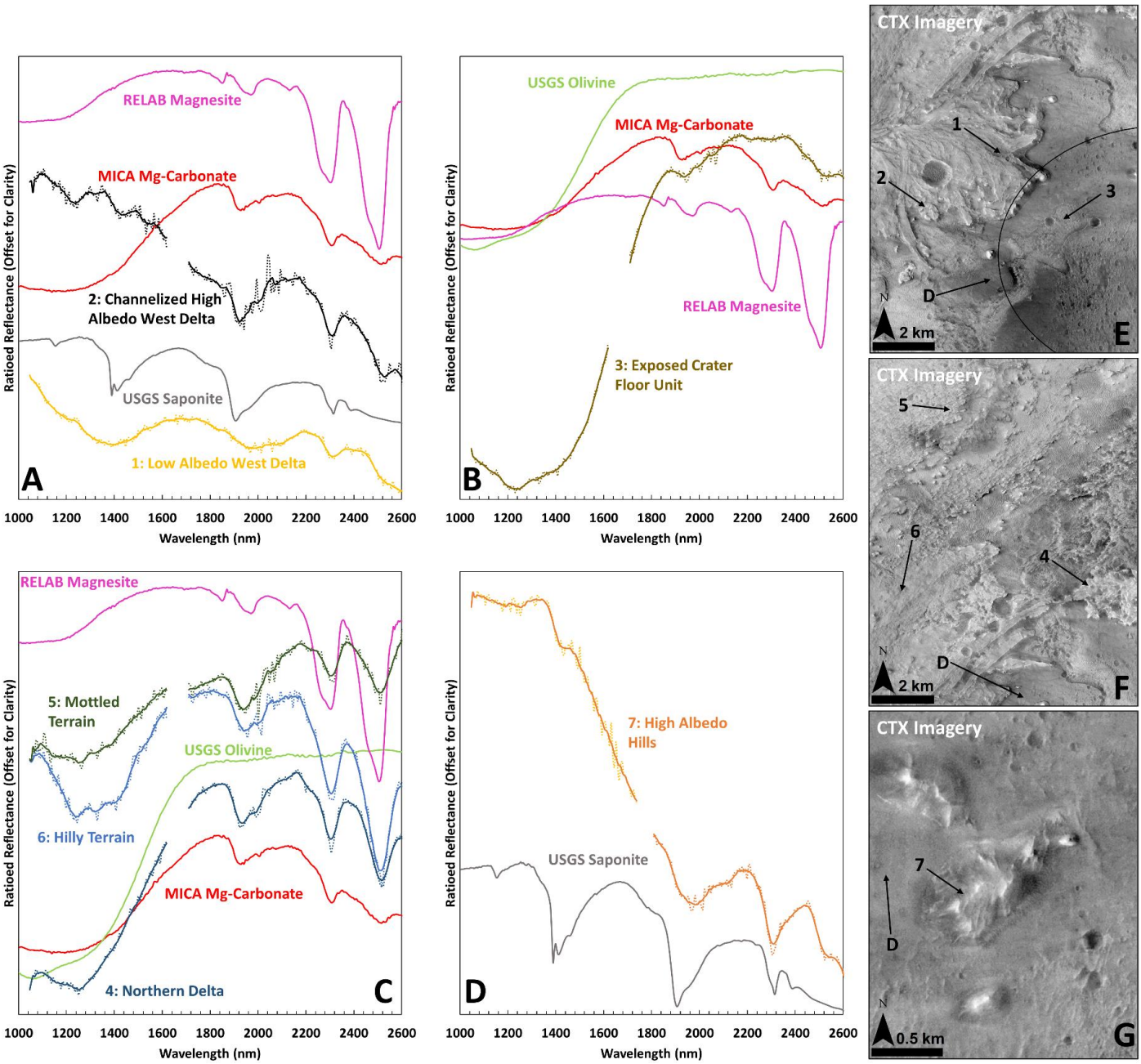

Figure 30: CRISM SWIR spectra for selected geographic areas in and around the proposed Jezero Crater landing zone and laboratory spectra from known spectral databases for comparison. Numbered spectra are extracted from CRISM imagery, non-numbered spectra are laboratory spectra. (A) Spectra from the western delta. (B) Spectra from the exposed crater floor unit. (C) Spectra from rocks north of the western delta. (D) Spectra from the high-albedo hills in the landing ellipse. Dashed lines are spectra prior to 7-pixel boxcar averaged, solid lines are boxcar averaged spectra. Absolute reflectance values are not included; reflectance is ratioed and offset for clarity and no longer pertains to real values. E-G: CTX image D14_032794_1989 of Jezero Crater regions of interest illustrating regions spectra were extracted. Numbered labels are numerator spectra; D is denominator spectrum. Comparison spectra are from the USGS, RELAB, and MICA databases (Pieters and Hiroi, 2004; Viviano-Beck et al., 2014; Kokaly et al., 2017) and their respective sample IDs are olivine_gds70.16284 (USGS olivine), saponite_sapca1.19977 (USGS saponite), CRB114 (HOSERLab ID for RELAB magnesite). MICA samples do not have sample IDs.

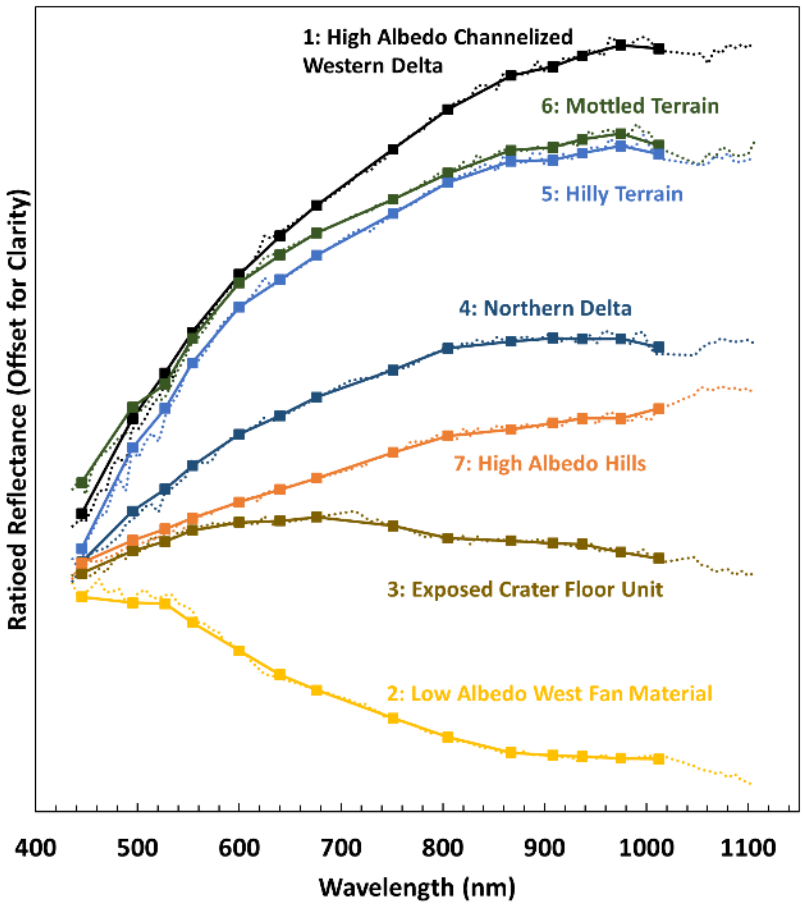

Figure 31: CRISM VNIR spectra for selected geographic areas in and around the proposed Jezero Crater landing zone. Dashed lines are CRISM VNIR spectra from Jezero Crater and solid lines are MCZ VNIR spectra with squares representing spectral filter positions. Absolute reflectance values are not included; reflectance is ratioed and offset for clarity and no longer pertains to real values.

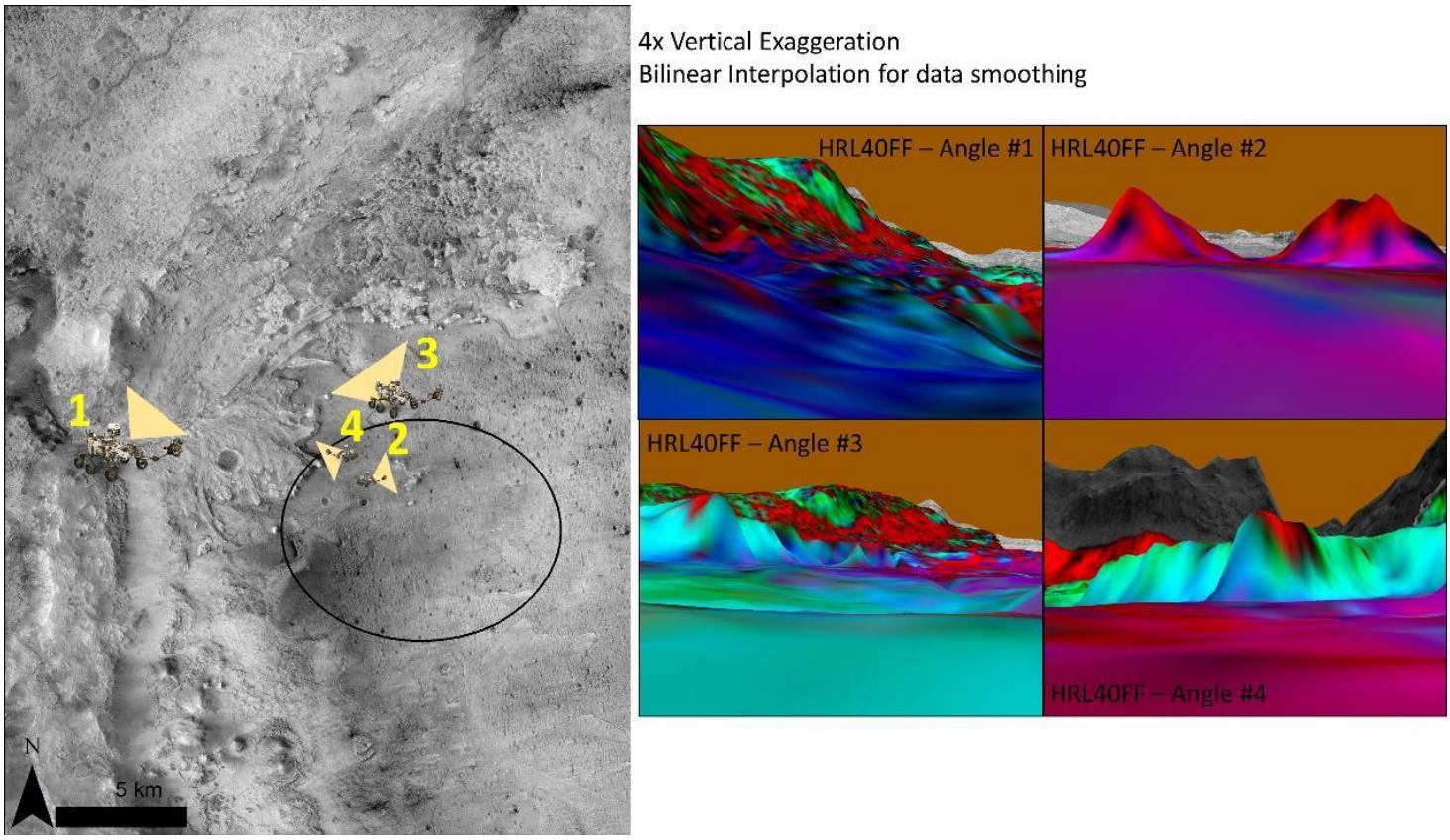

Figure 32: RGB composites for Mastcam-Z parameters have been applied to 3D simulations of Jezero developed using HiRISE imagery and high-resolution digital terrain models. (Left) HIRISE image mosaic (composed of HiRISE images ESP_022680_1985, ESP023102_1985, ESP_037752_1990, ESP045994_1985, PSP_001820_1985, PSP_002743_1985) of Jezero Crater Hills showing simulated rover locations. Numbers refer to the view angles showing in the panels on the right. (Right) 3D perspective images simulating suggested spectral parameters BD_{554} (red), R_{600}/R_{805} (green), and R_{805}/R_{908} (blue) applied to Mastcam-Z imagery.

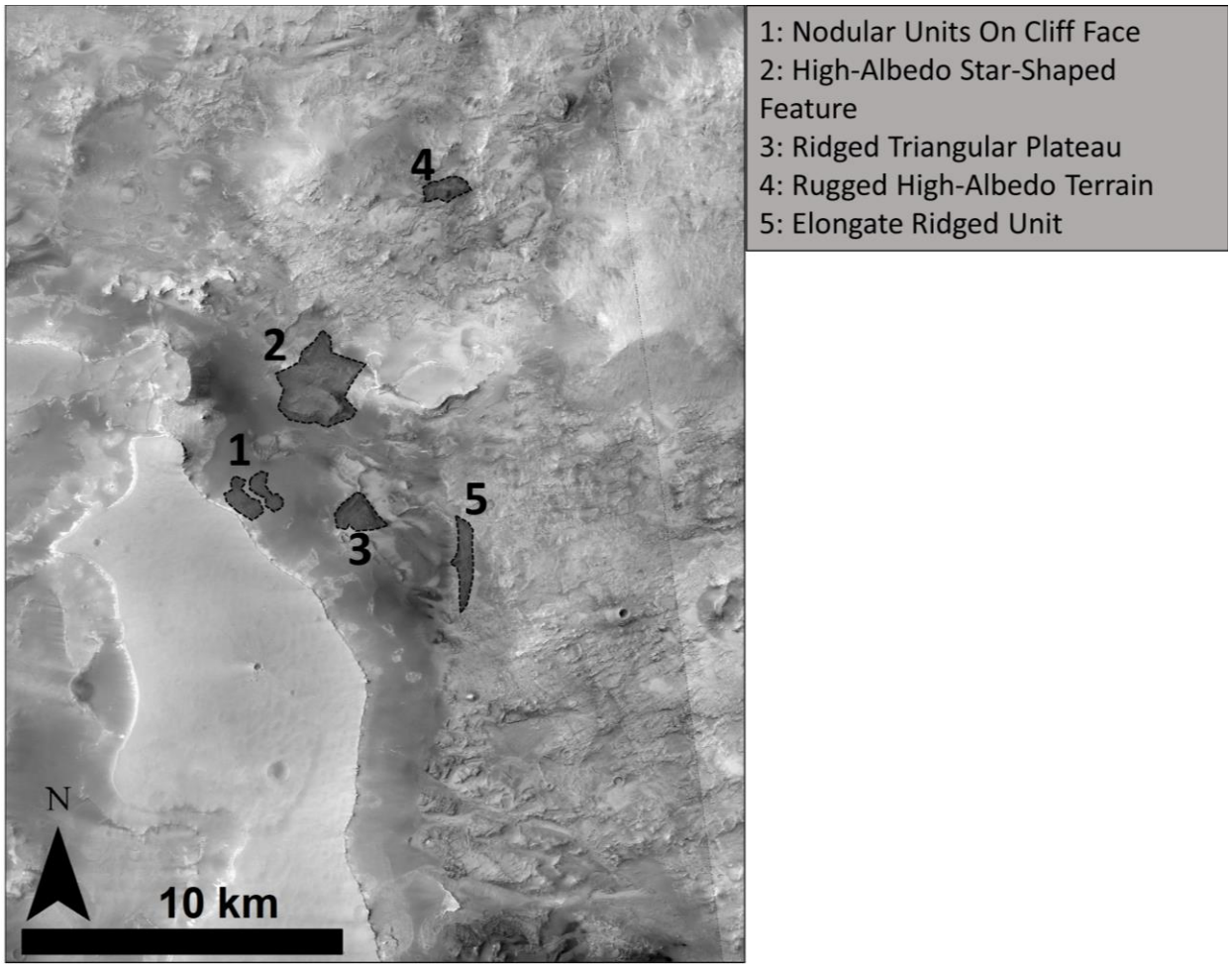

Figure 33: CTX images B18_016720_1978 and B_19_016931_1975 of the NE Syrtis region showing geologic units that were chosen for spectral extraction.

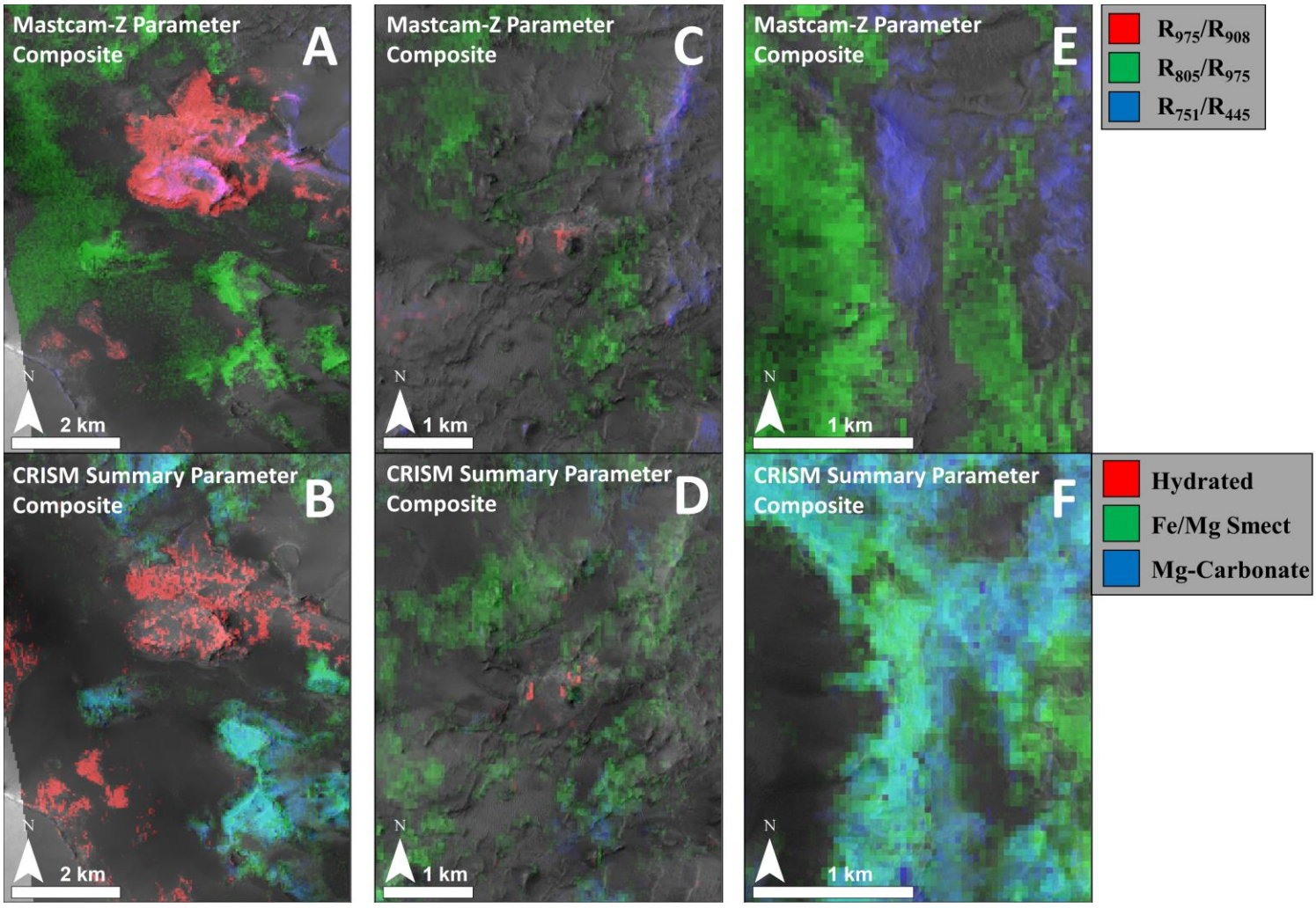

Figure 34: (A) Mastcam-Z parameter composite of NE Syrtis region of interest #1. (B) CRISM SWIR summary parameter composite of NE Syrtis region of interest #1. (C) Mastcam-Z parameter composite of NE Syrtis region of interest #2. (D) CRISM SWIR summary parameter composite of NE Syrtis region of interest #2. (E) Mastcam-Z parameter composite of NE Syrtis region of interest #3. (F) CRISM SWIR summary parameter composite of NE Syrtis region of interest #3. All parameter maps overlain on CTX image B18_016720_1978.

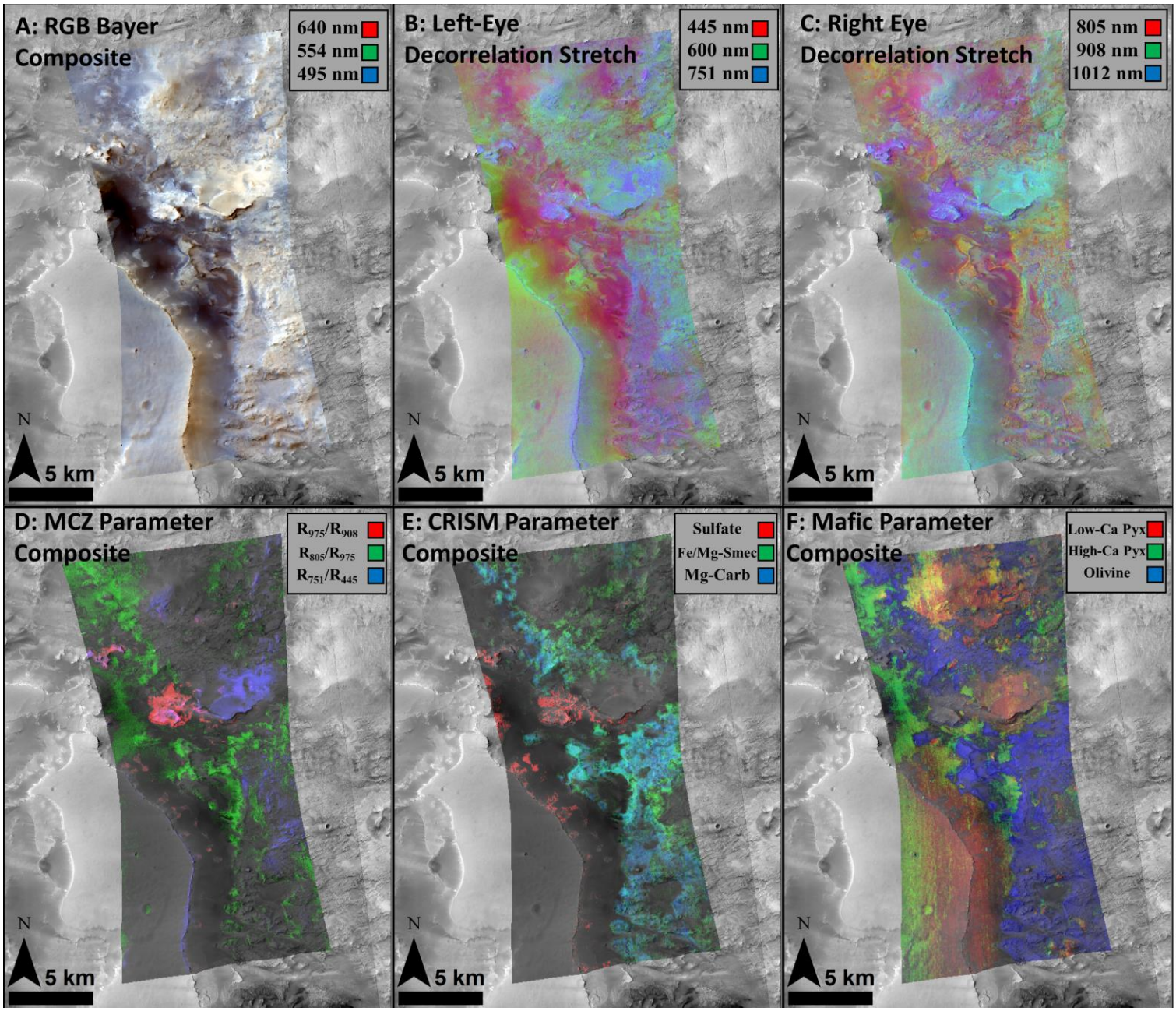

Figure 35: (A) Mastcam-Z RGB Bayer filter composite to simulate Mastcam-Z real-color imagery. (B) Left eye decorrelation stretch. (C) Right eye decorrelation stretch. (D) Mastcam-Z parameter composite. (E) CRISM SWIR summary parameter map for alteration mineralogy. (F) CRISM SWIR summary parameter map for mafic mineralogy. All parameter maps overlain on CTX images B18_016720_1978 and B_19_016931_1975.

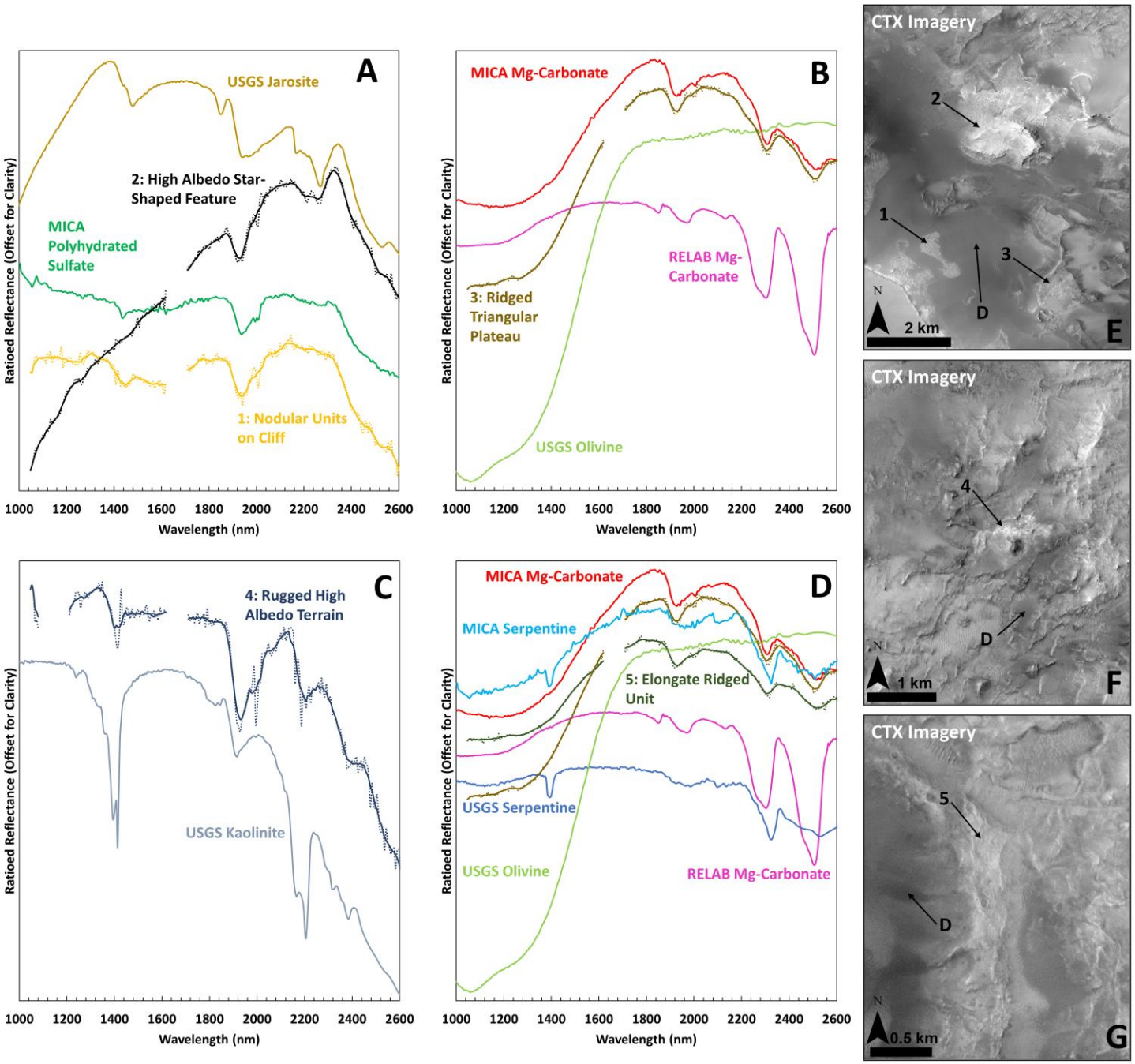

Figure 36: CRISM SWIR spectra for selected geographic areas south of the proposed NE Syrtis landing zone and laboratory spectra from known spectral databases for comparison. Numbered spectra are extracted from CRISM imagery, non-numbered spectra are laboratory spectra. (A) Spectra from the star-shaped feature and nodular units in the cliff face. (B) Spectra from the ridged triangular plateau (C) Spectra from the high-albedo rugged terrain. (D) Spectra from the elongate ridged unit. Dashed lines are spectra prior to 7-pixel boxcar averaged, solid lines are boxcar averaged spectra. Absolute reflectance values are not included; reflectance is ratioed and offset for clarity and no longer pertains to real values. E-G: CTX image B18_016720_1978 of NE Syrtis regions of interest illustrating regions spectra were extracted. Numbered labels are numerator spectra; D is denominator spectrum. Comparison spectra are from the USGS, RELAB, and MICA databases (Pieters and Hiroi, 2004; Viviano-Beck et al., 2014; Kokaly et al., 2017) and their respective sample IDs are olivine_gds70.16284 (USGS olivine), kaolinite_cm3.11788 (USGS kaolinite), serpentine_hs318.20395 (USGS serpentine), jarosite_gds100.11210 (USGS Jarosite), CRB114 (HOSERLab ID for RELAB magnesite). MICA samples do not have sample IDs.

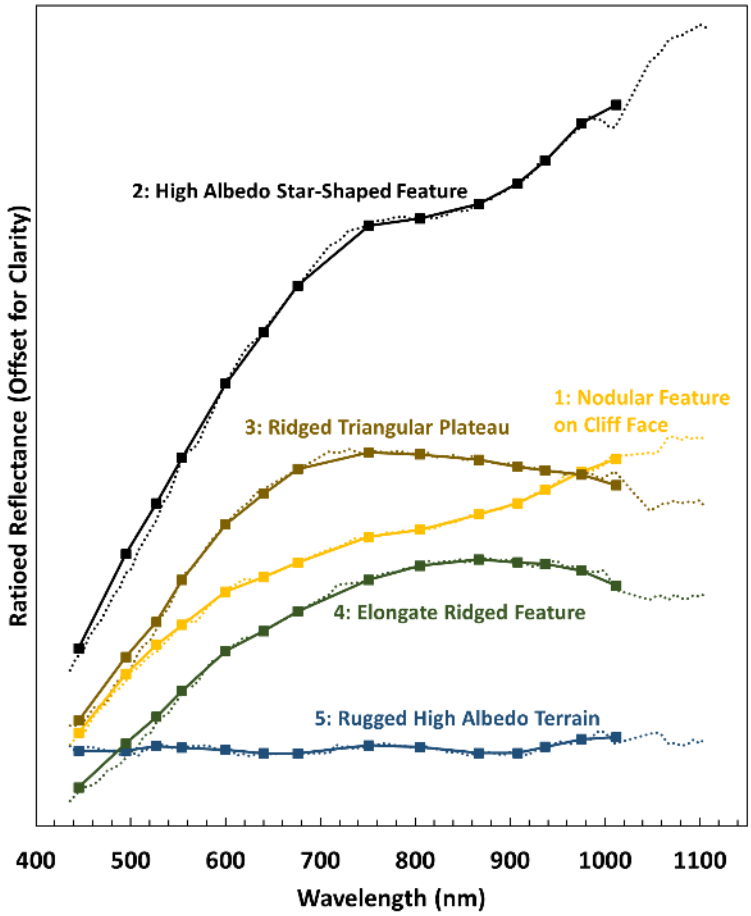

Figure 37: CRISM VNIR spectra for selected geographic areas south of the proposed NE Syrtis landing zone. Dashed lines are CRISM VNIR spectra from NE Syrtis and solid lines are MCZ VNIR spectra with squares representing spectral filter positions. Absolute reflectance values are not included; reflectance is ratioed and offset for clarity and no longer pertains to real values.

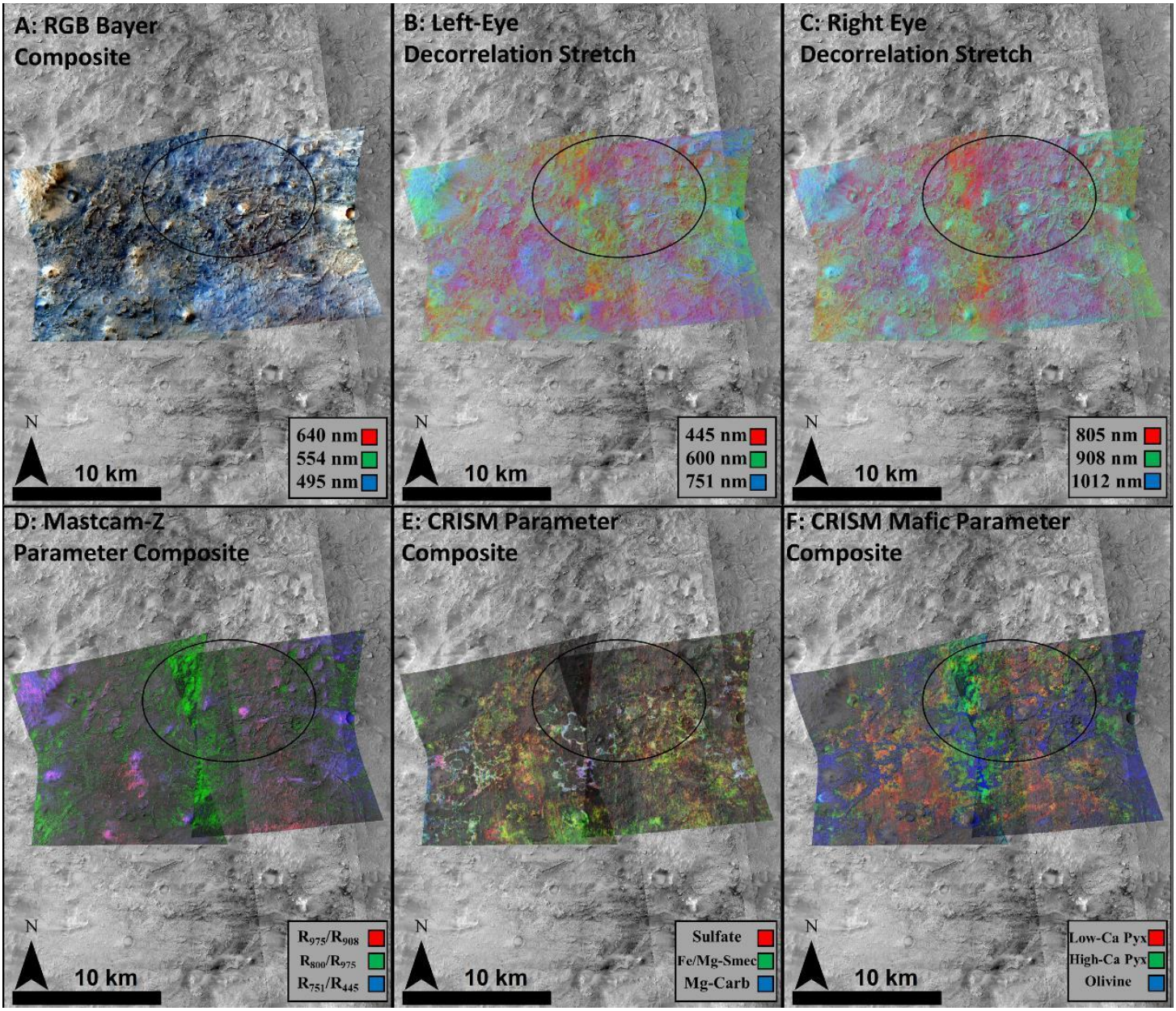

Figure 38: (A) Mastcam-Z RGB Bayer filter composite to simulate Mastcam-Z real-color imagery. (B) Left eye decorrelation stretch. (C) Right eye decorrelation stretch. (D) Mastcam-Z parameter composite. (E) CRISM SWIR summary parameter map for alteration mineralogy. (F) CRISM SWIR summary parameter map for mafic mineralogy. All parameter maps overlain on CTX images B18_016720_1978, B_19_016931_1975, F05_037818_1977, and P06_003376_1987.

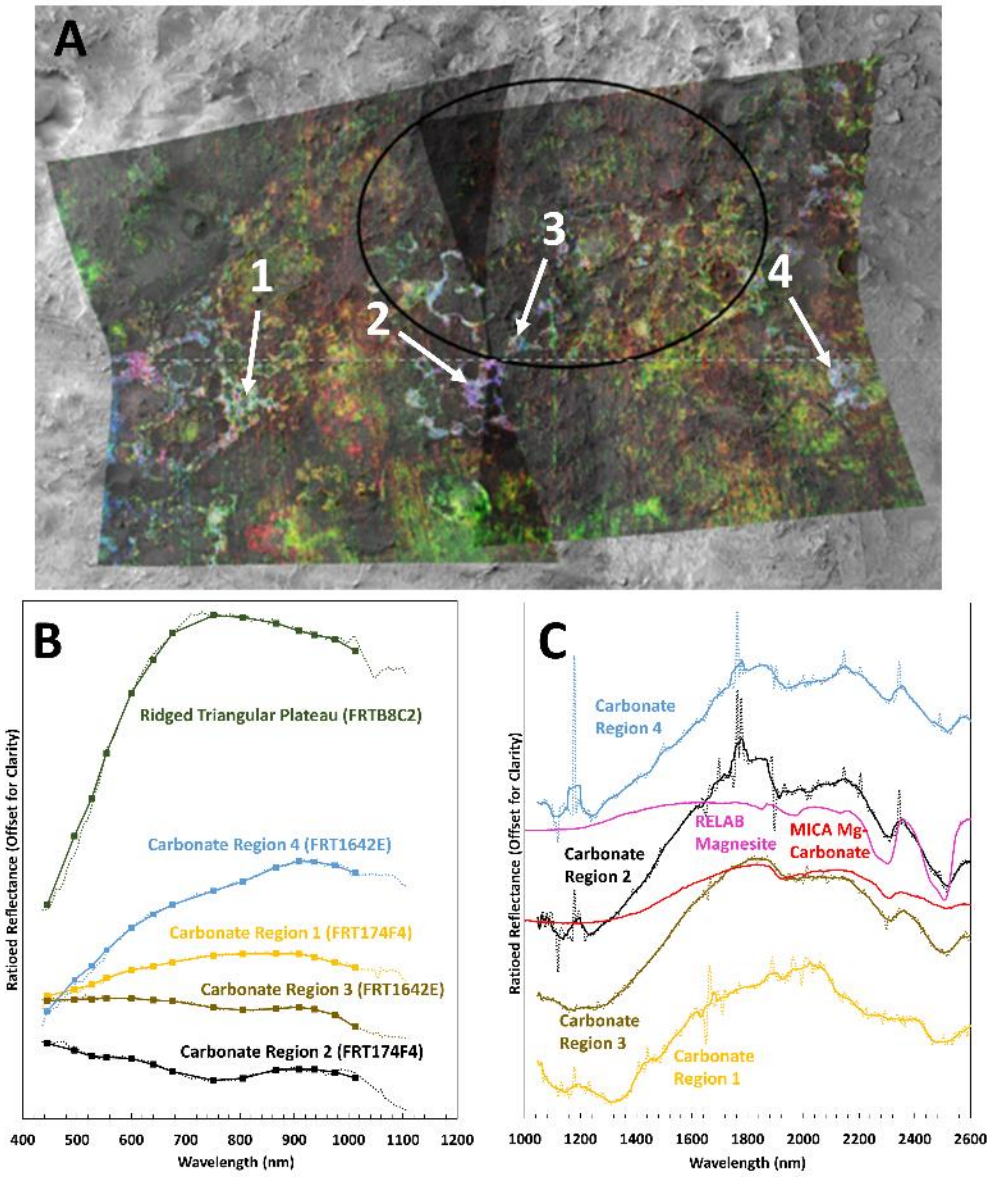

Figure 39: (A) CRISM SWIR summary parameter map for alteration mineralogy overlain on CTX images B18_016720_1978, B_19_016931_1975, F05_037818_1977, and P06_003376_1987. Numbers are regions where spectra were extracted from potential Mg-carbonate units. (B) CRISM VNIR/MCZ spectra for compared to the ridged triangular plateau in FRTB8C2. Numbers in plot labels correspond to numbers in panel A. (C) CRISM SWIR spectra for numbered carbonate regions in the NE Syrtis landing ellipse. Numbers in plot labels correspond to numbers in Panel A. Comparison spectra are from the RELAB and MICA databases (Pieters and Hiroi, 2004; Viviano-Beck et al., 2014) and the RELAB magnesite's HOSERLab sample ID is CRB114. MICA samples do not have sample IDs.

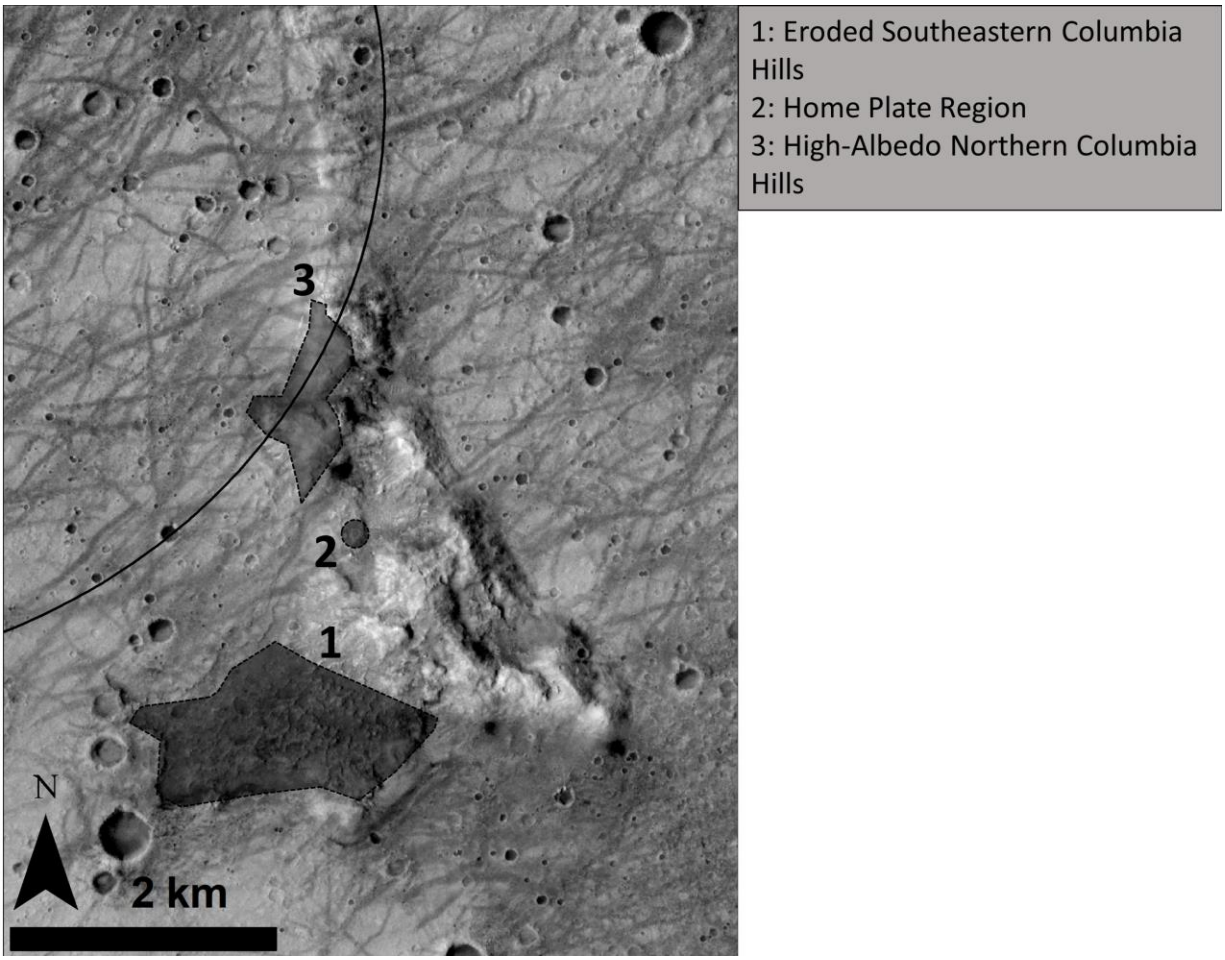

Figure 40: CTX image D06_029415_1653 of the Columbia Hills region showing geologic units that were chosen for spectral extraction. These units will be discussed in this section's results.

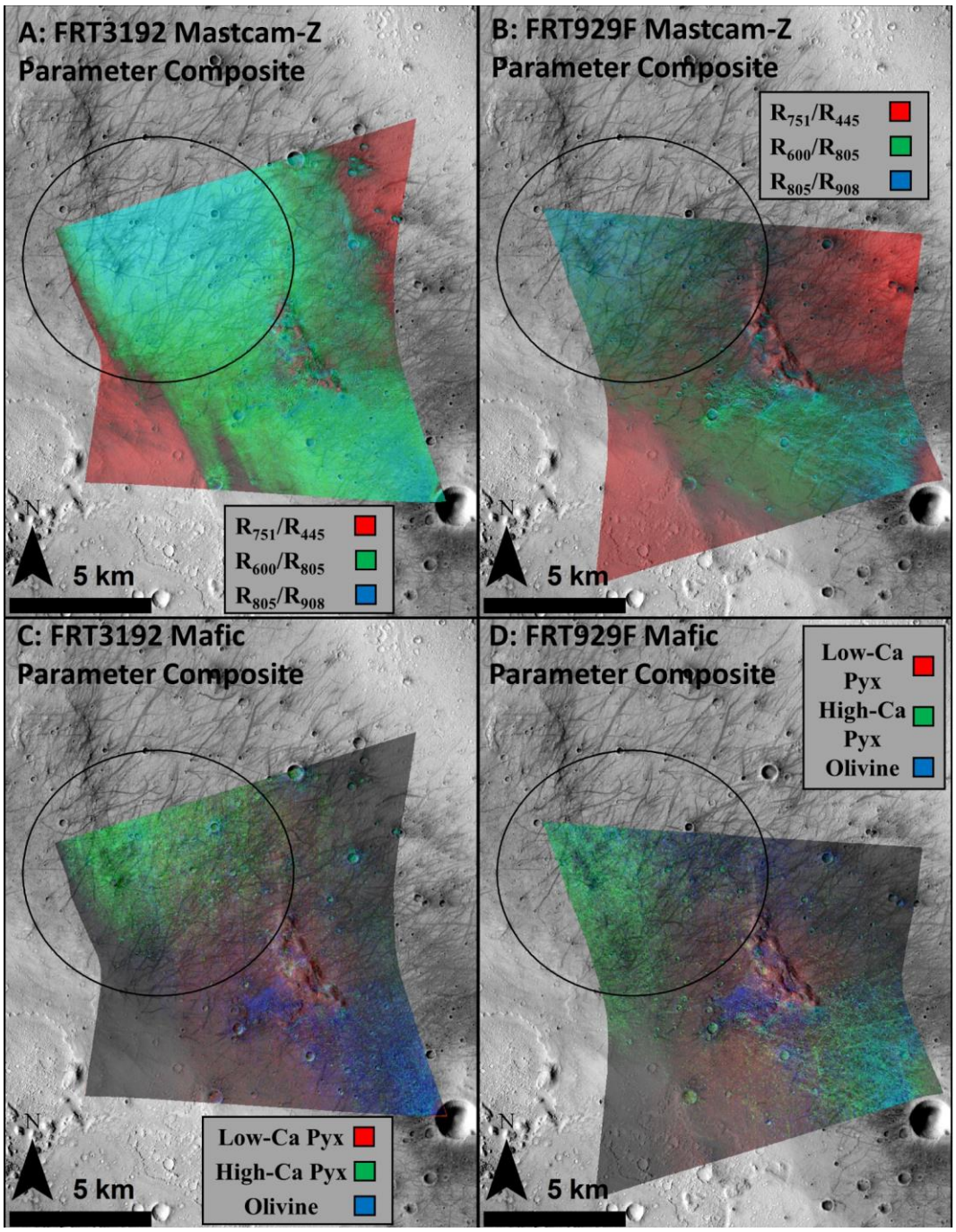

Figure 41: (A) Mastcam-Z parameter composite for FRT3912. (B) Mastcam-Z parameter composite for FRT929F. (C) CRISM SWIR summary parameter composite for mafic minerals in FRT3192. (D) CRISM SWIR Summary parameter composite for mafic minerals in FRT929F. Black ovals are the proposed Columbia Hills landing ellipses. All parameter maps overlain on CTX image D06_029415_1653

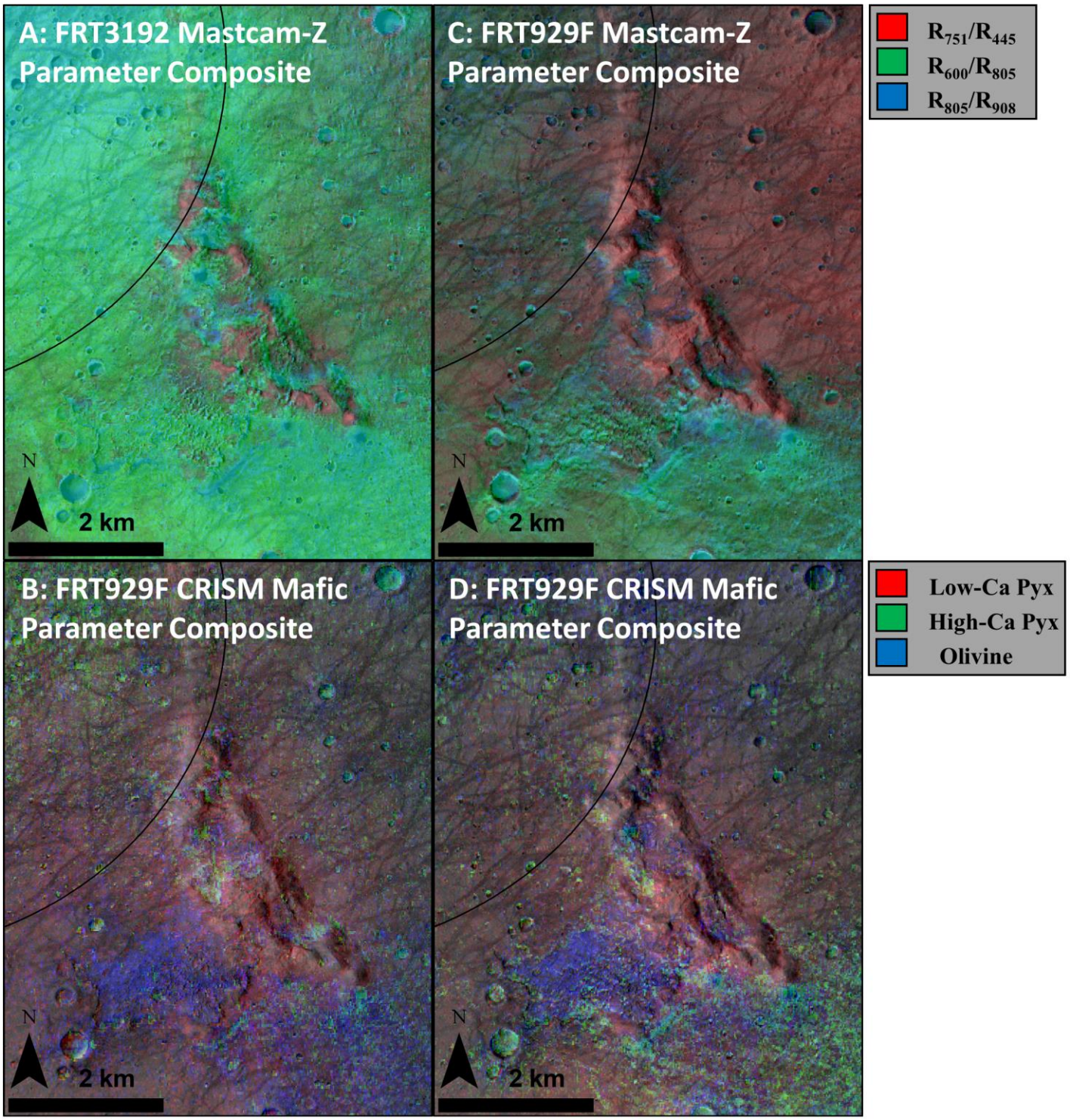

Figure 42: (A) Mastcam-Z parameter composite for FRT3912. (B) Mastcam-Z parameter composite for FRT929F. (C) CRISM SWIR summary parameter composite for mafic minerals in FRT3192. (D) CRISM SWIR summary parameter composite for mafic minerals in FRT929F. Black partial-ovals are the proposed Columbia Hills landing ellipse. All parameter maps overlain on CTX image D06_029415_1653.

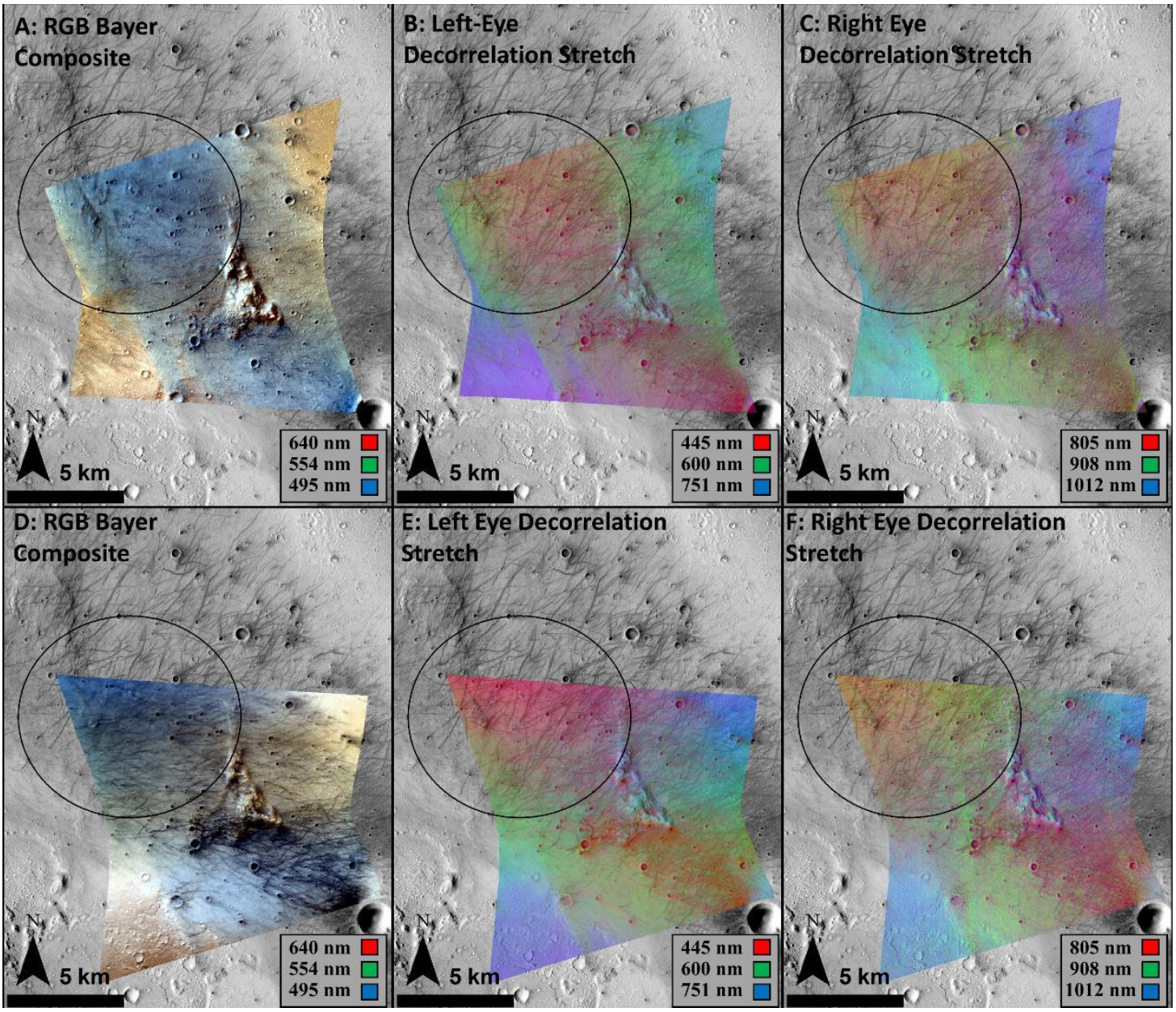

Figure 43: Imagery for FRT3192 (A-C) and FRT929F (D-F). (A) Mastcam-Z RGB Bayer filter composite to simulate Mastcam-Z real-color imagery in FRT3192. (B) Left eye decorrelation stretch for FRT3192. (C) Right eye decorrelation stretch for FRT3192. (D) Mastcam-Z RGB Bayer filter composite to simulate Mastcam-Z real-color imagery in FRT929F. (E) Left eye decorrelation stretch for FRT929F. (F) Right eye decorrelation stretch for FRT929F. All parameter maps overlain on CTX image D06_029415_1653. Black ovals are the proposed Mars-2020 landing ellipse.

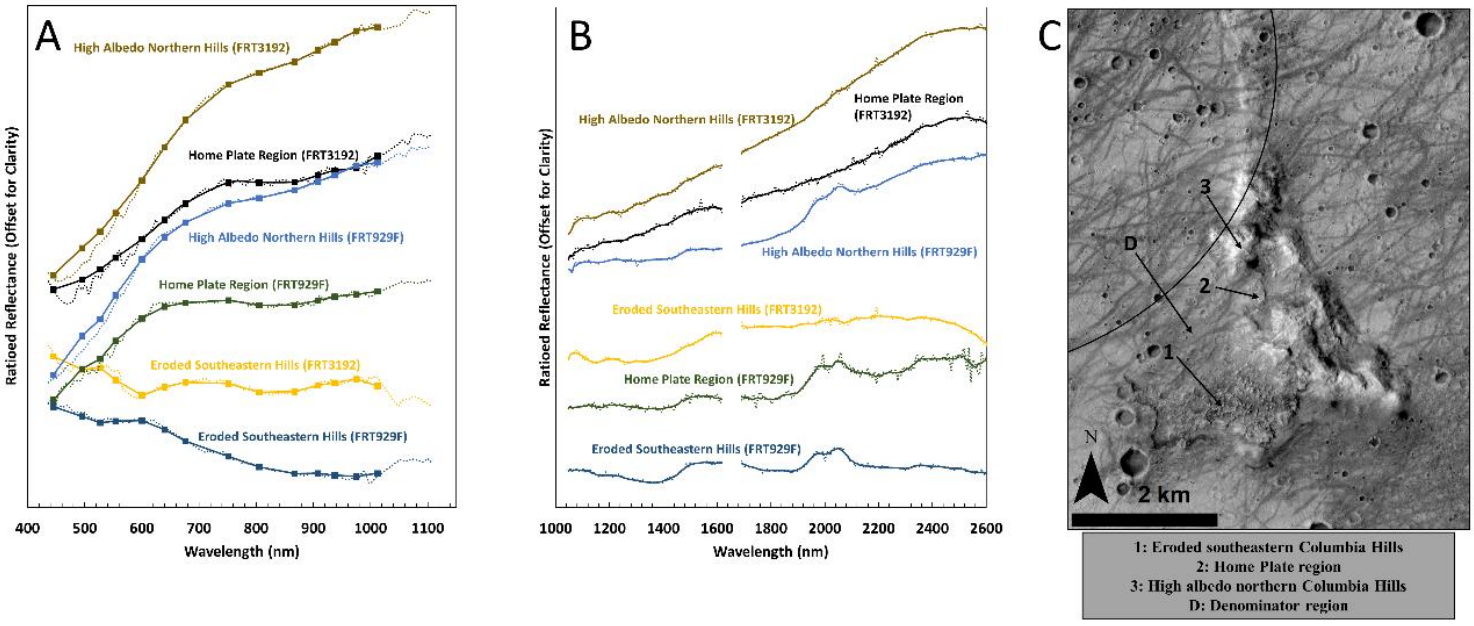

Figure 44: (A) CRISM SWIR spectra for regions of interest in FRT3192 and FRT929F. Dashed lines are spectra prior to 7-pixel boxcar averaged, solid lines are boxcar averaged spectra. (B) CRISM VNIR and MCZ VNIR spectra for regions of interest in FRT3192 and FRT929F. Dashed lines are CRISM VNIR spectra and solid lines are MCZ VNIR spectra with squares representing spectral filter positions. Reflectance values are not included; reflectance is ratioed and offset for clarity and no longer pertains to real values (C) CTX image D06_029415_1653 illustrating regions of spectra extraction. Numbers are numerator spectra; D is denominator spectrum. Black partial-oval is the proposed Mars-2020 landing ellipse.

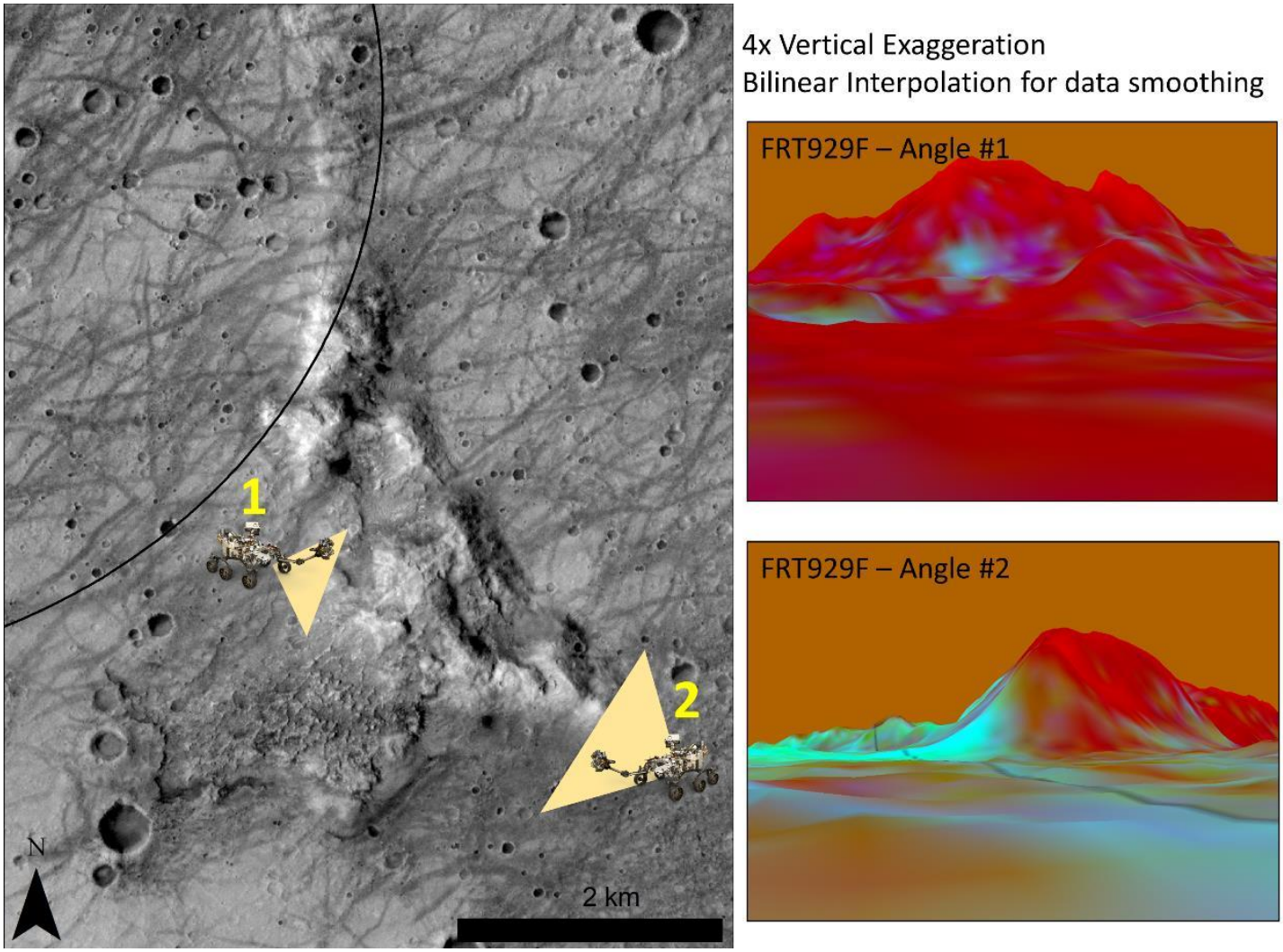

Figure 45: (Left) HIRISE image mosaic (composed of HiRISE images ESP_011943_1650, ESP_034874_1655, ESP_035230_1665, ESP_035586_1655, ESP_035942_1655, ESP_036087_1655, ESP_036641_1655, PSP_001513_1655, PSP_006524_1650, and PSP_008963_1650) of the Columbia Hills showing simulated rover locations and viewing angles. (Right) 3D perspective images simulating MCZ spectral parameters for FRT929F showing observed spectral endmembers; R_{751}/R_{445} (red), R_{600}/R_{805} (green), and R_{805}/R_{908} (blue) applied to Mastcam-Z imagery.

TABLES

(Table number and caption BELOW tables)

Mineral Name	Chemical Formula	H2O/SO4 Ratio	Detections/Inferred Stability on Mars
Gypsum	$CaSO_4 \cdot 2(H_2O)$	2	Bridges and Grady, 2000 Horgan et al., 2009 Squyres et al., 2012 Nachon et al., 2014 Vaniman et al., 2017
Bassanite	$2(CaSO_4) \cdot H_2O$	0.5	Wray et al., 2010 Nachon et al., 2014 Vaniman et al., 2017
Anhydrite (Drierite)	$CaSO_4$	0	Bridges and Grady, 2000 Nachon et al., 2014 Vaniman et al., 2017
Epsomite	$MgSO_4 \cdot 7(H_2O)$	7	Vaniman and Chapera, 2006 Tosca and McLennan, 2006 Tosca et al., 2008
Hexahydrite	$MgSO_4 \cdot 6(H_2O)$	6	Vaniman et al., 2004 Feldman et al., 2004 Vaniman and Chapera, 2006
Kieserite	$MgSO_4 \cdot H_2O$	1	Vaniman and Chapera, 2006 Tosca and McLennan, 2006

Table 1: Minerals used for this study, including chemical formula and H_2O/SO_4 ratio, and references related to either their detection or theoretical stability on the martian surface.

Gypsum Grain Size Series								
975 nm Center Band Depth	937-1013 Band Depth	937-975 Band Depth	975 nm Center % Reduction From Selenite	1013 nm % Reduction From Selenite	975 nm % Reduction From Selenite	Lab Res. Band Depth	Lab Res. Band Pos.	Grain Size (µm)
0.048	0.0766	0.0435	-	-	-	0.0966	1001	Whole Rock
0.0116	0.0149	0.019	75.84	80.61	56.26	0.0228	1001	2000-4000
0.0166	0.0166	0.0264	65.3	78.31	39.33	0.0257	1001	1000-2000
0.0139	0.0293	0.0313	71.01	61.7	28.13	0.0303	1001	500-1000
0.0103	0.0161	0.0184	78.55	78.98	57.78	0.0197	1001	250-500
0.0092	0.016	0.0172	80.88	79.09	60.43	0.0171	1001	125-250
0.0082	0.0139	0.0152	82.89	81.8	65.03	0.0155	1001	63-125
0.0081	0.0091	0.0127	83.01	88.11	70.73	0.0158	1001	<63
Epsomite Grain Size Series								
975 nm Center Band Depth	937-1013 Band Depth	937-975 Band Depth	975 nm Center % Reduction From 2000-4000 µm	1013nm % Reduction From 2000-4000 µm	975 nm % Reduction From 2000-4000 µm	Lab Res. Band Depth	Lab Res. Band Pos.	Grain Size (µm)
0.0555	0.1108	0.106	-	-	-	0.0802	1001	2000-4000
0.0529	0.1123	0.1092	75.84	-1.34	56.26	0.0826	1001	1000-2000
0.0537	0.116	0.1093	65.3	-4.68	39.33	0.0793	1001	500-1000
0.0388	0.083	0.0793	71.01	25.1	28.13	0.057	998	250-500
0.0281	0.0557	0.0555	78.55	49.72	57.78	0.0412	1001	125-250
0.0182	0.0392	0.0377	80.88	64.63	60.43	0.0264	999	63-125
0.0192	0.0391	0.0386	82.89	64.68	65.03	0.0262	1001	<63

Table 2: 975 NM center band depth, 937-1013 band depth, 937-975 band depth, percent reduction of band depths from the selenite sample spectrum (for gypsum) and 2000-4000 µm sample spectrum (for epsomite), laboratory resolution band depth (960 nm and 1050 nm as shoulder positions), and lab resolution band position of gypsum and epsomite grain size series.

Gypsum-Anhydrite Mixture Series								
975 nm Center	937-1013	937-975 Band	975 nm Center %	1013 nm %	975 nm %	Lab Res. Band	Lab Res. Band	Percent Gypsum

Band Depth	Band Depth	Depth	Reduction From 100% Gypsum	Reduction From 100% Gypsum	Reduction From 100% Gypsum	Depth	Pos.	
0.0018	-0.0129	-0.0047	86.80	143.84	114.94	0.0016	964	0%
0.0035	-0.0064	0.0003	74.87	121.71	99.11	0.0031	970	10%
0.0032	-0.0108	-0.0022	77	136.71	107.17	0.003	970	20%
0.005	-0.0002	0.0049	63.91	100.74	84.3	0.0044	974	30%
0.0046	-0.0113	-0.0012	67.22	138.57	103.68	0.0042	970	40%
0.0057	-0.002	0.0047	59.08	106.86	85.05	0.0052	974	50%
0.0073	0.0003	0.0074	47.81	99.11	76.37	0.0113	990	60%
0.0067	0.0002	0.0067	52.14	99.48	78.47	0.0091	990	70%
0.0083	0.0037	0.0101	40.54	87.28	67.56	0.0135	993	80%
0.0088	0.0043	0.011	36.77	85.32	64.96	0.0176	1001	90%
0.0139	0.0293	0.0313	-	-	-	0.0303	1001	100%
Gypsum-Bassanite Mixture Series								
975 nm Center Band Depth	937-1013 band depth	937-975 band depth	975 nm Center % Reduction From 100% Gypsum	1013 nm % Reduction From 100% Gypsum	975 nm % Reduction From 100% Gypsum	Lab Res. Band Depth	Lab Res. Band Pos.	Percent Gypsum
0.0011	-0.0146	-0.0064	92.09	150.37	120.41	0.0012	964	0%
0.0012	-0.0151	-0.0064	91.12	151.53	120.53	0.0015	967	10%
0.0012	-0.0156	-0.0067	91.49	153.02	121.4	0.0006	963	20%
0.0013	-0.0138	-0.0056	90.35	146.95	118.01	0.0015	967	30%
0.0015	-0.017	-0.0071	89.05	157.92	122.63	0.0017	967	40%
0.0018	-0.0127	-0.0046	86.75	143.17	114.6	0.0015	967	50%
0.0031	-0.0092	-0.0016	77.88	131.47	105.08	0.0028	970	60%
0.0026	-0.0116	-0.0032	81.3	139.4	110.37	0.0025	970	70%
0.0047	-0.0021	0.0036	66.17	107.12	88.33	0.0085	990	80%
0.0053	-0.0016	0.0045	61.7	105.43	85.53	0.0106	990	90%
0.0139	0.0293	0.0313	-	-	-	0.0303	1001	100%
Bassanite-Anhydrite Mixture Series								
975 nm Center Band Depth	937-1013 Band Depth	937-975 Band Depth	975 nm Center Center % Reduction From 100% Bassanite	1013 nm % Reduction From 100% Bassanite	975 nm % Reduction From 100% Bassanite	Lab Res. Band Depth	Lab Res. Band Pos.	Percent Bassanite

0.0018	-0.0127	-0.0047	-66.84	12.79	26.79	0.0016	964	0%
0.0035	-0.0105	-0.0019	-214.84	27.84	70.22	0.0033	969	10%
0.0018	-0.0182	-0.0076	-64.32	-24.83	-18.46	0.0009	963	20%
0.0023	-0.0115	-0.0036	-107.94	21.2	43.86	0.0018	966	30%
0.0026	-0.0111	-0.0031	-135.36	24.04	51.97	0.002	966	40%
0.0015	-0.0111	-0.0042	-32.71	23.72	33.79	0.0013	966	50%
0.0016	-0.0151	-0.0062	-42.38	-3.98	2.63	0.0016	966	60%
0.0016	-0.0111	-0.004	-48.92	24.08	37.03	0.0014	966	70%
0.0019	-0.0102	-0.0034	-69.16	29.7	47.17	0.0015	966	80%
0.0011	-0.0131	-0.0056	-2.48	9.96	12.27	0.0012	966	90%
0.0011	-0.0146	-0.0064	-	-	-	0.0012	964	100%

Table 3: 975 NM center band depth, 937-1013 band depth, 937-975 band depth, percent reduction of band depths from 100% of the more hydrated phase, laboratory resolution band depth (960 nm and 1050 nm as shoulder positions), and lab resolution band position of Ca-sulfates mixtures

Epsomite-Kieserite Mixture Series								
975 nm Center Band	937-1013 Band	937-975 Band Depth	975 nm Center % Reductio	1013 nm % Reductio	975 nm % Reductio	Lab Res. Band Depth	Lab Res Band Pos.	Percent Epsomite

Depth	Depth		n From 100% Epsomite	n From 100% Epsomite	n From 100% Epsomite			
0.0067	0.0181	0.0158	87.47	84.41	85.52	0.0062	1024	0%
0.0106	0.0208	0.0211	80.17	82.09	80.73	0.012	998	10%
0.0119	0.0222	0.0231	77.77	80.84	78.9	0.0138	1001	20%
0.0175	0.0337	0.0343	67.33	70.94	68.6	0.0225	1001	30%
0.0174	0.0307	0.0327	67.53	73.53	70.07	0.022	1001	40%
0.0212	0.0391	0.0406	60.48	66.27	62.83	0.0283	1001	50%
0.0203	0.0382	0.0393	62.18	67.09	64.08	0.0271	1001	60%
0.0236	0.0398	0.0433	56.08	65.64	60.39	0.0324	1001	70%
0.0328	0.0615	0.0629	39	46.93	42.44	0.0452	1001	80%
0.0369	0.0717	0.0719	31.25	38.18	34.22	0.0508	1001	90%
0.0537	0.116	0.1093	-	-	-	0.0793	1001	100%
Epsomite-Hexahydrite Mixture Series								
975 nm Center Band Depth	937-1013 band depth	937-975 band depth	975 nm Center % Reduction From 100% Epsomite	1013 nm % Reduction From 100% Epsomite	975 nm % Reduction From 100% Epsomite	Lab Res. Band Depth	Lab Res. Band Pos.	Percent Epsomite
0.0443	0.0454	0.0663	17.49	60.86	39.35	0.0384	985	0%
0.0455	0.0531	0.0712	15.26	54.25	34.89	0.0397	986	10%
0.0406	0.0474	0.0636	24.43	59.15	41.8	0.0387	990	20%
0.0448	0.0639	0.0757	16.55	44.93	30.72	0.047	993	30%
0.0446	0.0641	0.0756	16.97	44.72	30.81	0.0474	993	40%
0.0433	0.0636	0.0741	19.33	45.17	32.17	0.049	993	50%
0.0432	0.0675	0.0759	19.61	41.77	30.55	0.0513	993	60%
0.0414	0.0704	0.0756	22.85	39.32	30.82	0.0536	1001	70%
0.042	0.0777	0.0797	21.84	32.98	27.09	0.0571	1001	80%
0.0429	0.0812	0.0823	20.19	29.96	24.75	0.0612	994	90%
0.0537	0.116	0.1093	-	-	-	0.0793	1001	100%
Hexahydrite-Kieserite Mixture Series								
975 nm Center Band Depth	937-1013 band depth	937-975 band depth	975 nm Center % Reduction From 100% Hexahydrite	1013 nm % Reduction From 100% Hexahydrite	975 nm % Reduction From 100% Hexahydrite	Lab Res. Band Depth	Lab Res. Band Pos.	Percent Hexahydrite

0.0067	0.0181	0.0158	84.82	60.16	76.12	0.0062	1024	0%
0.0088	0.0126	0.0151	80.22	72.18	77.21	0.0083	991	10%
0.0081	0.0129	0.0146	81.73	71.59	78.01	0.0075	992	20%
0.0121	0.0177	0.021	72.65	61.07	68.37	0.0107	991	30%
0.0151	0.0182	0.0242	65.9	60.01	63.54	0.0136	990	40%
0.0221	0.0292	0.0365	50.25	35.59	44.89	0.0193	988	50%
0.0303	0.0284	0.0442	31.74	37.46	33.33	0.0257	982	60%
0.0294	0.0329	0.0455	33.74	27.53	31.31	0.0258	988	70%
0.0309	0.0341	0.0477	30.2	24.87	28.09	0.0268	986	80%
0.0371	0.0444	0.0588	16.19	2.24	11.32	0.031	985	90%
0.0443	0.0454	0.0663	-	-	-	0.0384	985	100%

Table 4: 975 NM center band depth, 937-1013 band depth, 937-975 band depth, percent reduction of band depths from 100% of the more hydrated phase, laboratory resolution band depth (960 nm and 1050 nm as shoulder positions), and lab resolution band position of Mg-sulfate mixtures.

Gypsum-Anhydrite Mixture Series + 5% Dust Contamination								
975 nm Center Band Depth	937-1013 band depth	937-975 band depth	975 nm Center % Reduction from Dust-Free	1013 nm % Reduction from Dust-Free	975 nm % Reduction from Dust-Free	Lab Res. Band Depth	Lab Res. Band Pos.	Percent Gypsum

-0.0002	-0.0044	-0.0025	113.04	65.53	46.77	0.0002	962	0%
0.0001	-0.0159	-0.0079	95.55	-47.5	-252.65	0.0004	961	20%
0.0005	-0.0117	-0.0055	89.41	-3.6	-373.93	0.0003	961	40%
0.0011	-0.0094	-0.0036	84.48	3688.04	149.09	0.0013	968	60%
0.0006	-0.0099	-0.0044	93.21	364.91	143.82	0.0002	961	80%
0.0028	-0.0034	0.0011	79.77	111.43	96.42	0.0073	992	100%
Gypsum-Anhydrite Mixture Series Subset								
0.0018	-0.0129	-0.0047	-	-	-	0.0016	964	0%
0.0032	-0.0108	-0.0022	-	-	-	0.003	970	20%
0.0046	-0.0113	-0.0012	-	-	-	0.0042	970	40%
0.0073	0.0003	0.0074	-	-	-	0.0113	990	60%
0.0047	-0.0021	0.0036	-	-	-	0.0085	990	80%
0.0139	0.0293	0.0313	-	-	-	0.0303	1001	100%
Epsomite-Kieserite Mixture Series + 5% Dust Contamination								
975 nm Center Band Depth	937-1013 band depth	937-975 band depth	975 nm Center % Reduction from Dust-Free	1013 nm % Reduction from Dust-Free	975 nm % Reduction from Dust-Free	Lab resolution band Depth	Lab resolution band Pos.	Percent Epsomite
0.0011	-0.003	-0.0004	83.61	116.8	102.74	0.0016	975	0%
0.0013	-0.0035	-0.0005	89.49	115.78	102.25	0.0018	977	20%
0.0026	-0.0007	0.0023	84.85	102.38	93.05	0.0041	989	40%
0.007	0.0089	0.0115	65.5	76.64	70.72	0.0099	990	60%
0.0114	0.0166	0.0197	65.2	73.06	68.68	0.0163	990	80%
0.0283	0.054	0.0549	24.49	26.37	25.06	0.0473	1001	100%
Epsomite-Kieserite Mixture Series Subset								
0.0067	0.0181	0.0158	-	-	-	0.0062	1024	0%
0.0119	0.0222	0.0231	-	-	-	0.0138	1001	20%
0.0174	0.0307	0.0327	-	-	-	0.022	1001	40%
0.0203	0.0382	0.0393	-	-	-	0.0271	1001	60%
0.0328	0.0615	0.0629	-	-	-	0.0452	1001	80%
0.0537	0.116	0.1093	-	-	-	0.0793	1001	100%

Table 5: 975 NM center band depth, 937-1013 band depth, 937-975 band depth, percent reduction of band depths from corresponding uncontaminated samples, laboratory resolution band depth (960 nm and 1050 nm as shoulder positions), and lab resolution band position of dust contaminated mixtures.

Simulated Spectra				Laboratory Spectra		
% Epsomite	Band Depth	Band Position	**% of Lab Band Depth**	**% Epsomite**	Band Depth	Band position
10	0.0092	1019	76.48	**10**	0.012	998
20	0.0147	1000	106.30	**20**	0.0138	1001
30	0.0192	1000	85.29	**30**	0.0225	1001

40	0.0243	1000	110.53	**40**	0.022	1001
50	0.0302	1000	106.65	**50**	0.0283	1001
60	0.0370	1000	136.37	**60**	0.0271	1001
70	0.0449	1000	138.48	**70**	0.0324	1001
80	0.0540	1001	119.49	**80**	0.0452	1001
90	0.0654	1001	128.73	**90**	0.0508	1001

Table 6: Percent epsomite (relative to kieserite), band depth, and bad position for modeled spectra and laboratory spectra. Percent of laboratory band depth is calculated for modeled band depth to illustrate error in the linear mixing model for this sample set.

Observation ID	Date Acquired	Landing Site	Prominent Units	Solar Longitude (L_s)	Lat/Lon
FRT3192	11/22/2006	Columbia Hills	Columbia Hills and surrounding volcanic plains	139° Northern	14.5478 S, 175.6255

				Summer	E
FRT929F	1/3/2008	Columbia Hills	Columbia Hills and surrounding volcanic plains	12° Southern Fall	14.5478 S, 175.6255 E
HRL40FF	1/29/2007	Jezero Crater	Western and northern delta, crater rim, volcanic floor	175° Northern summer	18.85 N, 77.52 E
HRLB8C2	7/14/2008	NE Syrtis	Large cliff-forming unit south of landing ellipse, ridges, plateaus, and mafic sand units extensively mapped by Ehlmann and Mustard, 2012	99° Northern Summer	18N, 77E
FRT174F4	3/19/2010	NE Syrtis	Abundant mound and ridge forming units within the landing ellipse	66° Northern Spring	18N, 77E
FRT1642E	2/2/2010	NE Syrtis	Abundant mound and ridge forming units within the landing ellipse	43° Northern Spring	18N, 77E

Table 7: Observation ID, date CRISM acquired the observation, location, and prominent geologic units for each CRISM observation used in this study.

CRISM Summary Parameters			
Parameter ID	**Parameter**	**Mineral Sensitivity**	**Formulation**
OLINDEX3	Broad 1000 nm	Olivine	(RB1210 * 0.1) + (RB1250 * 0.1) +

	absorption		(RB1263 * 0.2) + (RB1276 * 0.2) + (RB1330 * 0.4)
LCPINDEX2	Broad 1810 nm absorption	Low-Ca Pyroxene	(RB1690 * 0.2) + (RB1750 * 0.2) + (RB1810 * 0.3) + (RB1870 * 0.3)
HCPINDEX2	Broad 2120 nm absorption	High-Calcium Pyroxene	(RB2120 * 0.1) + (RB2140 * 0.1) + (RB2230 * 0.15) + (RB2250 * 0.3) + (RB2430 * 0.2) + (RB2460 * 0.15)
D2300	2300 nm dropoff	Hydroxylated Fe,Mg Silicates (Fe/Mg smectites)	$1-\left(\frac{\frac{R2290}{RC2290}+\frac{R2320}{RC2320}+\frac{R2330}{RC2330}}{\frac{R2120}{RC2120}+\frac{R2170}{RC2170}+\frac{R2210}{RC2210}}\right)$
SINDEX2	Convexity at 2290 nm due to 2100 nm and 2400 nm absorptions	Hydrated Sulfates	$1-\left(\frac{a*R2120+b*R2400}{R2290}\right)$
MIN2295_2480	Mg-carbonate overtone band depth and metal-OH band	Mg-Carbonates	minimum $\left[\left(1-\left(\frac{R2295}{a*R2165+b*R2364}\right)\right)\right]$, $\left[\left(1-\left(\frac{R2480}{a*R2364+b*R2570}\right)\right)\right]$
BD1900_2	1900 nm H_2O band depth	Hydrated Minerals	$1-\left(\frac{\left(\frac{R1930+R1985}{2}\right)}{a*1875+b*2067}\right)$

Table 8: CRISM summary parameters used in this study including parameter ID, parameter function, and mineral sensitivity (parameters developed by Viviano-Beck et al., 2014). R = reflectance at wavelength ####, RC = reflectance of continuum line at wavelength ####, RB = band depth at #### nm.

Suggested Mastcam-Z Parameters				
Parameter	**Parameter ID**	**Landing Site**	**Histogram Stretch**	**Geologic Units**

751 nm/445 nm	R_{751n}/R_{445nm}	Columbia Hills	4.27 - 5.32	N/NE Columbia Hills
600 nm/751 nm	R_{600nm}/R_{805nm}	Columbia Hills	0.79 - 0.825	SE Columbia Hills + Volcanic Plains
805 nm/908 nm	R_{805nm}/R_{908nm}	Columbia Hills	1.03 - 1.044	Small Craters + Sand Dunes
554 nm Band Depth (445 nm, 676 nm Shoulders)	BD_{554}	Jezero Crater	0.00726 - 0.029	Deltaic Sediments + N of Crater Rim (Mg-Carbonate/Phyllosilicate-bearing)
600 nm/805 nm	R_{600}/R_{805}	Jezero Crater	0.845 - 0.887	Crater Floor Units + Southern Jezero
805 nm/908 nm	R_{805}/R_{908}	Jezero Crater	1.076 - 1.099	Sand Dunes + Delta Front
975 nm/908 nm	R_{975nm}/R_{908nm}	NE Syrtis	0.968 - 0.979	Sulfate-Bearing Units
805 nm/975 nm	R_{805}/R_{975}	NE Syrtis	1.142 - 1.17	Mg-Carbonate/Olivine-Bearing Units
751 nm/445 nm	R_{751}/R_{445}	NE Syrtis	3.14 - 3.49	Serpentine-Bearing Ridge

Table 9: Simulated Mastcam-Z Spectral parameters for each landing site, histogram stretches used for these parameters in Figures 28-29, 32-34, 39-40, and 43, and the geologic units they highlight. 'BD' indicates a band depth. 'R_{xxx}/R_{xxx}' indicates a ratio of the reflectance at two wavelengths.

Pancam	Proposed	Pancam Formula	Proposed	Purpose

Parameter	Mastcam-Z Parameter		Mastcam-Z Formula	
482 to 673 nm slope	495 to 676 nm slope	1000*((R673-R482)/191)	1000*(R676-R495)/191)	Gauge of Fe oxidation
535 nm band depth	527 nm band depth	1-(R535/((0.57*R432)+(0.43*R673)))	1-(R527/((0.57*R445)+(0.43*R676)))	Gauge of development of ferric oxides
601 nm band depth	600 nm band depth	1-(R601/((0.57*R535)+(0.43*R673)))	1-(R600/((0.57*R527)+(0.43*R676)))	Assess convexity near 600 nm
803 nm / 904 nm	805 nm / 908 nm	R803/R904	R805/R908	Indicator of strength of NIR absorption band
803 nm / 1009 nm	805 nm / 1013 nm	R803/R1009	R805/R1013	Help distinguish between olivine and pyroxene dominated lithologies
904 nm band depth	908 nm band depth	1-(904/((0.57*R803)+(0.43*R1009)))	1-(R908/((0.57*R805)+(0.43*R1013)))	Assess depth of NIR absorption band
754 to 1009 nm slope	751 to 1013 nm slope	1000*((R1009-R754)/255)	1000*((R1013-R751)/255)	Gauge of hematite development; indicator of pyroxene, olivine
934 to 1009 nm slope	937 to 1013 nm slope	1000*((R1009-R934/75)	1000*((R1013-R937/75)	Indicator of H_2O overtone band
Fitted reflectance peak position	Fitted reflectance peak position	Maximum of 5^{th} degree polynomial fitted to bands from 535 to 904 nm	Maximum of 5^{th} degree polynomial fitted to bands from 527 to 908 nm	Gauge of Fe oxidation
Fitted NIR band minimum position	Fitted NIR band minimum position	Minimum of 3^{rd} degree polynomial fitted to bands from 864 to 1009 nm	Minimum of 3^{rd} degree polynomial fitted to bands from 867 to 1013 nm	Distinguish between Fe-bearing phases

Table 10: Pancam parameters from Farrand et al., 2016, parameter formulas, and parameter purpose, compared to suggested Mastcam-Z adaptations.